1988

Magneto-Optical Sensing Utilizing the Faraday Effect in Bulk $Cd_{1-x}Mn_xTe$

Jeff C. Adams
University of Rhode Island

MAGNETO-OPTICAL SENSING UTILIZING THE FARADAY EFFECT IN BULK $Cd_{1-x}Mn_xTe$

BY

JEFF C. ADAMS

A THESIS SUBMITTED IN PARTIAL FULFILLMENT OF THE REQUIREMENTS FOR THE DEGREE OF MASTER OF SCIENCE IN ELECTRICAL ENGINEERING

UNIVERSITY OF RHODE ISLAND

1988

MASTER OF SCIENCE THESIS

OF

JEFF C. ADAMS

APPROVED:

Thesis Committee

Major Professor Harish R. D. Sunak

Frank Lyford Morris

Nicolas Jones

Dean of the Graduate School

UNIVERSITY OF RHODE ISLAND

1988

ABSTRACT

A magnetic field sensor utilizing the Faraday effect in bulk $Cd_{1-x}Mn_xTe$ was investigated. The magnetic field sensitivity was found theoretically as a function of various system parameters and compared with experiment.

The magneto-optical Verdet constant of $Cd_{.5}Mn_{.5}Te$ was measured at a wavelength of 633 nm, and found to be 0.15° $cm^{-1}Gauss^{-1}$. The optical absorption was measured to be 0.9 cm^{-1}, and the refractive index 3.1; all values agreed well with published measurements.

A polarization preserving fiber was used to link the $Cd_{.5}Mn_{.5}Te$ sensor in a polarization-rotated reflection scheme in order to cancel environmentally induced linear birefringence fluctuations which contribute to system noise. The linear birefringence fluctuations were modelled as a gaussian distributed random variable and included in the formulation of the sensing system's signal-to-noise ratio. Since the standard deviation of the birefringence fluctuations was not known a priori, its value was chosen to match theory with experiment, and then compared with data from recently published papers examining the statistics of linear birefringence fluctuations in polarization-preserving fibers; published values of the standard deviation of birefringence fluctuations for a given environmental perturbation compared reasonably with values inferred from our experimental data. Experimental results showed a marked improvement in the magnetic sensor's signal-to-noise ratio using this method of polarization-rotated reflection.

ACKNOWLEDGEMENTS

The author would first like to thank his major professor, Dr. Harish Sunak, whose enthusiastic support made it possible to pursue this subject. Helpful discussions also came from Dr. Lengyel, Dr. Cuomo, Dr. Letcher, Dr. Polk, Dr. Vaccaro, and Dr. Swaszek.

Also, a special thanks to Joe Zieman, who made the $Cd_{1-x}Mn_xTe$ crystals at the Oregon Graduate Center with support from Dr. Russell Kremer, and Bill Dippert of Tektronix, whose recognition of the viability of optical sensors led to the support of this research.

Appreciation also goes out to Andy Rosenberger of the Mechanical Engineering Department for diamond cutting new crystal samples, Ganiyu Hanidu for instruction on crystal polishing, and Jim Vincent for his assistance in acquiring needed instrumentation.

Finally, I would like to thank my wife, Laurie, for enduring a long distance relationship during my stay at URI.

CONTENTS

LIST OF TABLES

LIST OF FIGURES

CHAPTER 1 ◊ INTRODUCTION

1.1 Introduction to optical sensors

In its broadest definition, optical sensing is the detection and analysis of light which has been modulated or modified by some perturbation. The perturbation could be virtually anything: temperature, displacement, acceleration, acoustics, electric and magnetic fields, and so on. Characterizing the response of some light parameter to a perturbation thus enables us to measure that perturbation.

Optical sensors can generally be placed into one of three catagories: (1) an optical fiber acting as the transducer, (2) an optical fiber acting simply as a link to an external transducer, and (3) the optical transducer using free space light, without an optical fiber link. Since a number of papers have been written which cover the full gamut of optical sensor technology [1]-[10], we will provide only salient features of optical sensors for the purposes of this introduction.

The advantages of many optical sensors are their inherent compatability with optical fiber telemetry, immunity to electromagnetic interference and other hostile environments, and high sensitivity. Examples of sensitivities for various optically measured quantities include: (1) temperature--200° to -50° C ±0.1° C using a fiber microprobe by Luxtron Corp. [2]; (2) acceleration--6 x 10^{-8} g's detected at 35 Hz at Optech, Inc. [8]; (3) pH--6 - 12 ±0.02 [2]; (4) sound pressure--3 - 170 dB with reference to 1 μP [2]; (5) magnetic fields--10^{-9} Gauss at low frequencies [1]; (5)

flow--10^{-6} - 10^{5} m/s [2].

Futhermore, though many such sensors are still in the research and development stage, the market predictions are impressive. According to Kessler Marketing Intellegence, the consumption of fiber-optic sensors--not including ancillary electronics and packaging--will grow 30 percent annually, moving from about $20 million in 1983 to $278 million in 1993. From 1979 to 1981, the number of fiber-optic sensor patents increased nearly 2.5 times [11].

1.2 Significance of research

In the area of magneto-optical sensing, there are two primary sensing methods. The one that has received the most attention is the interferometric magnetometer, because of its particulary high sensitivity. In this method, a magnetorestrictive coating is put on a length of fiber, or the fiber is wound on a mandrel which has some magnetorestrictive surface. In both cases, an applied **B**-field stresses the magneto-optical material, thus changing the optical path length of the fiber. This change in optical path length is then detected using an interferometer. Since an interferometer can detect phase shifts as small as 10^{-6} radians, this scheme can be quite sensitive. The lowest detected magnetic fields using this method are on the order of 10^{-9} Gauss [1], but frequency response is usually low (e.g. 100 Hz - 10 KHz). Measurement of DC **B**-fields has been demonstrated down to 1 μG [12].

The other method of magneto-optical sensing utilizes the Faraday effect, which rotates the polarization vector in a material under the influence of a magnetic field. Sensitivities using this effect are usually much less than those obtained with interferometric optical magnetometers, but offer potentially higher frequency response, greater immunity to hostile environments, and are far easier to implement.

In fact, much of the market potential for Faraday effect magnetometers lies in the measurement of large fields. Measurement of large currents (e.g. 1 - 1000 amps) in the power industry using the Faraday effect in silica fiber or bulk glasses has received much attention [13]-[19], and is justified by the following points. First, the increase in transmission voltages necessitates the use of conventional (inductive) current transformers with greater isolation capabilities--this has sharply raised production costs [19]. On the other hand, fiber-optic current sensors are naturally good isolators and offer the potential of using identical devices for different voltage levels. Second, the power environments are electromagnetically noisy; optical fibers offer immunity to electromagnetic interference (EMI). Third, optical sensors are essentially free from saturation effects. Finally, optical current sensing can potentially capture high frequency transients with characteristics or "signatures" that may provide useful diagnostic information [20].

Other application areas include the defense and aerospace industry, where lightning testing can require measuring millions of amperes, and where EMI is a common problem.

Current sensing using fibers is becoming well developed but has a few inherent problems. For one thing, the small Faraday response in optical fibers can require the use of many meters of fiber to get a usable effect. Even though the frequency response may be more than adequate to handle power system requirements, the optical transit time of light through the fiber limits its use at frequencies above, say, hundreds of MHz; a strong tradeoff exists between sensitivity and frequency response. Futhermore, there is a problem with the intrinsic and bend induced birefringence of optical fibers which conspires to reduce sensitivity and accuracy. This problem has been substantially mitigated, but only at the cost of increased complexity. Finally, though the fiber sensor is well suited for

measurements of conductor currents, it is not practical for magnetic field measurements requiring high spatial resolution. It should also be pointed out that because magnetic induction is proportional to frequency, conventional magnetic sensors used at high frequencies are especially subject to error voltages due to undesired induction in circuit layouts, ground loops, sensor leads, and so forth.

The answer to these problems lies in the use of a small sample of optical material with a high Faraday effect response. Materials exist that are nearly three orders of magnitude higher in sensitivity to magnetic fields than silica fiber or quartz, thus requiring shorter material lengths to acheive similar sensitivities. Concomitantly high frequency response (provided the material is intrinsically fast) and high spatial resolution become possible. A material with these attributes has recently surfaced, and is used in our experiments as a proposed magnetic field sensor. The material is a "dilute magnetic semiconductor" of composition $Cd_{1-x}Mn_xTe$.

Though the emphasis of this work pertains to magnetic detection, the investigation will provide useful information for any device utilizing polarization rotation, such as optical isolators or certain magneto-optic modulators.

1.3 Organization of thesis

The general mechanisms responsible for the Faraday effect will be reviewed first, followed by a discussion of the properties of $Cd_{1-x}Mn_xTe$. Chapter 3 covers the experimental measurement of the magneto-optical Verdet constant in this material. In chapter 4 we determine the minimum resolvable polarization rotation ($\Delta\theta$) in a Faraday medium using laser light in free space and a PIN photodiode; $\Delta\theta$ will then translate into a minimum measurable **B**-field. In this formulation we consider a minimum specified signal-to-noise ratio, the light's degree of polarization,

the ellipticity of the polarized component, the extinction ratio of the analyzer, the detector noise, and the intensity of the input light. Example calculations of minimum measurable fields will be given along with discussions about practical limitations. Theory will be related to the minimum resolvable B-field that was noted while making the measurement of the Verdet constant. Dynamic range of possible measurements and practical electronics following the detector will be discussed.

Chapter 5 will discuss in detail the use of a polarization preserving fiber that couples light into and out of the crystal sensor, and does so in such a manner as to cancel fiber birefringence fluctuations which contributes noise to the sensing system. This undesirable birefringence fluctuation will be modelled as a gaussian distributed random variable and incorporated into formulations that give the signal-to-noise ratio of the fiber-optically linked magnetic sensor, considering certain quantifiable system non-idealities. Since the statistics of the birefringence fluctuations are not known a priori, the variance of these fluctuations (which turns out to be the statistic of importance) will be estimated by choosing the variance that matches theory to experiment. The so chosen variance will then be compared for reasonableness with values obtained in recently published papers for the same type of polarization preserving fiber. As the primary purpose of the fiber-linked sensor experiment is to observe a reduction in noise on a magnetic signal that is being monitored, we will show spectrum analyzer photos with and without the noise suppression scheme in effect.

In order to provide a magnetic field measurement reference, I built and calibrated a Hall effect magnetometer, which is described in appendix 1. Also, since we had to produce magnetic fields of at least 300 or so Gauss, it was necessary to design a magnetic field generator. This is described in appendix 2. The crystal refractive index and absorption measurement was put in appendixes 4 and 5 so as not

to break-up the main thrust of the presentation. Other appendixes including these are listed in the contents and appropriately referenced in the text.

CHAPTER 2 ◊ THE FARADAY EFFECT

2.1 Introduction

In the words of Jacob Bronowski, "All science is the search for unity in hidden likenesses." [21] In 1846, Michael Faraday expressed this same basic sentiment in Philisophical Transactions, where he describes the research that showed for the first time a direct connection between magnetism and light:

> I have long held an opinion...that the various forms under which the forces of matter are made manifest have one common origin; or, in other words, are so directly related and mutually dependent, that they are convertible, as it were, one into another....
>
> This strong persuasion extended to the powers of light, and led...to many exertions, having for their object the discovery of the direct relation of light and electricity, and their mutual action in bodies subject jointly to their power....[22]

The "hidden likeness" that Faraday found was an interaction between light and matter in the presence of a magnetic field.

By passing polarized input light through a material and adjusting an analyzer at the output to extinguish the light, Faraday noticed that when a magnetic field was applied parallel with the light propagation direction, the light exiting the analyzer was no longer extinguished. He first discovered this in a heavy glass called silicated borate of lead, and found that the amount of rotation of the plane of polarization in the glass was proportional to the applied magnetic field. Faraday predicted that this relationship between light and magnetism would "prove exceedingly fertile," [22] and a generation later, Maxwell proved this so.

The proportionality between the amount of polarization rotation--and thus the applicability of this effect to the measurement of magnetic fields--is seen from the

empirical relation

$$\theta = V\int_0^L \mathbf{B}\cdot d\mathbf{l} \ , \qquad (2.1)$$

where θ is the angle of rotation, **B** is the magnetic field vector, L is the length of optical material impinged by the magnetic field, and V is the Verdet coefficient, a material characteristic with typical units of (minutes of an arc)/cm · Gauss. Although similar to optical activity due to circular birefringence, the sense of Faraday rotation for a given material depends only on the direction of the magnetic field, thus, polarized light reflected back through a sample will have twice the polarization rotation of a single pass [23]. Typical values of V and its temperature dependence for various materials are given in Table 1. Generally, all materials exhibit the Faraday effect, which tends to be weak for diamagnetic materials. The materials that have the greatest sensitivity to magnetic fields tend to have the greatest temperature dependence. As we will later examine, $Cd_{1-x}Mn_xTe$ is an attractive exception, having a high Verdet constant which can be made virtually temperature independent with proper choice of manganese concentration and operating wavelength. Also, note that for N turns of silica fiber encircling a current carrying wire, the amount of polarization rotation becomes independent of geometry for a uniform magnetic field:

$$\theta = VN(\mu_o I/2\pi r)(2\pi r) = \mu_o VNI \qquad (2.2)$$

Thus, an equivalent sensitivity figure for the silica fiber in Table 1 is 0.0198'/Amp · turn. In fact, the vast majority of published papers on optical current sensing examine the use of multiple fiber turns around conductors, where the proposed application is often current measurement in power substations. Measurement of high pulsed currents in the defense industry is another application area that has received attention. Since magnetic field measurement using fibers involves fairly

different considerations than using bulk materials, our work will primarily treat the latter.

Table 1. Verdet Constants and Temperature Dependence of Various Materials

Material	Verdet Constant (minutes/cm · Gauss)	Temperature Dependence
Air (@ O° C, 760 mm Hg, $\lambda = 0.578\ \mu m$)[a]	6.27×10^{-6}	not available
CO_2 (same conditions as above)[a]	9.39×10^{-6}	not available
Water (@ 20° C)[a]	0.0131	not available
Silica Fiber (diamagnetic)[b]	0.016 (typical) @ 0.633 μm	small
Quartz (@ 20° C) (diamagnetic)[a]	0.0166 @ 0.633 μm	small
NaCl (@ 16° C)[a]	0.0359 @ 0.633 μm[f]	not available
SF6 Flint Glass (diamagnetic)[c]	0.09 @ 0.87 μm	0.5% from -20° C to 80° C
FR5 Flint Glass (paramagnetic)[c]	0.11 @ 0.87 μm	30% from -20° C to 80° C
$Bi_{12}GeO_{20}$ (diamagnetic)[d]	0.188 @ 0.85 μm	2% from -25° C to 85° C
Yttrium Iron Garnet (ferromagnetic)[c]	9.0 @ 1.3 μm	25% from -20° C to 80° C
$Cd_{1-x}Mn_xTe$ (@ 40° C) (paramagnetic)[e]	10.5 @ 0.633 μm x = 0.45	Proper λ & x gives temp. independence

[a] obtained from Ref. 24
[b] obtained from Ref. 14
[c] obtained from Ref. 19
[d] obtained from Ref. 25
[e] obtained from Ref. 29
[f] wavelength implied but not explicitly given

Note: Material's magnetic clasification applies to room temperature.

As we shall see, the solution of Maxwell's equations for a plane wave entering a plasma with an applied magnetic field give two circular polarizations of opposite rotational sense. Furthermore, the differential propagation constants of these two solutions increases with applied **B**-field. Since linear polarization can be thought of as the sum of two contra-rotational circular polarizations, the application of a **B**-field will cause a rotation of the linearly polarized light.

Analyzing the Faraday effect for a given material requires the quantum mechanical theory of dispersion, considering the energy exchanges at the atomic level. As the emphasis of this research is not the detailed microscopic material behavior, we shall instead review the classical model of plane wave propagation in a plasma under the influence of an applied field in order to illuminate the general mechanisms responsible for the Faraday effect. Following this section will be a discussion of the characteristics of $Cd_{1-x}Mn_xTe$.

2.2 Faraday Rotation--General Theory

A qualitatively simple interpretation of the subsequent theory is as follows: monochromatic light radiation couples to elastically bound electrons in a substance, driving the electrons into circular orbit via the oscillating **E**-field of the light. (In general, all electrons in a solid contribute to the Faraday effect--for the optical region, conduction electrons and interband effects provide the greatest contribution [26].) Now, applying a **B**-field perpendicular to this orbit produces a force, $\mathbf{F} = e(\mathbf{E} + \mathbf{v} \times \mathbf{B})$, radially in *or* out from the center of the electrons orbit, depending on the direction of the magnetic field and the handedness of the electric field. The sum of the electron's elastic restoring force and this added **B**-field dependent force therefore give two possible values, hence, two possible values exist for the electric dipole moment, the permitivity, and the index of refraction [24]. Two wave solutions

thus exist, which we will show are circularly polarized waves of opposite rotational sense. The behavior of electromagnetic waves in a solid can be gleaned by first considering a stationary plasma where collisions are neglected and where the interaction between light and free electrons is examined (assuming that the positive ions are too massive to appreciably contribute to the effect). We will combine the methodology used in two texts for resolution of this problem [27], [28]. The last steps leading to the wave solutions, however, will use a different approach that is hopefully more convincing.

Assume the situation depicted in Fig. 2.1, where **B** is in the z direction, the propagation direction **k** is in the xz plane, and **E** is normal to **k**.

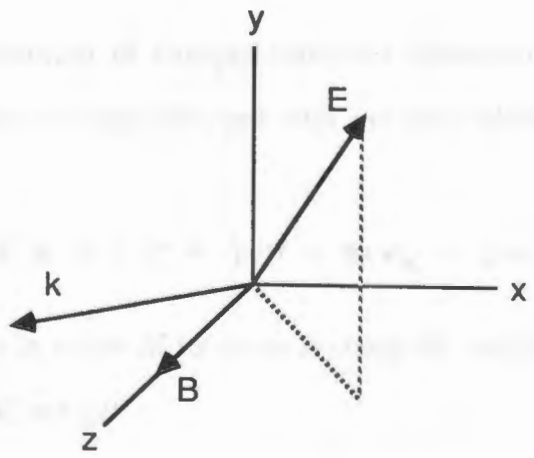

Fig. 2.1 Coordinate system for wave propagation in the plasma

Electrons moving in a magnetic field give rise to the Lorentz force, and since **E** is time varying, the electron of mass m experience a force $\mathbf{F} = m\mathbf{dv}/dt = -e(\mathbf{E} + \mathbf{v} \times \mathbf{B})$. For a uniform plane wave in an arbitrary direction we have $\mathbf{E} = \mathbf{E}_o e^{-j(\omega t - \boldsymbol{\beta} \cdot \mathbf{r})}$, where $\boldsymbol{\beta} \cdot \mathbf{r} = \beta_x x + \beta_y y + \beta_z z$. Thus,

$$-(m/e)\,dv_x/dt = E_x + v_y B_z \qquad (2.3a)$$

$$-(m/e)\,dv_y/dt = E_y - v_x B_z \qquad (2.3b)$$

$$-(m/e)dv_z/dt = E_z \tag{2.3c}$$

For a time harmonic E, we assume the particle velocity vector v is also time harmonic. Solving for the velocity components of the charged particle and defining the angular cyclotron frequency as $\omega_c = eB_z/m$ gives

$$v_x = \frac{-(e/m)(j\omega E_x - \omega_c E_y)}{\omega_c^2 - \omega} \tag{2.4a}$$

$$v_y = \frac{-(e/m)(j\omega E_y + \omega_c E_x)}{\omega_c^2 - \omega} \tag{2.4b}$$

$$v_z = (e/m)jE_z/\omega \tag{2.4c}$$

Letting the movement of charged particles constitute a conduction current, where N is the number of particles per unit volume, Maxwell's equation can be expressed by

$$\nabla \times \mathbf{H} = \mathbf{J} + j\omega\mathbf{D} = Nev_x + j\omega\epsilon_o\mathbf{E} \tag{2.5}$$

Expressing (2.5) in terms of its three rectangular components and substituting in the relations of (2.4), we get

$$(\nabla \times \mathbf{H})_x = j\omega\epsilon_o\left[1 + \frac{Ne^2}{\epsilon_o m(\omega_c^2 - \omega^2)}\right] + \frac{Ne^2\omega_c E_y}{m(\omega_c^2 - \omega^2)} \tag{2.6a}$$

$$(\nabla \times \mathbf{H})_y = j\omega\epsilon_o E_y\left[1 + \frac{Ne^2}{\epsilon_o m(\omega_c^2 - \omega^2)}\right] - \frac{Ne^2\omega_c E_x}{m(\omega_c^2 - \omega^2)} \tag{2.6b}$$

$$(\nabla \times \mathbf{H})_z = j\omega\epsilon_o E_z\left[1 - \frac{Ne^2}{\epsilon_o m\omega^2}\right] \tag{2.6c}$$

If the frequency of the plane wave entering the plasma (ω) is much greater than the angular cyclotron frequency (ω_c) then (2.6a) and (2.6b) reduce to the form of (2.6c).

Now, if $Ne^2/(\epsilon_o m\omega^2) = 1$, a critical frequency is reached for which the effective permitivity and index of refraction become zero. We define this critical frequency as

$$\omega_o = \sqrt{\frac{Ne^2}{\epsilon_o m}} \tag{2.7}$$

Substituting (2.7) into the equations of (2.6), we can write a general expression utilizing the tensor permitivity $\bar{\epsilon}$:

$$\nabla \times \mathbf{H} = j\omega\bar{\epsilon}\cdot\mathbf{E} \tag{2.8}$$

where

$$\bar{\epsilon} = \begin{bmatrix} \epsilon_{11} & -j\epsilon_{12} & 0 \\ j\epsilon_{21} & \epsilon_{22} & 0 \\ 0 & 0 & \epsilon_{33} \end{bmatrix} \tag{2.9}$$

and

$$\epsilon_{11} = \epsilon_{22} = \epsilon_o\left[1 + \frac{\omega_c^2}{\omega_c^2 - \omega^2}\right] \tag{2.10a}$$

$$\epsilon_{12} = -\epsilon_{21} = \frac{\omega_o^2\epsilon_o(\omega_c/\omega)}{\omega_c^2 - \omega^2} \tag{2.10b}$$

$$\epsilon_{33} = \epsilon_o\left[1 - \frac{\omega_c^2}{\omega^2}\right] \tag{2.10c}$$

Thus, the application of a magnetic field will generally change the permitivity tensor and, for the case where $\omega \blacktriangleright \omega_c$, the plasma remains isotropic.

It remains to determine the wave solution for TEM waves incident on a stationary plasma impinged by a magnetic field. We will examine the case where the wave propagates parallel to the magnetic field, since this is the case that occurs for

Faraday rotation. Starting with Maxwell's equations and assuming that the propagation direction and B-field are in the z direction, we have

$$\nabla \times \mathbf{E} = -j\omega\mu_o \mathbf{H} \tag{2.11}$$

$$\nabla \times \nabla \times \mathbf{E} = -j\omega\mu_o (\nabla \times \mathbf{H}) \tag{2.12}$$

$$= -j\omega\mu_o (\mathbf{J} + \delta\mathbf{D}/\delta t) \tag{2.13}$$

Since we have assumed a stationary plasma ($\mathbf{J} = 0$), we arrive at the relation

$$\nabla^2\mathbf{E} - \nabla(\nabla \cdot \mathbf{E}) + \omega^2\mu_o\mathbf{D} = 0 \tag{2.14}$$

This can be further reduced by noting that for a TEM wave propagating either parallel of perpendicular to the B-field, the E-field component or its derivative is zero in all directions, making $\nabla \cdot \mathbf{E} = 0$. Thus,

$$\nabla^2\mathbf{E} + \omega^2\mu_o\mathbf{D} = 0 \tag{2.15}$$

Since the assumed z dependence is $e^{\pm j\beta z}$, we have

$$\frac{d}{dz^2}\begin{bmatrix} E_x \\ E_y \\ 0 \end{bmatrix} + \omega^2\mu_o \begin{bmatrix} \epsilon_{11} & -j\epsilon_{12} & 0 \\ j\epsilon_{21} & \epsilon_{22} & 0 \\ 0 & 0 & \epsilon_{33} \end{bmatrix} \begin{bmatrix} E_x \\ E_y \\ 0 \end{bmatrix} = 0 \tag{2.16}$$

Which gives

$$\frac{dE_x}{dz^2} + \omega^2\mu_o(\epsilon_{11}E_x - j\epsilon_{12}E_y) = 0 \tag{2.17a}$$

$$\frac{dE_y}{dz^2} + \omega^2\mu_o(j\epsilon_{12}E_x + \epsilon_{11}E_y) = 0 \tag{2.17b}$$

Letting $E_x = E_{xo}e^{-j\beta z}$ and $E_y = E_{yo}e^{-j(\beta z + \psi)}$, we will determine E_{xo}, E_{yo}, and ψ in order to satisfy equation (2.17), and thus find the type of existing wave solution.

Making these substitutions and solving for β^2, equation (2.17a) and (2.17b) respectively become

$$\beta^2 = \omega^2\mu_o(-j\epsilon_{12}\frac{E_{yo}}{E_{xo}}e^{-j\psi} + \epsilon_{11}) \qquad (2.18a)$$

$$\beta^2 = \omega^2\mu_o(j\epsilon_{12}\frac{E_{xo}}{E_{yo}}e^{-j\psi} + \epsilon_{11}) \qquad (2.18b)$$

Solving for E_{xo} in (2.18a) and substituting it into (2.18b) yields the relation

$$\beta^4 - 2\beta^2\omega^2\mu_o\epsilon_{11} - \omega^4\mu_o{}^2(\epsilon_{12}{}^2e^{-j2\psi} - \epsilon_{11}{}^2) \qquad (2.19)$$

Solving for β gives

$$\beta = \pm\,\omega\sqrt{\mu_o(\epsilon_{11} \pm \epsilon_{12}e^{-j2\psi})} \qquad (2.20)$$

The assumed form of wave solution requires that β be real in order for energy to be propagated in the plasma. Since we defined ϵ_{11} and ϵ_{12} as real quantities, we can see from (2.20) that β has a chance of being real only if $\psi = \pi n/2$, where n = $\pm1,\pm3,\pm5,\ldots$. Thus,

$$\beta|_{\psi=\pi n/2} = \pm\,\omega\sqrt{\mu_o(\epsilon_{11} \pm \epsilon_{12})} \qquad (2.21)$$

Substituting $\psi = \pi n/2$ into (4.18a) and rearranging we get

$$E_{xo} = \pm\,\frac{\omega^2\mu_o\epsilon_{12}E_y}{\omega^2\mu_o\epsilon_{12}} = \pm\,E_{yo} \qquad (2.22)$$

Therefore, for $\epsilon_{11} > \epsilon_{12}$, β is real and we have circularly polarized wave solutions propagating in the plasma:

$$E_x = E_oe^{-j\beta z} \qquad (2.23a)$$

$$E_y = \pm jE_o e^{-j\beta z} \qquad (2.23b)$$

From the relations above, we see that the positive and negative roots of β (β_+ & β_-) in (2.21) corresponds to propagation in the +z direction and -z direction, respectively. Further, we can see that $\beta_+ = \omega\sqrt{\mu_o(\epsilon_{11} - \epsilon_{12})}$ corresponds to the propagation constant for clockwise circular polarization, $\mathbf{E}^{CW}{}_+ = \mathbf{E}^{CW}{}_+(\mathbf{x} - j\mathbf{y})$ while $\beta_+ = \omega\sqrt{\mu_o(\epsilon_{11} + \epsilon_{12})}$ corresponds to counterclockwise circular polarization, $\mathbf{E}^{CCW}{}_+ = \mathbf{E}^{CCW}{}_+(\mathbf{x} - j\mathbf{y})$. For propagation in the -z direction we have

$$\mathbf{E}^{CW}{}_- = \mathbf{E}^{CW}{}_-(\mathbf{x} + j\mathbf{y}) \qquad (2.24a)$$

$$\mathbf{E}^{CCW}{}_- = \mathbf{E}^{CCW}{}_-(\mathbf{x} - j\mathbf{y}) \qquad (2.24b)$$

which implies that $\beta^{CCW}{}_- = \beta^{CW}{}_+$ and $\beta^{CW}{}_- = \beta^{CCW}{}_+$.

Thus, the decomposed wave solutions for propagation in the +z direction (with the E-vector in the x direction at z = 0 as shown in Fig. 2) is

$$\mathbf{E}^{CW} = 0.5E(\mathbf{x} - j\mathbf{y})e^{-j\beta^{CW}z} \qquad (2.25a)$$

$$\mathbf{E}^{CCW} = 0.5(\mathbf{x} + j\mathbf{y})e^{-j\beta^{CCW}z}\ , \qquad (2.25b)$$

corresponding to right and left circularly polarized waves, respectively. The total wave solution is then

$$\mathbf{E}_T = \mathbf{E}^{CW} + \mathbf{E}^{CCW} \qquad (2.26)$$

$$= 0.5E\left[\mathbf{x}(e^{-j\beta^{CCW}z} + e^{-j\beta^{CW}z}) + j\mathbf{y}(e^{-j\beta^{CCW}z} - e^{-j\beta^{CW}z})\right]$$

$$= Ee^{-\frac{1}{2}j(\beta^{CW} + \beta^{CCW})z}\left[\mathbf{x}\cos\left[\frac{\beta^{CW} - \beta^{CCW}}{2}\right]z - \mathbf{y}\sin\left[\frac{\beta^{CW} - \beta^{CCW}}{2}\right]z\right]$$

From the above expression we note that the field vector has a fixed orientation for different z values. The angle that the E-field vector has relative to its direction at the boundary of the plasma (i.e., at $z = 0$) is shown on in Fig. 2.2.

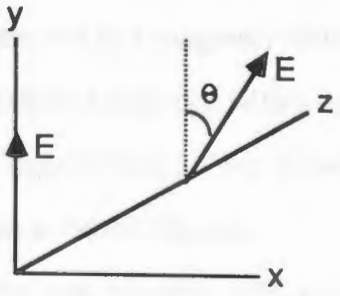

Fig. 2.2 Polarization rotation relative to plasma boundary

Solving for this angle gives

$$\tan\theta = Ey/Ex = -\tan\left[\frac{\beta^{CW} - \beta^{CCW}}{2}\right]z \qquad (2.27)$$

Thus,

$$\theta = \left[\frac{\beta^{CW} - \beta^{CCW}}{2}\right]z \qquad (2.28)$$

Therefore, we see that a linear polarized wave rotates as it passes through a plasma immersed in a magnetic field. The degree of magnetically induced circular birefringence, $\beta^{CCW} - \beta^{CW}$, generally depends on the magnitude of the B-field in the direction of wave propagation direction and the properties of the medium. As we have seen, the empirical equivalent of equation (2.28) is equation (2.1).

2.3 Properties of $Cd_{1-x}Mn_xTe$

The theoretical formulations for determining the Faraday effect will obviously depend on the material in question. Whether the necessary formulations are classi-

cal or quantum-mechanical, the common feature was demonstrated in the previous section: the medium's permitivity (or perhaps permeability) tensor changes under the influence of a magnetic field, which induces circular birefringence and produces Faraday rotation for polarized waves entering that medium.

If we are interested in a magnetic field sensor or modulator utilizing this effect, then we want to choose a material with a high Verdet constant, low absorption, and small temperature dependence. Also, as we will see, it is desirable that the material have no intrinsic linear birefringence.

A material that has recently received attention in the literature as a candidate for optical isolators, modulators, and Faraday effect magnetic field sensors is $Cd_{1-x}Mn_xTe$ (cadmium manganse telluride), a zinc blende semi-magnetic semiconductor with all the aformentioned attributes [29], [30]. Its Verdet constant varies with operating wavelength and manganese concentration, and can be nearly 1000 times greater than silica. The large Verdet constant in $Cd_{1-x}Mn_xTe$ is due to an exchange interaction between localized manganese spins and mobile carriers in the conduction and valence bands. The Verdet constant for the interband Faraday effect in magnetic semiconductors can be approximately expressed by

$$V = V_o \frac{H_{eff}}{H_o} F(\omega/\omega_g) \qquad (2.29)$$

where V_o is a constant dependent on the band parameters, H_o is the applied magnetic field, and $F(\omega/\omega_g)$ is a function giving the wavelength dependence with a singularity at the band edge, $\omega = \omega_g$. The effective magnetic field is given by

$$H_{eff} = H_o \left[1 + \frac{J\chi(T)}{N_s(g\mu)^2}\right] \qquad (2.30)$$

where J is the exchange interaction between localized spins and charge carriers in the conduction and valence bands, $\chi(T)$ is the temperature dependent paramagnetic susceptibility, N_S is the concentration of localized spins (residing on the Mn atoms), g is an average g factor, and μ is the Bohr magneton [31]. $Cd_{1-x}Mn_xTe$ is paramagnetic above ~ 15° K [32]. Its band gap is linearly variable with manganese concentration, and is given by $E_g = 1.620 + 1.34x - 5.56 \times 10^{-4} T(^\circ K)$ [33].

Good quality single-phase crystals have been grown using the vertical Bridgeman method with manganese concentrations of up to 70 percent, corresponding to free space wavelengths of roughly 0.855 μm to 0.52 μm at room temperature. Absorption coefficients above the bandgap depend on Mn concentration, but are on the order of 1 cm^{-1}.

Another interesting property of this material is that the Verdet constant can be rendered temperature independent at a given operating wavelength by varying the manganese concentration. This is possible because although the rotation decreases with increasing temperature well above the band gap, the rotation also increases rapidly as the wavelength approaches the band gap, thus allowing for a point where these two effects can cancel [33].

Frequency response of the material depends on optical transit time through the crystal and the intrinsic spin reorientation time. The bandwidth of the former can be approximated by $BW = 0.6c/nL$, where c is the free space light velocity, n is the refractive index of the crystal, and L is the length of the crystal. The time needed for localized Mn spins to reorder is sub-nanosecond, and translates into a BW of about 3.5 GHz for Mn = 0.45 percent (x = 0.45). Thus, the greatest amount of Faraday rotation at maximum bandwidth (corresponding to L = 1.5 cm) for this case is approximately 0.25° /Gauss [31]. The ultimate sensitivity of this material as a magnetic sensor will then depend on the minimum amount of measurable rotation,

which we examine in chapter 4.

CHAPTER 3 ◊ VERDET CONSTANT MEASUREMENT IN $Cd_{1-x}Mn_xTe$

We measured the Verdet constant of a 3.63 mm thick crystal sample with a manganese concentration of 50 percent. This percentage of Mn was set before the actual crystal growth process, so the actual percentage of manganese in our sample might vary slightly (maybe ± 5%) due to an inhomogeneous melt during crystallization. Fortunately, the crystal sample had a side that was roughly one degree off from being perfectly parallel with the other side (see Appendix 3). Therefore, multiple light reflections did not have to be considered for the calculation of the single pass Verdet constant. Perfectly parallel crystal sides would have given a Fabry-Perot cavity, which would have necessitated a correction to the measured polarization rotation due to light multiply reflected in the cavity before exiting [34]-[36]. Such corrections can be especially important for accurately determining the effective mass in semiconductors, as illustrated by the effective mass equation for direct gap semiconductors,

$$m^* = \omega \sqrt{\frac{2Vnc\epsilon_o}{Ne^3}} \qquad (3.1)$$

where ω is the frequency of incident light, V is the Verdet constant, n is the refractive index of the material, c is the free space speed of light, ϵ_o is the vacuum permitivity, e is the electron's charge, and N is the number of charge carriers per unit volume [37].

The configuration used to measure the Verdet constant is shown in Figure 3.1. By simply measuring the change in intensity at the detector for a known B-field,

we can infer the amount of polarization rotation using Malus's law. Figure 3.2 helps define the variables used in the following formulation. Other definitions are as follows:

I_D = Intensity at detector in Figure 3.1 without an applied **B**-field

I_D' = Intensity at detector in Figure 3.1 with an applied **B**-field

I_S = Source Intensity, and γ = System power loss factor

Refering to Figure 3.1 and 3.2 we have

$$I_D = \gamma I_S \cos^2\theta_B \tag{3.2}$$

$$I_D' = \gamma I_S \cos^2(\theta_B \pm \Delta\theta)$$

$$= I_D\left[\frac{\cos(\theta_B \pm \Delta\theta)}{\cos\theta_B}\right]^2 \tag{3.3}$$

Solving for positive $\Delta\theta$ in (3.3) gives

$$\Delta\theta = \cos^{-1}\left[(I_D'/I_D)^{\frac{1}{2}}\cos\theta_B\right] - \theta_B \tag{3.4}$$

To avoid errors due to a possibly unstable laser output, we will continuously remeasure the intensity under no field conditions. The analyzer was tilted 45 degrees with respect to the input polarizer in order to operate in the most linear portion of the Intensity verses $\Delta\theta$ curve.

From work presented in Appendix 2, we have an empirical relationship between the applied coil current and the magnetic field at various distances above the gap. These measurements were made with a Hall effect magnetometer. In Figure 3.1, the coil-crystal assembly was attached to an x-y-z positioner in order to (1) conveniently find the clearest spot for the laser beam to minimize scattering and maximize the degree of polarzation, and (2) to accurately position the beam at the same location above the coil gap where the coil current verses **B**-field is measured

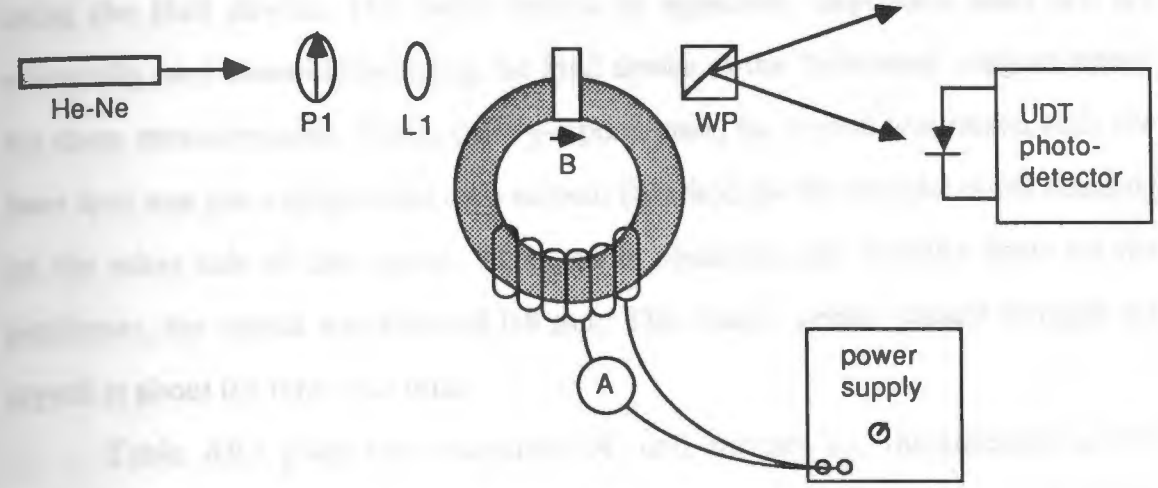

He-Ne: 4 mW laser @ 0.633 μm
P1: Polarizer
L1: Microscope objective--NA=0.1; distance from lens front to crystal:1.60 cm
WP: Wollaston prism--principle axis @ 45 degrees to P1
Distance from crystal to detector: 11.5 cm

Figure 3.1 Set-up for determining Verdet constant

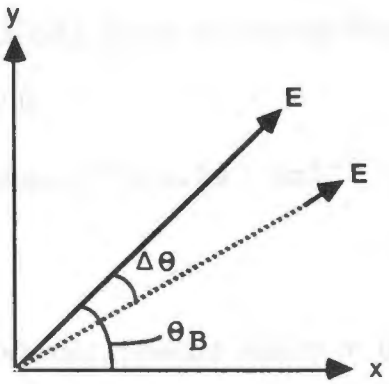

x axis corresponds to
WP analyzer alignment

θ_B : Angle "bias" of E with respect to analyzer without an applied B-field

$\Delta\theta$: Change in polarization angle after an applied B-field

Figure 3.2 Polarization orientation to analyzer

using the Hall device. This latter reason is especially important since we are essentially (and unavoidably) using the Hall device as the "reference" magnetometer for these measurements. Using the x-y-z positioner, the crystal was raised until the laser spot was just extinguished on a screem (blocked by the toroidal core) standing on the other side of the crystal. Then, while observing the distance scale on the positioner, the crystal was lowered 0.8 mm. The beam's center passed through the crystal at about 0.8 mm ± 0.1 mm.

Table A9.1 gives the measured DC coil current I_C, the intensity at the detector with that applied current, I_D', and the intensity at the detector with no applied current, I_D. Again, I_D is remeasured within about 10 seconds from the I_D' measurement to correct for any laser output drift. Also in Table A9.1 is the calculated angle of Faraday rotation and the calculated B-field at 0.8 mm above the gap. This calculation is based on the empirical relationship given in Appendix 2.

Figures 3.3 through 3.6 are plots of the data in Table A9.1 for different ranges of B. In Figure 3.3 we see that the coil assembly begins to saturate above about 400 Gauss; below this the plot is linear as expected. From Figure 3.4 we note that the slope is about 0.0533. Since the crystal thickness was measured to be 3.63 mm, the Verdet constant is

$$(0.0533 \text{ degrees} \cdot \text{Gauss}^{-1})(0.363 \text{ cm})^{-1} = 0.147' \text{ cm}^{-1} \cdot \text{Gauss}^{-1}$$

$$= \underline{\underline{8.8' \text{ cm}^{-1} \cdot \text{Gauss}^{-1}}}$$

This value is close to Verdet constant values in the literature for similar crystal compositions. As a comparison, Martin and Butler [29] reported a Verdet constant at room temperature of about 10.2' $cm^{-1} \cdot Gauss^{-1}$ for $Cd_{.55}Mn_{.45}Te$ at 0.633 μm; Turner, Gunshn, and Datta [30] reported a Verdet constant for $Cd_{.55}Mn_{.45}Te$ at room temperature and 0.633 μm of about 7.2' $cm^{-1} \cdot Gauss^{-1}$. The difference

between these latter two values might be partially due to the error in assessing the actual Mn concentration, since this affects the Verdet constant for a given wavelength.

Certainly the greatest source of error in determining the Verdet constant in this particular set-up is the measurement of the **B** field above the gap. The primary uncertainty lies in the distance measured above the gap. From Appendix 2, this uncertainty translates into a tolerance of about ±20 percent on the value found for the Verdet constant. Despite this, the obtained value is quite reasonable. This tolerance could have been considerably tightened using a solenoid magnetic field generator, but the field generated would not have been as high for the reasons given in Appendix 2.

Also, from Figure 3.6 we note that the minimum resolution of $\Delta\theta$ ($\Delta\theta_{min}$) was about 0.1°, corresponding to a minimum resolvable field of 1 Gauss for this sample.

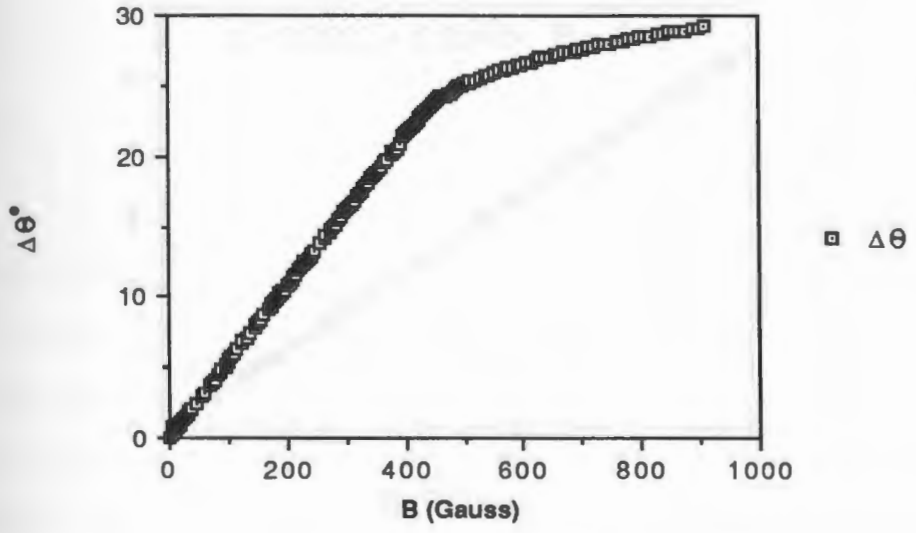

Fig. 3.3 Polarization rotation vs. B-field: 0-1000 Gauss

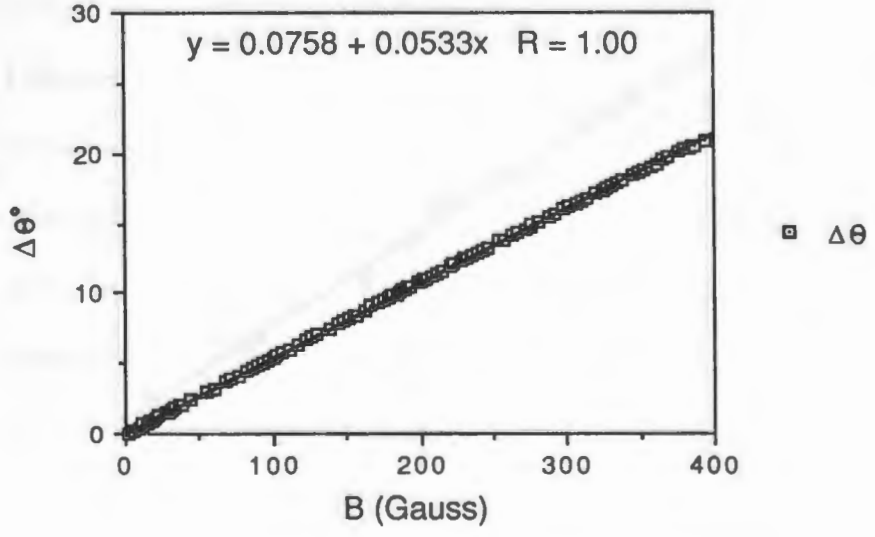

Fig. 3.4 Polarization rotation vs. B-field: 0-400 Gauss

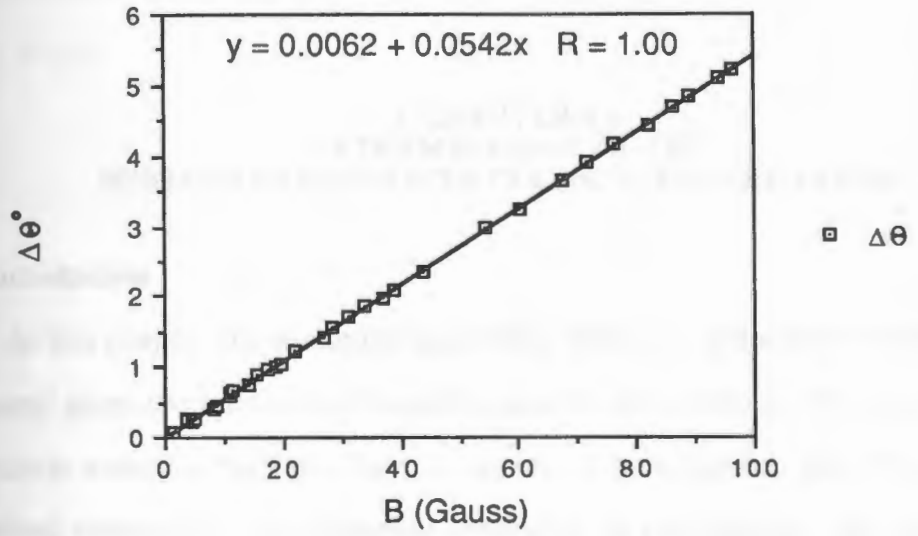

Fig. 3.5 Polarization rotation vs. B-field: 0-100 Gauss

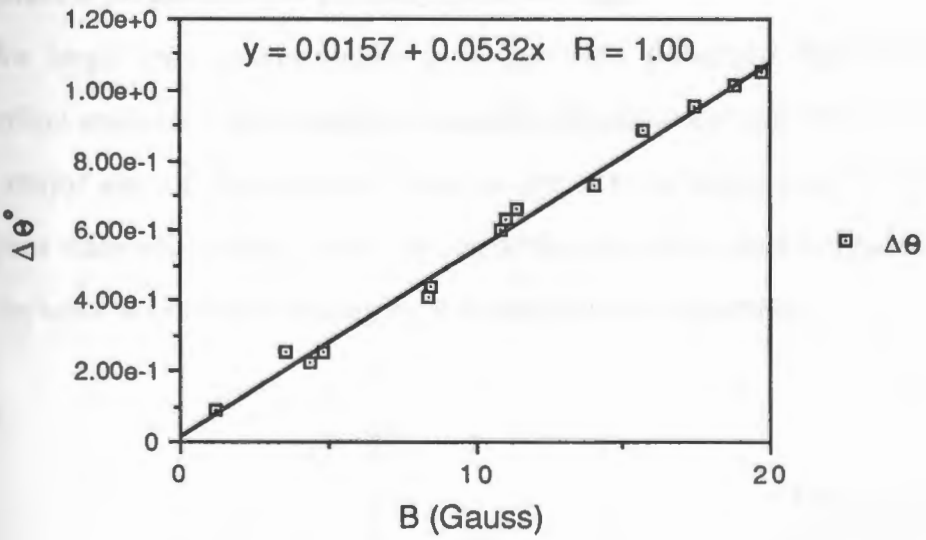

Fig. 3.6 Polarization rotation vs. B-field: 0-20 Gauss

◊ CHAPTER 4 ◊
DETERMINATION OF THE MINIMUM RESOLVABLE POLARIZATION ROTATION

4.1 Introduction

In this chapter the minimum resolvable change in polarization angle ($\Delta\Theta$) will be found given the minimum allowable signal-to-noise ratio at the detector. We will ultimately consider the laser beam's degree of polarization, the ellipticity of the polarized component, the extinction coefficient of the analyzer, the detector noise, and the intensity of the light exiting the Faraday material. Finally, we will use this analysis to estimate the $\Delta\Theta$ resolution of our experiment. Knowing this will allow estimation of the minimum detectable magnetic field.

4.2 Affect of an analyzer on partially polarized light

We begin with a consideration of perfectly polarized light incident on an imperfect analyzer with orthogonal intensity transmission coefficients of k_1 and k_2. The major axis of the elliptical polarization is at an angle φ with respect to the analyzer transmission axis, which for convenience is the x axis in Figure 4.1. a and b are the semi-major and semi-minor axis magnitudes, respectively.

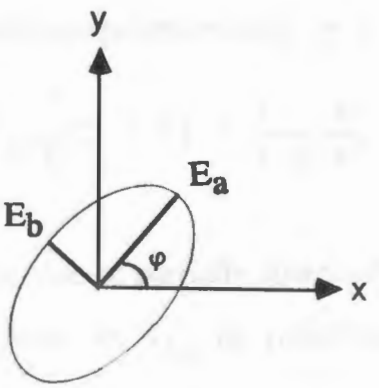

Fig. 4.1 Elliptical polarization incident on anaylzer

Defining the electric field phasors for the major and minor axes of the polarization ellipse incident on the analyzer as $\mathbf{E}_a$ and $\mathbf{E}_b$, we find the total transmitted intensity I_o as follows [38]:

$$\mathbf{E}_a = ae^{j\omega t} \tag{4.1a}$$

$$\mathbf{E}_b = be^{j(\omega t-\pi/2)} = -jbe^{j\omega t} \tag{4.1b}$$

$$\mathbf{E}_x = (ae^{j\omega t}\cos\varphi + jbe^{j\omega t}\sin\varphi) \tag{4.2a}$$

$$\mathbf{E}_y = (ae^{j\omega t}\sin\varphi - jbe^{j\omega t}\cos\varphi) \tag{4.2b}$$

The intensity transmission on the x and y axes is

$$I_{xo} = k_1(\mathbf{E}_x \cdot \mathbf{E}_x^*) \tag{4.3a}$$

$$= k_1(a^2\cos^2\varphi + b^2\sin^2\varphi) \tag{4.3b}$$

$$I_{yo} = k_2(\mathbf{E}_y \cdot \mathbf{E}_y^*) \tag{4.4a}$$

$$= k_2(a^2\sin^2\varphi + b^2\cos^2\varphi) \tag{4.4b}$$

Letting the total intensity out of the analyzer be I_o we have

$$I_o = I_{xo} + I_{yo}$$

$$= 0.5k_1[a^2(1 + \cos2\varphi) + b^2(1 - \cos2\varphi)] + 0.5k_2[a^2(1 - \cos2\varphi) + b^2(1 + \cos2\varphi)]$$

$$= 0.5[(k_1 + k_2)(a^2 + b^2) + (a^2 - b^2)(k_1 - k_2)\cos2\varphi]$$

Defining the total light input to the analyzer as $I_{in} = a^2 + b^2$, the extinction ratio of the analyzer as $k_2/k_1 = \zeta$, and the ellipticity of the input polarization as as $\rho = b/a$ ($\rho = 1$ = circular polarization; $\rho = 0$ = linear polarization), we get

$$I_o = \frac{1}{2} k_1 I_{in}\left[(1 + \zeta) + \frac{1 - \rho^2}{1 + \rho^2}(1 - \zeta)\cos2\varphi\right] \tag{4.5}$$

To extend (4.5) for the case of partially polarized light, we define the fraction of unpolarized light as q. Now, let I_{in} be redefined as the total input intensity

including polarized (I_p) *and* unpolarized light (I_u):

$$I_{in} = I_p + I_u = I_p + qI_{in}. \tag{4.6}$$

Since (4.5) is for purely polarized light, I_{in} is identical to I_p in this equation. For the case where we have a mix of polarized and unpolarized light, we can define I_{in} from (4.6) as $I_{in} = I_p/(1 - q)$. For partially polarized light we thus have

$$I_o = \frac{I_{in}}{2} k_1(1 - q)(1 + \zeta)\left[1 + \frac{1 - \rho^2}{1 + \rho^2}(1 - \zeta)\cos 2\varphi\right] + \frac{I_{in}}{2} qk_1(1 + \zeta) \tag{4.7}$$

where the first term is the output intensity of the polarized light and the second term is the output intensity of the unpolarized light. Simplifying (4.7) we get

$$I_o = \frac{I_{in}}{2} k_1(1 + \zeta)\left[1 + (1 - q)\left[\frac{1 - \rho^2}{1 + \rho^2}\right]\left[\frac{1 - \zeta}{1 + \zeta}\right]\cos 2\varphi\right] \tag{4.8}$$

4.3 Output intensity change due to a change in polarization angle

Guiding this formulation further we take the more pertinent case of Figure 4.1 and assume that under no field conditions the major axis of the polarization ellipse makes an angle with respect to the analyzer of θ_B. The *change* in polarization orientation from this "bias" angle due to the Faraday effect will be designated by $\Delta\theta$. Thus, $\varphi = \theta_B + \Delta\theta$ in (4.8). $\Delta\theta$ translates into a change in output intensity $I_o(\Delta\theta)$.

$$\Delta I_o(\Delta\theta) = I_o(\varphi = \theta_B) - I_o(\varphi = \theta_B + \Delta\theta) \tag{4.9}$$

where I_o is defined in (4.8). For the common case where $\theta_B = 45°$, equation (4.9) becomes the following:

$$\Delta I_o(\Delta\theta) = \frac{I_{in}}{2} k_1(1 - q)\left[\frac{1 - \rho^2}{1 + \rho^2}\right]\left[\frac{1 - \zeta}{1 + \zeta}\right]\sin 2\Delta\theta \qquad (4.10)$$

4.4 Signal-to-noise ratio of detected rotation $\Delta\theta$

By determining the minimum change in output intensity ΔI_{omin} that we can detect, the minimum detectable polarization change resolution $\Delta\theta_{min}$ can be found. We start with the general equation for the voltage signal-to-noise ratio at the photodetector, considering shot and thermal noise [39]:

$$\frac{S}{N} = \frac{(M\eta e I/hf)}{\sqrt{4\kappa T\Delta f/R_L} + \sqrt{2e\Delta f M^n[(\eta e I/hf) + I_d)}} \qquad (4.11)$$

where
- M = photodetector gain
- n = excess noise factor (for avalanche photodiodes)
- η = quantum efficiency of detector
- e = electron charge
- I = signal intensity
- h = 6.626×10^{-34} J·s
- f = frequency of light
- κ = 1.38×10^{-23} J/K
- T = temperature in °K
- Δf = receiver bandwidth (Hz)
- R_L = load resistance (Ω)
- I_d = dark current of photodiode

The intensity that causes shot noise and the intensity change that represents a signal are not the same in this case. I in the shot noise term will be the total intensity at the photodetector, and I in the signal term will be the change in the intensity $\Delta I_o(\Delta\theta)$ due to Faraday rotation. Making these substitutions in (4.11) yields the new signal-to-noise ratio (SNR):

$$\frac{0.5k_1 I_{in}(M\eta e/hf)(1 - q)\left[\frac{1 - \rho^2}{1 + \rho^2}\right]\left[\frac{1 - \zeta}{1 + \zeta}\right]\sin 2\Delta\theta}{\sqrt{M^n 2e\Delta f\left[I_d + \tfrac{1}{2}I_{in}k_1(\eta e/hf)\left[1-(1-q)(1-\zeta)\frac{1 - \rho^2}{1 + \rho^2}\sin 2\Delta\theta\right]\right] + N_{th}}} \qquad (4.12)$$

where N_{th} is the thermal noise term $[4\kappa T\Delta f/R_L]^{\frac{1}{2}}$.

The thermal noise term for PIN detectors will dominate for load resistances above about 1 MΩ. Since a practical magnetometer using a crystal might especially be useful for high frequency measurements, the load resistance would likely be lower than this in order to keep the RC time constant small. If an avalanche photodiode was used, however, shot noise could dominate. For now we will include both thermal and shot noise terms.

We are interested in what change in polarization orientation is sufficient to produce a change in output light intensity that is above the detector's noise level. Since we are interested in small $\Delta\theta$, we can simplify the expression of (4.12) by neglecting the $\sin 2\Delta\theta$ term in the shot noise term. Doing this and solving for $\Delta\theta$ in (4.12) gives a closed form expression for the minimum detectable rotation $\Delta\theta_{min}$ given the desired minimum SNR:

(4.13)

$$\Delta\theta_{min} = \tfrac{1}{2}\sin^{-1}\left[\frac{SNR\left[\sqrt{M^n 2e\Delta f[I_d + \tfrac{1}{2}k_1(\eta e/hf)(1+\zeta)I_{in}}\right] + N_{th}}{(M\eta e/2hf)k_1 I_{in}(1-q)\frac{(1-\rho^2)(1-\zeta)}{(1+\rho^2)(1+\zeta)}}\right]$$

Consider an example of perfectly polarized light ($\rho = q = 0$), a good analyzer ($\zeta \to 0$), and a PIN photodetector ($M = 1$) with the following parameters:

I_{in} = 1 mW, k_1 = 0.5, η = 0.5, T = 300°K, Δf = 5000 Hz, R_L = 1000 Ω, I_d = 2 nA and SNR = 5.

Using these values in (4.13) gives $\Delta\theta_{min} = 0.00136°$. Converting this to a minimum measurable B-field we get from (2.1)

$$B_{min} = \Delta\theta_{min}/VL \qquad (4.14)$$

For $V = 0.16° cm^{-1} G^{-1}$ and $L = 1$ cm, $B_{min} = 0.00853$ Gauss. This resolution might be possible for a very stable system.

There is another important consideration when determining the minimum resolvable rotation. If the applied field in Figure 3.1 is DC, then the change in intensity, ΔI_o,--though it may be greater than the detector noise--might be unresolvable because the total intensity illuminating the detector, $I_o(\varphi \simeq \theta_B)$, may be so much greater than $\Delta I_o(\Delta\theta)$ that the change in electrical power at the detector is unmeasurable. For instance, in the previous example the change in rms signal voltage at the detector, V_s, due to the calculated rotation change $\Delta\theta = 0.00136°$ is

$$V_s = 0.5 I_{in} R_L^{\frac{1}{2}} (\eta e/hf) k_1 \sin 2\Delta\theta = 9.56 \times 10^{-8} \text{ volts}$$

but the voltage signal at the detector for no rotation ($\Delta\theta = 0 \rightarrow \varphi = \theta_B = 45°$) is

$$V_o = 0.5 I_{in} R_L^{\frac{1}{2}} (\eta e/hf) k_1 = 2.01 \times 10^{-3} \text{ volts}$$

Clearly, even if our detection circuit or voltmeter has the required sensitivity (in this case, down to $\sim 10^{-8}$ volts), the measuring instrument may not be able to resolve V_s since V_o could overload the instrument on the scale of required sensitivity. If we set our hypothetical voltmeter to the 10^{-4} scale, it would be pointless to try to measure the 9.56×10^{-8} voltage unless the readout had a resolution out to 10^{-8} volts.

The situation changes, however, for a time-changing $\Delta\theta$. For a sinusoidal B-field in the set-up of Figure 3.1, the changing polarization angle can be expressed as $\Delta\theta \sin\omega t$. For perfectly linearly polarized light and a perfect analyzer ($\zeta \rightarrow 0$), we let $\varphi = 45° + \Delta\theta \sin\omega t$ in equation (4.8) to get the corresponding "modulated" output intensity:

$$I_o(\varphi = 45° + \Delta\theta \sin\omega t) = 0.5 I_{in} k_1 [1 - \sin(2\Delta\theta \sin\omega t)]$$

For small $\Delta\theta$ this reduces to

$$I_o(\varphi = 45 + \Delta\theta\sin\omega t) = 0.5I_{in}k_1(1 - 2\Delta\theta\sin\omega t) \qquad (4.15)$$

The corresponding signal voltage of the PIN detector is then

$$V_s = 0.5I_{in}k_1(\eta e/hf)R_L^{\frac{1}{2}}(1 - 2\Delta\theta\sin\omega t) \qquad (4.16)$$

Now, since the information we are interested in is sinusoidal, we can AC-couple this voltage to our hypothetical voltmeter and not worry as before about the desired signal being "masked" by the larger DC signal.

Sensitivity for $\theta_B = 90°$

For the case where the major axis of the input polarization ellipse is orthogonal to the analyzer under no field conditions in Figure 3.1 and 3.2, we find the minimum resolvable rotation angle. Using equation (4.8) we let $\varphi = 90° + \Delta\theta$ and substitute into (4.9) to find the ouput intensity change for a rotation $\Delta\theta$. For the typical case of linearly polarized light, a small $\Delta\theta$ will give only a small intensity at the photodetector, so we will neglect shot noise. Doing this and solving for $\Delta\theta$ gives

(4.17)

$$\Delta\theta_{min} = \sin^{-1}\left[\frac{SNR\sqrt{4\kappa T\Delta f/R_L}}{I_{in}k_1(\eta e/hf)(1 - \zeta)(1 - q)(1 - \rho^2)/(1 + \rho^2)}\right]^{\frac{1}{2}}$$

Using the same parameters as in the example on page 31 (which was for $\theta_B = 45°$), we get $\Delta\theta_{min} = 0.193°$. Biasing the analyzer at $\theta_B = 90°$ gives the least angle resolution since, from Malus's law, $\cos^2(\theta_B + \Delta\theta)$ changes slowest for $\theta_B = 90°$.

4.5 Theory related to experiment

In our measurement of the Verdet constant earlier, the smallest discernable $\Delta\theta$ was $\sim 0.09°$. Though we were unable to get exact noise specifications on the UDT photodetector, we can theoretically find the smallest measurable rotation angle $\Delta\theta_{min}$ given the resolution of the instrument. Under no field conditions, the optical

intensity in Figure 3.1 was 9.23×10^{-5} Watts, and the scale on the digital intensity meter was 10^{-5} Watts with resolution down to 10^{-7} Watts. Using the form of (4.12) and letting 10^{-7} Watts correspond to the noise level of our instrument, we can estimate the minimum resolvable rotation that we should have observed in our experiment:

$$SNR = \frac{(\text{total intensity at the photodiode})\sin 2\Delta\theta}{(\text{noise level of instrument})} = 1$$

$$= \frac{(9.23 \times 10^{-5} \text{ Watts})\sin 2\Delta\theta}{(10^{-7} \text{ Watts})} = 1$$

Solving for $\Delta\theta$ gives $\Delta\theta_{min} = 0.03°$, compared to the experimental $\Delta\theta_{min}$ of $\sim 0.09°$. This is the best resolution in $\Delta\theta$ that we could possibly have attained using the particular set-up in Figure 3.1. If not for a slight laser output drift, this resolution could probably have been achieved in the experiment.

If, hypothetically, our detector had a resolution of 10^{-9} Watts, then the theoretical limit to $\Delta\theta_{min}$ would be $3 \times 10^{-4}°$. The next question is whether or not this is practically possible--what else might degrade resolution? The most obvious degrading factor is laser output drift, but using signal processing such drift could probably be normalized out, leaving noise from the processing electronics as the dominate resolution limitation. Because of equipment limitations, we were unable to explore this point. In addition, it would seem that crystal quality might also be a factor. After all, if the crystal's properties are slightly inhomogeneous, it is possible that the observable Faraday effect might have a bottom limit in terms of magnetic field, where **B** versus the *inferred* $\Delta\theta$ is no longer linear and "well behaved."

4.6 Measured degree of polarization out of crystal.

In our examples we have been assuming that our linear input polarization

remains linear at the output. Since our material is non-birefringent under no field conditions, this is a valid assumption. However, in case there were any inhomogeneities in our sample that might lead to linear birefringence, we measured the degree of polarization (D.O.P) anyway. The method was simply to rotate the Wollaston prism in Figure 3.1 for a minimum and maximum intensity as measured by the UDT photodetector. By definition [23],

$$D.O.P. = \frac{I_{max} - I_{min}}{I_{max} + I_{min}} \qquad (4.18)$$

For the set-up used to meaure the Verdet constant, the measured values were $I_{max} = 2.00 \times 10^{-4}$ Watts, and $I_{min} = 9.85 \times 10^{-8}$ Watts. Thus, D.O.P. = 0.99901. Also, the absorption coefficient for $Cd_{1-x}Mn_xTe$ with $B \neq 0$ differs for left and right circular polarization as predicted by the Kramers-Kronig relations; input light would be slightly elliptical at the output [26]. For most cases including ours, however, this effect is insignificant.

4.7 Dynamic range of measurement

A related specification of interest is the range over which we can measure magnetic fields. Keeping in mind that the change in polarization angle $\Delta\theta$ is proportional to the magnetic field, we will define this dynamic range (D.R.) as

$$D.R. = \frac{\text{maximum measurable } \Delta\theta}{\text{minimum measurable } \Delta\theta} \qquad (4.19)$$

The minimum measurable $\Delta\theta$ has already been discussed. The maximum measurable $\Delta\theta$ depends on (1) the allowable tolerance for error, and (2) the complexity of the sensing method. Going back to the set-up of Figure 3.1, the theoretical change in voltage at the PIN load resistor for a Faraday rotation of $\Delta\theta$ is

$$\Delta V = 0.5 I_{in} k_1 (\eta e/hf) R_L^{\frac{1}{3}} (1 - q) \left[\frac{1 - \rho^2}{1 + \rho^2}\right] \left[\frac{1 - \zeta}{1 + \zeta}\right] \sin 2\Delta\theta \qquad (4.20)$$

Note from (4.20) that ΔV versus $\Delta\theta$ is linear only for the approximation $\sin 2\Delta\theta \simeq 2\Delta\theta$. This is linear to within ~1 percent for $2\Delta\theta < 12°$, and to within ~2 percent for $2\Delta\theta < 20°$. As an example, for an error of less than 1 percent and a minimum measurable rotation of 0.001°, the dynamic range is 6°/0.001 = 6000 : 1.

More sophisticated sensing systems do not rely on the linear portion of the ΔV versus $\Delta\theta$ curve to operate. Equation (4.20) can be numerically inverted to obtain $\Delta\theta$ and thus a magnetic field magnitude. Other systems actually count multiple polarization rotations, thus affording large dynamic ranges [40]. Magneto-optic sensors at Los Alamos, for instance, utilize digital storage scopes to count multiple rotations for high pulsed magnetic field measurements [41].

4.8 Verdet constant measurement--an alternate method

A more common method of examining the optical Faraday effect uses the basic configuration shown in Figure 4.2.

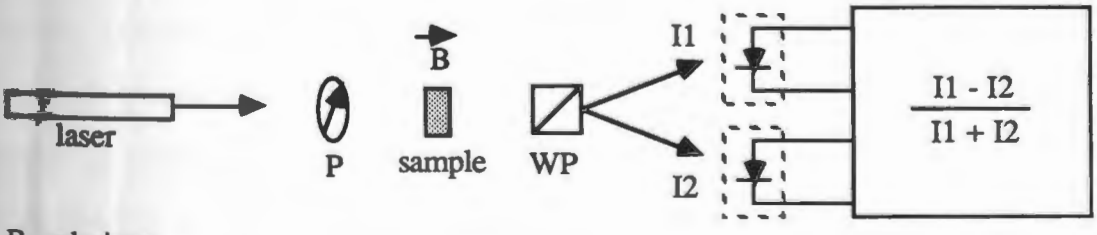

P: polarizer
WP: Wollaston prism
note: under no-field condtions, the WP axes are 45°
from the input polarization, thus, I1 = I2 when B = 0.

Fig. 4.2 Ratiometric Faraday rotation measurement

The intensities of the two beams are detected separately and the output of the detectors are connected to an electronic signal divider. Assuming a linearly polarized beam incident at the Wollaston prism with electric field amplitude E_{in}, we have

$$I_1 = E_{in}^2 \cos^2(\pi/4 + \Delta\theta) \qquad (4.21a)$$

$$I_2 = E_{in}^2 \sin^2(\pi/4 + \Delta\theta) \qquad (4.21b)$$

$$\frac{I_1 - I_2}{I_1 + I_2} = \sin 2\Delta\theta \qquad (4.22)$$

Thus, the operation of (4.22) renders $\Delta\theta$ independent of changes in the intensity of the light source [42].

Analog dividers are available up to roughly 10 MHz for time-varying intensities. For applications requiring faster response times such as in the measurements of pulsed magnetic fields, I_1 and I_2 can be stored for digital processing.

CHAPTER 5 ◊ FIBER-LINKED SENSOR--THEORY

5.1 Introduction

A number of schemes have been proposed to link Faraday effect magneto-optic sensors via optical fibers. All share the advantage of conveniently locating the light source away from the measurement point [29], [33], [43]. One scheme, however, offers the additional advantage of cancelling the degrading effects of fluctuating propagation characteristics in the fiber link. The method is known as polarization-rotated reflection, and was originally used as a means of stabilizing the temperature performance of electro-optic light modulators by cancelling the temperature dependent birefringence [44]. An ideal system without any sensor is shown in Figure 5.1 to demonstrate the principle of operation. The fiber is polarization-maintaining with eigenaxes in directions x and y. The attentuation and propagation constants along the eigenmodes are $\alpha_{x,y}$ and $\beta_{x,y}$, respectively. Following Figure 5.1, linearly polarized light transverses the beamsplitter and equally excites the polarization eigenmodes. The linear birefringence of the fiber yields an output electric field of arbitrary polarization ellipticity which, after having twice transversed the QWP by reflecting back from the mirror, now has its E components oriented orthogonal to their original orientation just after exiting the fiber output. Thus, the forward travelling electric vector along the x direction now travels back along the fiber with direction along y; the incident and reflected electric field vectors have "traded" places. After round trips, the input waves on each polarization axis have experienced the *same* phase shift $e^{-j(\beta_x + \beta_y)\ell}$ and the *same*

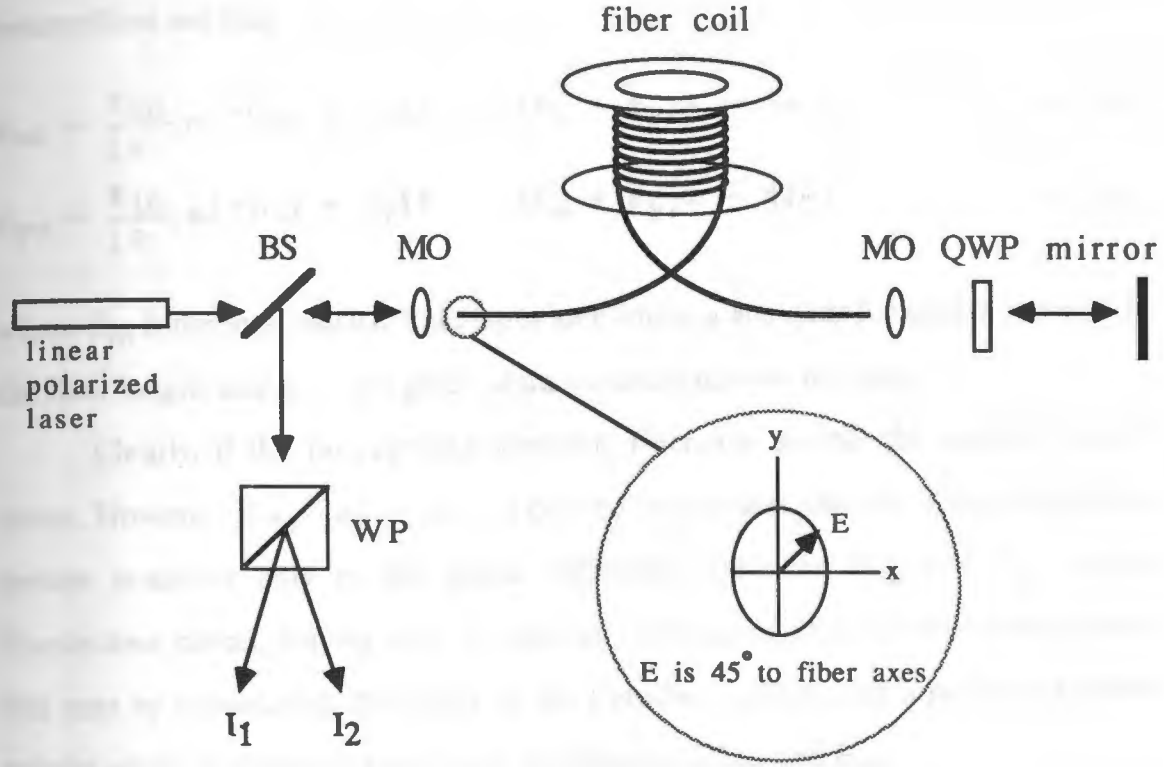

BS: beamsplitter
QWP: quarter wave plate
MO: microscope objective
WP: Wollaston prism

Fig. 5.1 Basic polarization-rotated reflection scheme

attenuation $e^{-(\alpha_x + \alpha_y)\ell}$ in the fiber. The returned electric field outputs from the beamsplitter are thus

$$E_{xo} = \frac{E_{in}}{\sqrt{2}}\gamma e[-(\alpha_x + \alpha_y)\ell - j(\beta_x + \beta_y)\ell - j\phi_1] \qquad (5.1a)$$

$$E_{yo} = \frac{E_{in}}{\sqrt{2}}\gamma e[-(\alpha_x + \alpha_y)\ell - j(\beta_x + \beta_y)\ell - j\phi_2] \qquad (5.1b)$$

where E_{in} is the total electric field input amplitude, γ accounts for system losses, ℓ is the fiber length, and $\phi_{1,2}$ are phase shifts occuring outside the fiber.

Clearly, if the propagation constants fluctuate, so will the output waves's phase. However, if $\phi_1 - \phi_2 = \Delta\phi$ is a desired measurand, then by using a detection system sensitive only to the phase difference between E_{xo} and E_{yo}, these fluctuations cancel, leaving only the desired information, $\Delta\phi$. We will demonstrate this next by considering the effect of the Faraday medium and a polarizing beam splitter which is oriented to mix equal amplitudes of E_{yo} and E_{xo}.

Referring to Figure 5.2, the linear wave components are transformed into circularly polarized waves by the QWP. With an applied magnetic field, the clockwise and counterclockwise polarized waves in the Faraday medium have propagation constants β^{CW} and β^{CCW}, respectively. Assuming that the only phase shifts outside the fiber occur in the non-reciprical Faraday crystal of length L, $\phi_1 = 2\beta^{CW}L$ and $\phi_2 = 2\beta^{CCW}L$. The factor of two accounts for the bidirectional transmission through the crystal. The amount of polarization rotation in the crystal is then $\phi_1 - \phi_2 = 2\theta_F = 2(\beta^{CW} - \beta^{CCW})L = 4VLB$, where V is the Verdet constant of the crystal, L is the length of the crystal, and B is the magnetic field component in direction of propagation (see equation 2.1). Now, with the polarizing axes of the beamsplitter at 45° with respect to E_{yo} and E_{xo}, we get the following output intensities [43]:

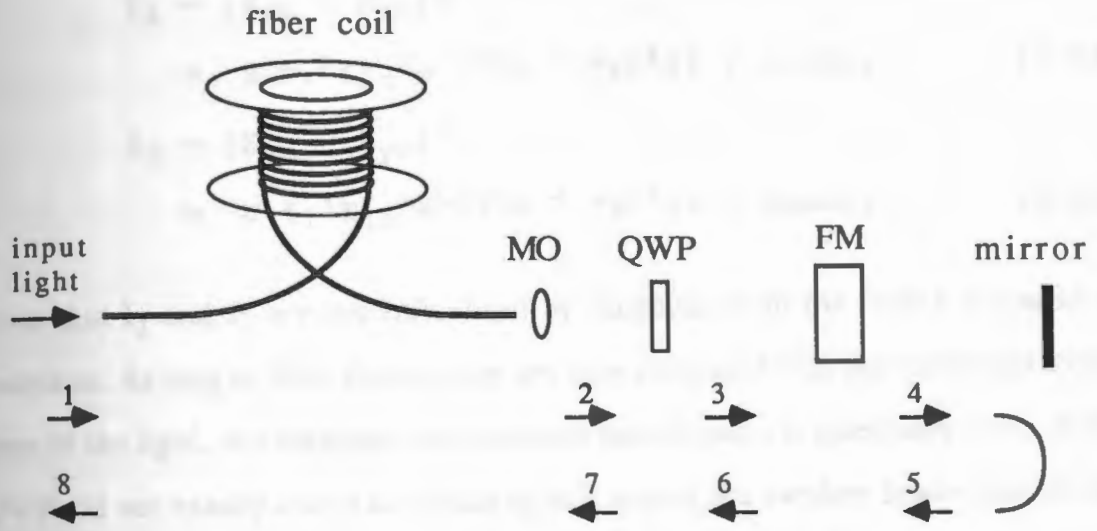

(a)

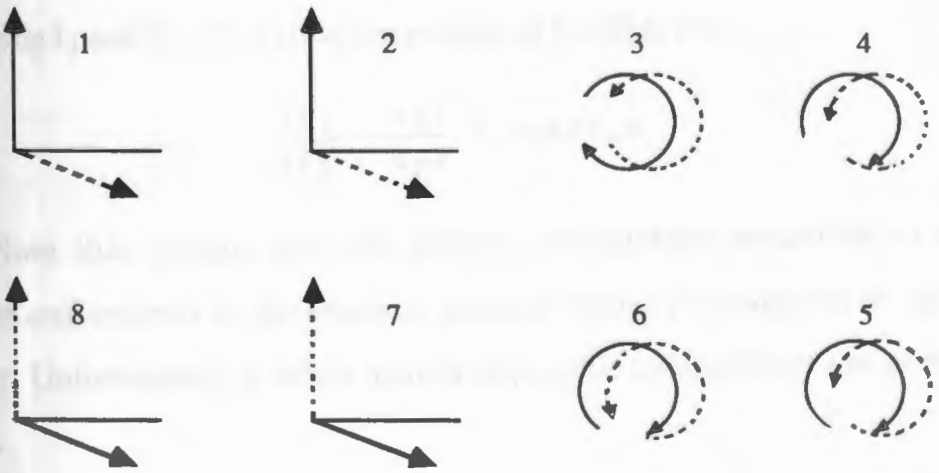

(b)

Fig. 5.2 Polarization-rotated reflection with Faraday effect sensor

$$I_1 = |E_{xo} + E_{yo}|^2$$

$$= 0.5\gamma^2 E_{in}^2 e^{-2(\alpha_x + \alpha_y)\ell}(1 + \cos 2\theta_F) \qquad (5.2a)$$

$$I_2 = |E_{xo} - E_{yo}|^2$$

$$= 0.5\gamma^2 E_{in}^2 e^{-2(\alpha_x + \alpha_y)\ell}(1 - \cos 2\theta_F) \qquad (5.2b)$$

Note that I_1 and I_2 are not influenced by fluctuations in the fiber's propagation constants. As long as these fluctuations are slow compared with the round trip transit time of the light, this idealized configuration cancels what is essentially noise. If the QWP did not exactly retard the phase by $\pi/2$, and/or the incident linear light on the fiber was not at exactly 45° to the polarization axes, then the fiber's fluctuating propagation constant would appear in (5.2), giving some variation in the output intensities I_1 and I_2.

Again, we can normalize out the effects of light intensity variations by substituting I_1 and I_2 of (5.2) into the relation of (4.22) to get

$$\frac{(I_1 - I_2)}{(I_1 + I_2)} = \cos 4VLB \qquad (5.3)$$

Note that another possible sensing configuration would be to put the polarizer *and* analyzer at the sensor to produce intensity modulation of light down the fiber. Unfortunately, it would then be impossible to implement this normalizing scheme.

5.2 Polarization-rotated reflection in a non-ideal sensor system

Enokihara, Masayuki, and Tadasi [43] used the configuration of Figure 5.2, but assumed for their analysis perfect optical components and perfectly equal input excitations on the fiber eigenmodes. Furthermore, the scheme was not examined for a time-varying magnetic field.

We will analyze the effectiveness of polarization-rotated reflection to cancel phase noise in Figure 5.2, considering the angle of incident linear polarization at the fiber input, θ_{in}, and the phase retardation of the QWP, ϕ. (The ideal case being $\theta_{in} = 45°$, and $\phi = 90°$.) The electric field outputs exiting the Wollaston prism can be found by multiplying the Jones matrices for each system component as shown in Figure 5.3.

Since QWP's can typically have tolerances as high as $\pm \lambda/25$ ($= 90° \pm 15°$), and because the proper alignment of the polarizing beamsplitter and QWP axes are not difficult (and therefore have small error tolerances), we will let $\theta_r = \theta_w = 45°$. Appendix 7 carries out the tedious matrix multiplication of Figure 5.3 to arrive at one intensity output of the Wollaston prism in Figure 5.2:

$$
\begin{aligned}
I_o = 0.5 I_{in} \gamma^2 \Big\{ & (\sin\theta_{in} - \cos\theta_{in}) \Big[(\sin\theta_{in} - \cos\theta_{in}) \cdot \\
& e^{-2(\alpha_x + \alpha_y)\ell} \sin^2\theta_F + e^{-(\alpha_x + \alpha_y)\ell} \sin 2\theta_F \cos\phi \cdot \\
& (\cos\theta_{in} e^{-2\alpha_x \ell} + \sin\theta_{in} e^{-2\alpha_y \ell}) \cos(\beta_x - \beta_y)\ell \Big] + \\
& \cos^2\theta_F \Big[\sin^2\phi (\cos\theta_{in} + \sin\theta_{in})^2 e^{-2(\alpha_x + \alpha_y)\ell} - \\
& (\cos\theta_{in} + \sin\theta_{in}) e^{-(\alpha_x + \alpha_y)\ell} \sin 2\phi \sin(\beta_x - \beta_y)\ell \cdot \\
& (\cos\theta_{in} e^{-2\alpha_x \ell} - \sin\theta_{in} e^{-2\alpha_y \ell}) + \cos^2\phi [\cos^2\theta_{in} e^{-4\alpha_x \ell} + \\
& \sin^2\theta_{in} e^{-4\alpha_y \ell} + \sin 2\theta_{in} e^{-2(\alpha_x + \alpha_y)\ell} \cos 2(\beta_x - \beta_y)\ell] \Big] \Big\}
\end{aligned}
\tag{5.4}
$$

In our ideal case where $\theta_{in} = 45°$ and $\phi = 90°$, the propagation constants did not appear--now they appear in three different forms, $\cos(\beta_x - \beta_y)\ell$, $\sin(\beta_x - \beta_y)\ell$, and $\cos 2(\beta_x - \beta_y)\ell$. Clearly, if the propagation constants fluctuate in time, so will I_o, thus giving uncertainties in the desired measurand θ_F that we ultimately aim to extract. In order to estimate the degree of variation in I_o due to these terms, we must treat the argument $(\beta_x - \beta_y)\ell$ as a random variable of some assumed distribution.

$$\cdot \begin{bmatrix} \cos\theta_r & \sin\theta_r \\ -\sin\theta_r & \cos\theta_r \end{bmatrix}_2 \begin{bmatrix} e^{-(\alpha_x + j\beta_x)\ell} & 0 \\ 0 & e^{-(\alpha_y + j\beta_y)\ell} \end{bmatrix}_1 \begin{bmatrix} E_x = E_{in}\cos\theta_{in} \\ E_y = E_{in}\sin\theta_{in} \end{bmatrix}$$

$$\cdot \begin{bmatrix} 1 & 0 \\ 0 & e^{-j\phi} \end{bmatrix}_6 \begin{bmatrix} -1 & 0 \\ 0 & -1 \end{bmatrix}_5 \begin{bmatrix} \cos\theta_F & \sin\theta_F \\ -\sin\theta_F & \cos\theta_F \end{bmatrix}_4 \begin{bmatrix} 1 & 0 \\ 0 & e^{-j\phi} \end{bmatrix}_3$$

$$\gamma \begin{bmatrix} \cos\theta_w & \sin\theta_w \\ -\sin\theta_w & \cos\theta_w \end{bmatrix}_9 \begin{bmatrix} e^{-(\alpha_x + j\beta_x)\ell} & 0 \\ 0 & e^{-(\alpha_y + j\beta_y)\ell} \end{bmatrix}_8 \begin{bmatrix} \cos\theta_r & -\sin\theta_r \\ \sin\theta_r & \cos\theta_r \end{bmatrix}_7$$

$$= \begin{bmatrix} E_{x'o} \\ E_{y'o} \end{bmatrix} = \text{E-field components of one Wollaston prism output beam}$$

Definitions:

$E_{x,y}$ = electric field component input to fiber axes
θ_r = angle of QWP axes to fiber axes
$\alpha_{x,y}$ = attenuation on fiber axes
$\beta_{x,y}$ = propagation constant on fiber axes
ℓ = length of fiber
ϕ = retardance of QWP
γ = total system losses
θ_w = angle of Wollaston prism to fiber axes
θ_F = total Faraday rotation in crystal*

(1) field components at fiber output end
(2) coordinates rotated to QWP axes
(3) field components after transversing QWP
(4) field components after Faraday rotation
(5) field components after mirror reflection
(6) components after transversing QWP again
(7) coordinates rotated back to fiber axes
(8) components after travelling back through fiber again
(9) components on Wollaston prism axes

*Since the direction of Faraday rotation is the same for either light propagation direction, we let θ_F be the total rotation after two passes through the crystal.

Figure 5.3 Jones matrices for sensor system

Before we do this, we will make the simplifying assumption that $\theta_{in} = 45°$. The justification for this is that the uncertainty or tolerance in the value of wave plate retardance is greater than the uncertainty in keeping θ_{in} close to 45°. Thus, we are essentially assuming in our model that the dominant system non-ideality is the QWP retardance. The QWP that we use in our experiment has a measured retardance of about 75° (see Appendix 6), so we know a priori that this assumption is probably good. Also, according to the manufacturer of the fiber we use, the difference between the attenuation coefficients α_x and α_y is negligible. Thus, letting $\theta_{in} = 45°$ and $\alpha_x = \alpha_y = \alpha$, equation (5.4) reduces to

$$I_o = \gamma^2 I_{in} e^{-4\alpha\ell} \cos^2\theta_F \left[\sin^2\phi + \cos^2\phi \cos^2(\beta_x - \beta_y)\ell\right] \qquad (5.5)$$

This is the output intensity of one exiting beam from the Wollaston prism in Figure 5.2. Since both output beams are exactly complimentary, we need only analyze one beam. We can see that for $\phi = 90°$, I_o agrees with equation (5.2a) for the ideal system.

By treating $(\beta_x - \beta_y)\ell$ as a random variable of some assumed distribution, we will be able to find the statistics of I_o for the case where $\phi \neq 90°$. Since we are ultimately interested in the system's signal-to-noise ratio in order to determine the minimum measureable θ_F and thus the magnetic field sensitivity, we will eventually treat the variations in I_o as a noise term to be combined and/or compared to the photodetector thermal and shot noise. Fortunately, recent papers focusing on polarization fluctuations in highly birefringent fibers report typical statistics for random variables such as $(\beta_x - \beta_y\ell)$ in fibers [45], [46]. This data was essentially gotten by choosing the proper statistics that matched theory to experiment using Monte Carlo computer simulation. By trying various distributions for $(\beta_x - \beta_y)\ell = \Delta\beta\ell$, the authors found the appropriate distribution to be gaussian. Based on this, we

assume that $(\beta_x - \beta_y)\ell$ in equation (5.5) is a gaussian distributed random variable with mean $\eta_{\Delta\beta\ell}$ and variance $\sigma_{\Delta\beta\ell}{}^2$. By transformation of the random variable $\Delta\beta\ell$, we shall find the statistics of I_o.

Rewriting equation (5.5) we have

$$I_o = I_{in}\gamma^2 e^{-4\alpha\ell}\cos^2\theta_F\left[\sin^2\phi + 0.5\cos^2\phi(1 + \cos 2\Delta\beta\ell)\right] \qquad (5.6)$$

Since it is expected that the fluctuating linear retardance $\Delta\beta\ell$ over time gives $<\cos 2\Delta\beta\ell> = 0$, $<\Delta\beta\ell> = \pm\pi/4$. The angle brackets $<>$ indicate an ensemble average; we assume the process $\Delta\beta\ell(t)$ is distribution-ergodic [47]. By making the following definitions and simplifying variable substitutions, we set-up the problem of determining the mean and variance of the random variable I_o in equation (5.6):

Let the random variable $(\beta_x - \beta_y)\ell = \Delta\beta\ell = X$

$<X> = \eta_x = \pm\pi/4$

$$f(x) = \frac{1}{\sigma_x\sqrt{2\pi}}\, e^{-(x - \eta_x)^2/2\sigma_x^2}$$

Let the random variable $I_o = Y$

$Y = g(X)$

$A = I_{in}\gamma^2 e^{-4\alpha\ell}\cos^2\theta_F\cos^2\phi$

$B = I_{in}\gamma^2 e^{-4\alpha\ell}\cos^2\theta_F\sin^2\phi$

$C = A/2 + B$

$I_o = Y = A\cos^2 X + B = A/2\cos 2X + C$

$<I_o> = C = \eta_y$

The variance of Y is expressed by

$$\sigma_y^2 = E\{y^2\} - \eta_y^2 \qquad (5.7)$$

where

$$E\{y^2\} = \int_{-\infty}^{\infty} y^2 f(y)\,dy \tag{5.8}$$

$$= \int_{-\infty}^{\infty} g(x)^2 f(x)\,dx$$

$$= \int_{-\infty}^{\infty} (A/2\cos 2x + C)^2 f_X(x)\,dx$$

$$= \frac{1}{\sigma_X\sqrt{2\pi}} \int_{-\infty}^{\infty} (A/2\cos 2x + C)^2 e^{-(x-\eta_X)^2/2\sigma_X^2}\,dx \tag{5.9}$$

Evaluating (5.9) in Appendix 8 and using relation (5.7), we arrive at the standard deviation of the random variable Y, which corresponds to the standard deviation of the intensity variation of I_O:

$$\sigma_y = I_{in}\gamma^2 e^{-4\alpha\ell}\cos^2\theta_F\left[\cos^4\phi(1 + e^{-8\sigma_x^2}\cos 4\eta_X) + (\tfrac{1}{4}\cos^4\phi + \tfrac{1}{4}\cos^2\phi\sin^2\phi)e^{-2\sigma_x^2}\cos 2\eta)\right]^{\frac{1}{2}} \tag{5.10}$$

For $\eta_X = \pm \pi/4$ (5.10) reduces to

$$\sigma_y = I_{in}\gamma^2 e^{-4\alpha\ell}\cos^2\theta_F\left[\cos^2\phi(1 - e^{-8\sigma_x^2})^{\frac{1}{2}}\right] \tag{5.11}$$

Note that for $\sigma_X = 0$ and/or $\phi = \pi/2$, $\sigma_y = 0$ as expected.

Using the standard deviation σ_y to indicate the degree of fluctuation of I_O due to a fluctuating differential linear retardance $\Delta\beta\ell$, we can define a signal-to-noise ratio as

$$SNR = \frac{\langle I_O\rangle}{\sigma_y} = \frac{(0.5\cos^2\phi + \sin^2\phi)}{\cos^2\phi(1 - e^{-8\sigma_x^2})^{\frac{1}{2}}}$$

$$= \frac{(0.5 + \tan^2\phi)}{(1 - e^{-8\sigma_x^2})^{\frac{1}{2}}} \tag{5.12}$$

Here the signal is the average intensity value and the noise is the undesirable deviation from this value. This relation assumes that the detector's noise is small compared to the fluctuating intensity noise.

Based on previously published data [45], [46], typical values of σ_x might be $0.1\%(2\pi)$ to $5\%(2\pi)$, depending on fiber type and environmental conditions on that fiber. As an example, the voltage signal-to-noise ratio for $\sigma_x = 2\%(2\pi)$ and $\phi = 80°$ using (5.12) would be ~275:1. Note that even for a large σ_x, the worse case SNR for $\phi = 80°$ is ~33:1.

5.3 Total SNR in fiber-linked sensor

Here we include shot and thermal noise of a PIN detector with the standard deviation of the intensity fluctuation found in the last section to arrive at a total sensor system signal-to-noise ratio. We define this voltage SNR as

$$SNR = \frac{V_{\Delta S}}{V_{th} + V_{sh} + V_\sigma} \qquad (5.13)$$

where

$V_{\Delta S}$ = change in detector output voltage due to Faraday rotation
$= \Delta I_o(\eta e/hf)R_L$

$V_{th} = (4\kappa T\Delta f R_L)^{\frac{1}{2}}$

$V_{sh} = [2e\Delta f(I_d + \langle I_o\rangle \eta e/hf)]^{\frac{1}{2}}R_L$

$\langle I_o\rangle = I_{in}\gamma^2 e^{-4\alpha l}\cos^2\theta_F(\frac{1}{2}\cos^2\phi + \sin^2\phi)$

$\Delta I_o = I_o(\theta_F=0) - I_o(\theta_F)$
$= I_{in}\gamma^2 e^{-4\alpha l}\sin^2\theta_F(\frac{1}{2}\cos^2\phi + \sin^2\phi)$

V_σ = noise voltage due to fluctuating I_o
$= \sigma_y(\eta e/hf)R_L$

I_{in} = input intensity to fiber

γ^2 = total system loss factor

As in section 4.4, we can calculate the minimum detectable rotation, θ_{Fmin}, for a given signal-to-noise ratio by solving for θ_F in (5.13). To simplify this

calculation we investigate the possibility of neglecting the dark current I_d. The validity of this assumption can be checked by estimating the system losses, assuming an input laser intensity of some minimum value, and finding for what I_{in} $(\eta e/hf)\Delta f I_{in} \blacktriangleright 2eI_d\Delta f$. It turns out that for $I_{in} \gtrsim 1$ mW, $\gamma^2 \lesssim 40$ dB, $I_d \simeq 2$ nA and a photodiode with $\eta \gtrsim 0.5$, I_d can be neglected.

Without I_d, (5.13) can be rearranged in the form of a quadratic in $\cos^2\theta_F$:

$$\cos^2\theta_F\Big\{I_{in}\gamma^2 e^{-4\alpha\ell}(\eta e/hf)\Big[\cos^2\phi(1 - e^{-8\sigma x^2})^{\frac{1}{2}}SNR + (\tfrac{1}{2}\cos^2\phi + \sin^2\phi)\Big]\Big\} + \cos\theta_F SNR\Big[(2e^2\eta\Delta f/hf)I_{in}\gamma^2 e^{-4\alpha\ell}\cdot(\tfrac{1}{2}\cos^2\phi + \sin^2\phi)\Big]^{\frac{1}{2}} + \Big[SNR(4\kappa T\Delta f/R_L) - (\eta e/hf)I_{in}\gamma^2 e^{-4\alpha\ell}\cdot(\tfrac{1}{2}\cos^2\phi + \sin^2\phi)\Big] = 0 \qquad (5.14)$$

If we neglect the shot noise in (5.13), then (5.14) reduces to the following closed form expression for small rotations:

$$\theta_{Fmin} = \qquad (5.15)$$

$$\sin^{-1}\left[\frac{SNR\Big[(4\kappa T\Delta f/R_L)^{\frac{1}{2}} + \eta e/hfI_{in}\gamma^2 e^{-4\alpha\ell}\cos^2\phi(1 - e^{-8\sigma x^2})^{\frac{1}{2}}\Big]}{I_{in}\gamma^2 e^{-4\sigma x\ell}(\tfrac{1}{2}\cos^2\phi + \sin^2\phi)\eta e/hf}\right]^{\frac{1}{2}}$$

Given the various parameters then, we can find θ_{Fmin}.

Also, since $Cd_{1-x}Mn_xTe$ has a fast response time, we may be interested in keeping R_L small in order to minimize the photodetectors RC time constant. Defining the detectors 3 dB roll-off frequency as $\Delta f = 1/2\pi R_L C_d$, where C_d is the photodetector's capacitance, we can solve for R_L and substitute into the thermal noise term to get $[8\pi\kappa T(\Delta f)^2 C_d]^{\frac{1}{2}}$. (Some caution should be used when doing this, however, since at small bandwidths this formula implies an R_L above what is realistically possible.)

As a typical example, say that in Figure 5.2 the Faraday material is 0.5 cm long, has a Verdet constant of $0.16° \text{ cm}^{-1} \text{G}^{-1}$, $\Delta f = 1$ KHz, SNR = 5, $I_{in}\gamma^2 = 10^{-5}$ W, and $\eta = 0.5$. Solving for the minimum measurable B-field for various values of σ_x and ϕ yields the plot in Figure 5.4. As additional examples, Figure 5.5 and 5.6 use the same parameters except Δf is 10 MHz and 100 MHz, respectively. As expected, the greatest sensitivity occurs when the $\Delta\beta\ell$ fluctuations are cancelled by using a perfect QWP ($\phi = \pi/2$).

In order to allow Figures 5.4-5.6 to apply to any material with some specified length L and Verdet constant V, we multiply the vertical scale values by V (of $Cd_{.5}Mn_{.5}Te$) x L = $(0.16°/\text{cm} \cdot \text{G})(0.5 \text{ cm}) = 0.08$. Thus, Given V and L of a newly proposed material we have:

B_{min} for the new Faraday material = $0.08 \cdot (B_{min}$ values in Figures$)/(V \cdot L)$.

It should be pointed out that the sensitivity could be greatly improved for high frequency fields over that shown in these plots by using a transimpedance amplifier after the photodiode to lower the effective load capacitance [48]. For comparison purposes we have assumed here that the PIN detector and load resistor sets the SNR.

5.5 Increasing the sensitivity

The sensitivities shown in the previous plots can be improved by placing another QWP just before the Wollaston prism in Figure 5.2 with the principle axes aligned with the principle axes of the fiber (x and y coordinates). The additional QWP biases the retardation $\Delta\phi = 2\theta_F$ by $\pi/2$, thus changing the cosine terms in (5.2) to sines. Since the sine function changes faster for small changes in θ_F than the cosine function, the sensitivity is improved. We check the degree of sensitivity improvement by appropriately changing the ΔI_0 term in the SNR relation of (5.13).

With sines in place of cosines in (5.2), the new ΔI_o term is

$$\Delta I_o = I_o(\theta_F=0) - I_o(\theta_F)$$

$$= I_{in}\gamma^2 e^{-4\alpha l}\sin 2\theta_F(\sin^2\phi + \tfrac{1}{3}\cos^2\phi) \qquad (5.16)$$

Using (5.15) in (5.13), the new SNR =

$$\frac{(\eta e/hf) I_{in}\gamma^2 e^{-4\alpha l}\sin 2\theta_F(\sin^2\phi + \tfrac{1}{3}\cos^2\phi)}{N + M + [(2e^2\eta/hf)\Delta f I_{in}\gamma^2 e^{-4\alpha l}(\tfrac{1}{3}\cos^2\phi + \sin^2\phi)(1 + \sin 2\theta_F)]^{\frac{1}{2}}}$$

where $N = (4\kappa T\Delta f/R_L)^{\frac{1}{2}}$

$M = \sigma_Y \eta e/hf$, where the $\cos^2\theta_F$ term is replaced by $1+\sin 2\theta_F$ in (5.11)

Since the noise in the denominator is virtually unchanged for small θ_F's compared to the SNR of (5.13), we can evaluate the improvement in SNR using the extra QWP by comparing the signal term in the numerator in (5.13) verses (5.16):

$$\text{Improvement factor in SNR} = \frac{\text{signal term in (5.16)}}{\text{signal term in (5.13)}}$$

$$= \frac{\sin 2\theta_F}{\sin^2\theta_F} \qquad (5.18)$$

Thus, for the measurement of small values of θ_F, we could theoretically acheive much improvement in the SNR using this method. For measurements of, say, $\theta_F \simeq 1°$, the improvement factor in SNR would be about 100 in terms of the minimum resolvable rotation. Neglecting shot noise in (5.17) and solving for the minimum measurable rotation gives

$$\Delta\theta_{Fmin} = \qquad (5.19)$$

$$\tfrac{1}{3}\sin^{-1}\left[\frac{SNR\left[(4\kappa T\Delta f/R_L)^{\frac{1}{2}} + \eta e/hf I_{in}\gamma^2 e^{-4\alpha l}\cos^2\phi(1 - e^{-8\sigma x^2})^{\frac{1}{2}}\right]}{I_{in}\gamma^2 e^{-4\alpha l}(\tfrac{1}{3}\cos^2\phi + \sin^2\phi)\eta e/hf}\right]$$

Note that the ratio of (5.15) to (5.19) can be expressed by

$$\text{angle resolution improvement} = \frac{(5.15)}{(5.19)} = \frac{\sin^{-1}K}{2\sin^{-1}K^{\frac{1}{2}}} \qquad (5.20)$$

where K is the argument of (5.19). In order to give a representative idea of sensitivity improvement, we consider the following example:

Parameters:		
	$\phi = 80°$	$I_{in}\gamma^2 = 10^{-7}$ W
	$R_L = 0.1$ M Ω	$\Delta f = 1$ KHz
	$\eta = 0.5$	SNR = 10
	$\sigma_x = 0.2\%(2\pi)$	$\lambda = 0.633\ \mu$m
	T = 300° K	$\alpha = 0$

Using the given parameters, $\Delta\theta_{Fmin} = 7.2°$ for (5.15) and 0.45° for (5.19), so the theoretical resolution is about 16 times better in this particular case. We were unable to set-up this more sensitive sensor configuration in our experiment, so the relation of (5.14) will eventually be used to relate theory to experiment.

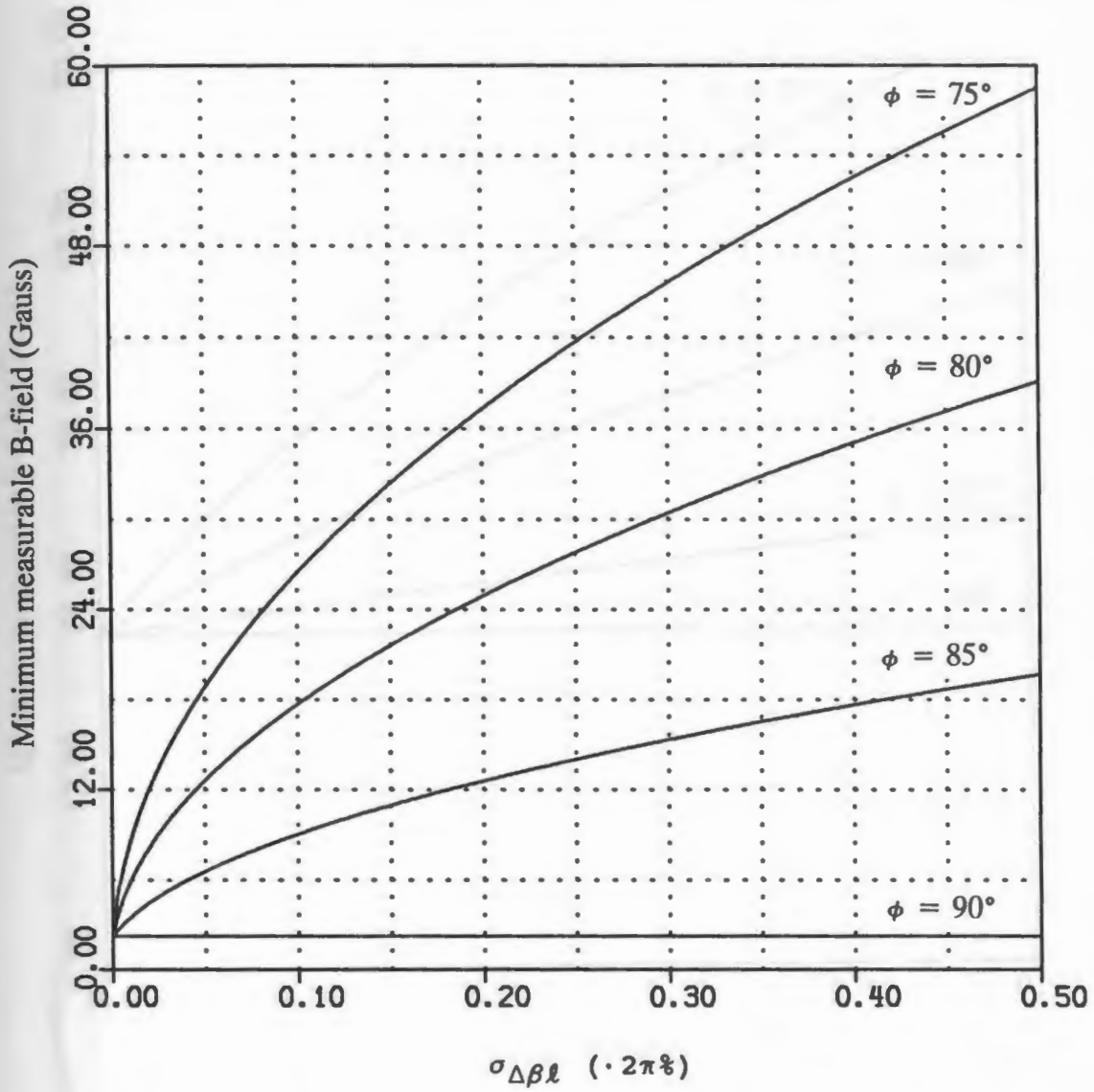

Fig. 5.4 Minimum measurable B-field for Δf = 1 KHz
SNR = 5, $I_{in} = 10^{-5}$ W, η = .5, sensor length = .5 cm

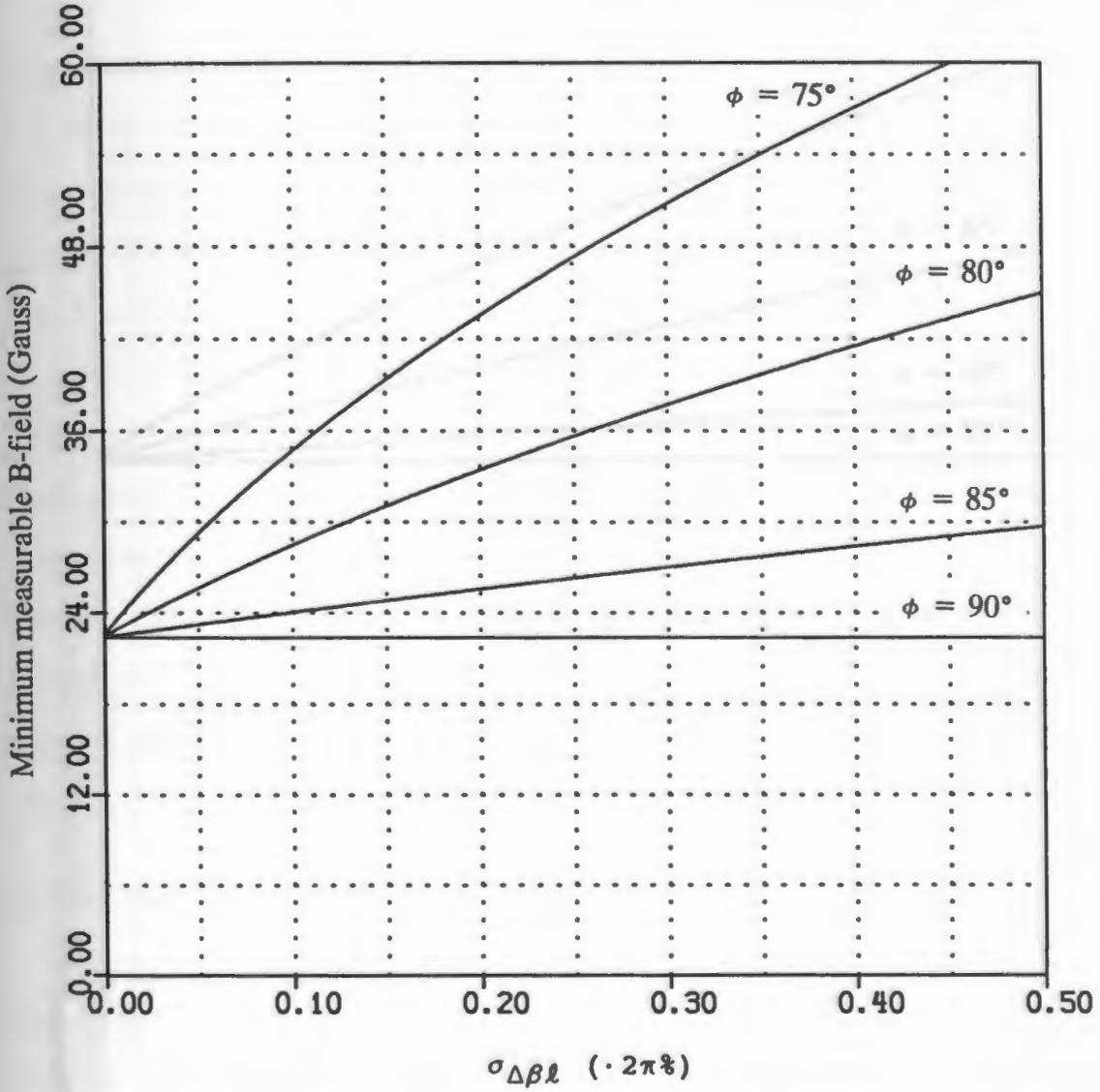

Fig. 5.5 Minimum measurable B-field for $\Delta f = 10$ MHz SNR = 5, $I_{in} = 10^{-5}$ W, $\eta = .5$, sensor length = .5 cm

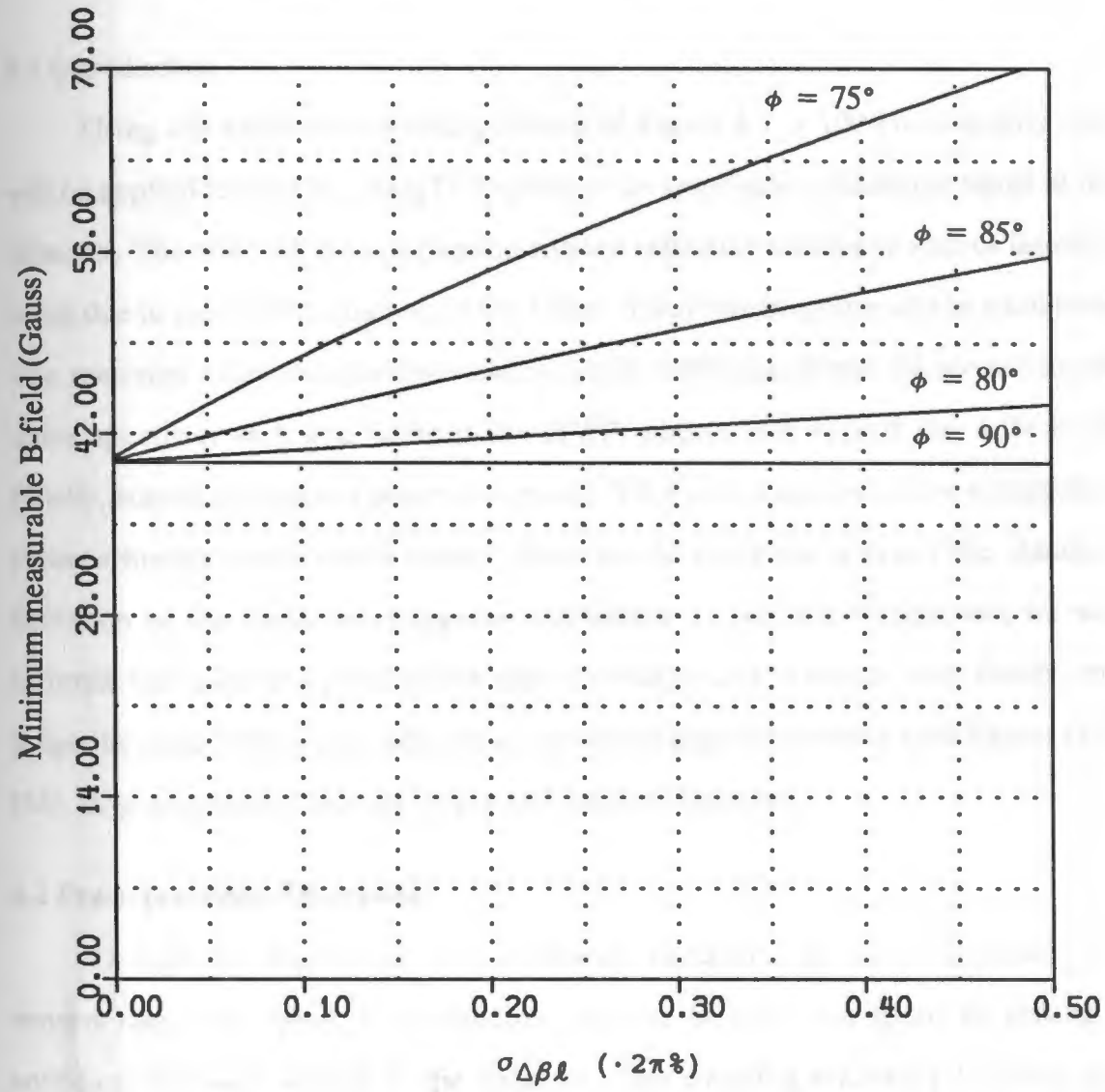

Fig. 5.6 Minimum measurable B-field for $\Delta f = 100$ MHz
SNR = 5, $I_{in} = 10^{-5}$ W, $\eta = .5$, sensor length = .5 cm

CHAPTER 6 ◊ FIBER-LINKED SENSOR--EXPERIMENT

6.1 Introduction

Using the experimental configuration of Figure 6.1, a 100 Hz magnetic field will be applied to the $Cd_{1-x}Mn_xTe$ to produce an amplitude modulation signal at the detector. The affect of the polarization-rotated reflection scheme to reduce intensity noise due to random fluctuations in the fiber's linear birefringence will be examined. The spectrum analyzer will allow viewing of this 100Hz signal and the accompanying noise spectrum with and without the QWP; photos will record the difference. Finally, empirical values of system losses and QWP retardance will allow comparison of experimental results with theory. Since we do not know a priori the standard deviation of the linear birefringence fluctuation σ_x for this comparison, we will estimate the value of σ_x that allows experimental results to concur with theory, and judge the credibility of this value based on recent papers reporting such figures [45], [46]. A photograph of this set-up can be found in Figure 6.6.

6.2 Pre-experiment--Discussion

Though the experiment was ultimately successful in reducing noise on a sensed magnetic signal, a tremendous amount of time was spent in getting a sufficient intensity output at the detector. The coupling efficiency between the microscope objective and the fiber was about 10% which, by itself, was not a problem. Indeed, without the crystal in the system, it was relatively easy to get a very visible intensity out of the Wollaston prism. Originally, the same crystal used in chapter 3 was put to test. Unfortunately, this 3.63 mm thick sample gave an

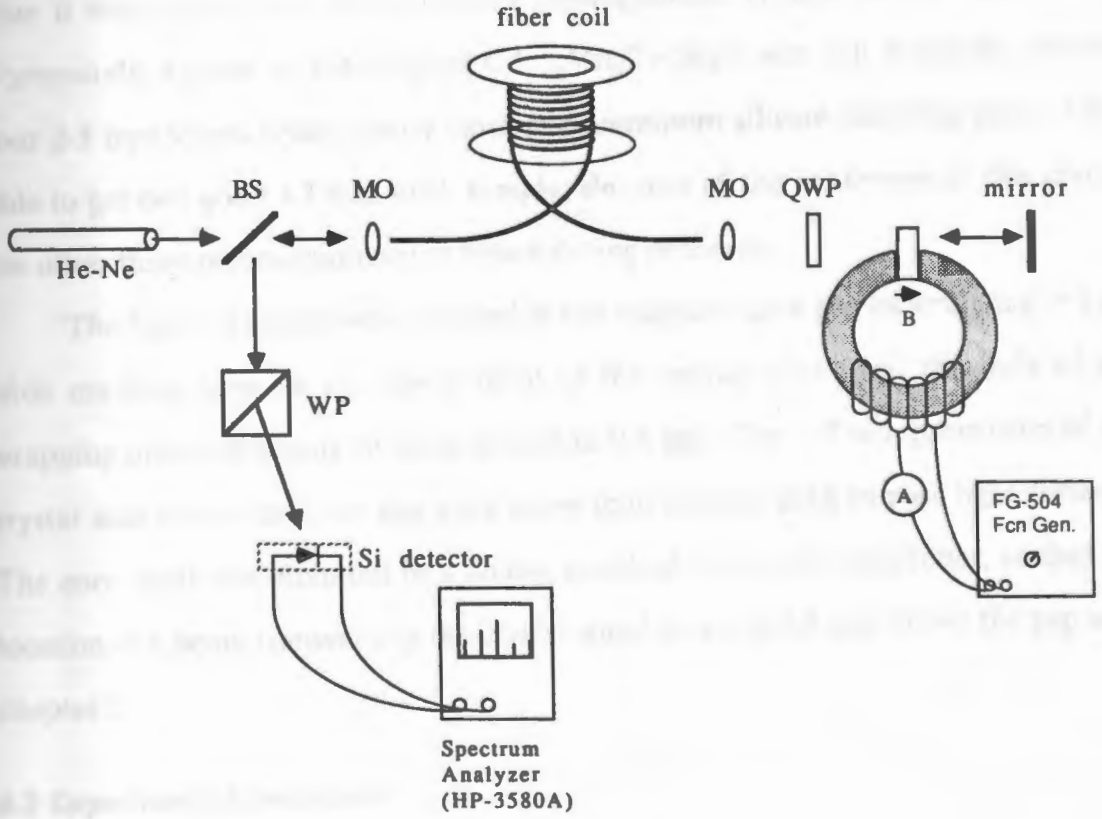

Fiber: 10 m of Andrew E-48280 polarization-maintaining
He-Ne: 4 mW polarized laser
BS: beamsplitter
QWP: quarter wave plate
MO: microscope objective; NA = .1
WP: Wollaston polarizing beamsplitter
A : ammeter

Figure 6.1 Fiber-linked magnetic sensor configuration

additional system loss of roughly 12 dB and, because of crystal defects, produced an irregular spot to be focused back onto the fiber's output end. Combinations of additional lenses and even concave mirrors were tried with no improvement. By this time it was clear that a thinner, more homogeneous crystal sample was needed. Fortunately, a piece of the original $Cd_{1-x}Mn_xTe$ ingot was still available, yielding four 2-3 mm slices. Using emory cloth and aluminum silicate polishing paste, I was able to get one good 1.3 mm thick sample. Because of the brittleness of this crystal, the other three pieces shattered or broke during polishing.

The finished crystal was centered in the magnetic core gap by wrapping ~1 cm wide masking tape on the lower third of the crystal slice until the bulk of the wrapping provided a snug fit when placed in the gap. The ~5 mm protrusion of the crystal slab above the core gap gave more than enough area to pass light through. The core itself was mounted in a holder attached to an x-y-z positioner, so that the location of a beam transversing the crystal could be set to 0.8 mm above the gap as in chapter 3.

6.3 Experimental procedure

(1) Turn on the He-Ne laser and let it warm up for at least thirty minutes.

(2) Find the fiber eigenaxes.

(3) Adjust the linear input polarization to 45° with respect to the fiber eigenaxes.

(4) Adjust the beamsplitter to 45°.

(5) Adjust the fiber coupler for maximum coupling.

(6) Adjust the marked QWP axes to 45° with respect to the fiber output axes.

(7) Without the crystal in the beam, adjust the mirror and microscope objective in order to maximize coupling back into the fiber.

(8) Adjust the x-y-z positioner to move the crystal into the beam, finding the clearest spot on the crystal directly above the core's gap.

(9) Readjust the microscope objective and mirror, as necessary, to achieve maximum coupling for the returning beam.

(10) Rotate the Wollaston prism to get two output intensity spots of identical intensity, and position the detector on one of these beams.

(11) Turn on the Tektronix FG-504 function generator to full output and tune to 100 Hz--check frequency on oscilloscope. Note the current reading on the ammeter.

(12) Connect the oscilloscope to the detector and verify that there is a 100 Hz modulation.

(13) Note the signal-to-noise difference on the scope with and without the QWP in the system.

(14) Put the QWP back in with the proper orientation and fine-tune its rotation angle to achieve minimum noise on the 100 Hz signal.

(15) Connect the detector to the spectrum analyzer and note the reproducibility of the spectrum trace. Store the trace.

(16) Photograph the stored trace.

(17) Remove the QWP and again photograph the resulting frequency spectrum.

(18) Repeat 13-16 for various environmental stresses on the fiber coil, such as temperature change, blowing air, etc.

(19) Measure the distance from the beam's center in the crystal to the top of the gap, using the micro-adjusters on the x-y-z positioner.

(20) Measure the intensity of one Wollaston prism output beam with the UDT intensity meter.

6.4 Procedure discussion

The eigenaxis of the fiber can be found by coupling light in one end and observing the far field pattern from the output end. Because the fiber core is elliptical, the minor axis of the core cross section corresponds to the major axis of the far field pattern and vice versa. The small clamp at the end of the fiber is rotated until the far field ellipse has its major axis upright. Doing this for both fiber ends

gives an alignment that is accurate to about ± 5°. This alignment can be improved using the fact that if only one polarization axis of the fiber is excited, the output polarization will be linear. (It is possible that the total linear birefringence of the fiber is such that linear output light is observed even if both input eigenaxes are exited. In this case however, small ambient temperature changes readily change the birefringence which consequently changes the output polarization from linear to elliptical--this is easily observed.) Thus, we can more precisely find one of the eigenaxes, especially since we already know approximately where it is based on the far field observations. The input polarization then is rotated 45° from the fiber eigenaxes in order to equally exite both eigenmodes. The remaining procedural steps are fairly straight forward.

6.5 Experimental results

As expected, the 100 Hz magnetic field modulated the light on the detector to produce a 100 Hz sinusoid on the oscilloscope. However, low frequency variations ($\lesssim$ 5 Hz) in detected intensity made it impossible to view a stationary waveform with the scope DC coupled to the detector. Using AC coupling, higher frequency noise could be seen riding on the 100 Hz sinusoid which varied in severity depending on the environmental conditions. An air conditioner on the ceiling above the optical table provided two environmental states: air condition on and air condition off (ambient). With the air conditioner on, air blew down on the table with enough force to sway the fiber entering the holders back and forth. This caused the most severe intensity noise, and provided the best test conditions for the noise cancellation scheme. (The fiber holder/postioner was firmly mounted on the table and did not move; the prepared fiber end was flush with tip of the holder so it too would not move.) A hair dryer pointed toward the fiber coil was also tried, but it actually produced less air

velocity than the air conditioner.

With the detector still input to the oscilloscope, the QWP could be rotated to minimize the noise on the sinusoid. In fact, it was found that the difference in the rotational position of the QWP between maximum noise and minimum noise was 45° --exactly as expected. When the QWP was rotated until maximum noise was observed, its principle axes were aligned with the principle axes of the fiber; removing the QWP had no noticable effect on the signal.

Since it was difficult to quantify this noise suppression by simply viewing the signal on the oscilloscope, an HP-3580A low frequency spectrum analyzer was used to get a more accurate estimate of the signal-to-noise ratio for eventual comparison with theory. With the air conditioner on, spectrum photos were taken with and without the QWP in the system. These photos are displayed in Figure 6.2. The center peak is the 100 Hz modulated light on a 20 Hz/division scale; the vertical scale is 1 mv/division (10 divisions shown). Note the dramatic reduction in noise with the QWP. A couple sweeps of the spectrum analyzer yielded consistently similar spectrums for both photos. Because the division markings were not illuminated on the spectrum analyzer, and because Figure 6.2 represents our best photos, we had a photographic lab superimpose a separate image of the graticules onto the spectrum photo image to produce these prints.

At a later time, we tilted the $Cd_{1-x}Mn_xTe$ crystal slab $\sim 15°$ in order to increase the modulation depth, then secured a blowing hair dryer about 1 foot from the fiber coil while the room air conditioner was off. We photographed the spectrum again with and without the QWP, as shown in Figure 6.3. This time there was not much noise to begin with, but an improvement is still obvious. It is suspected that the heating effect of the hair dryer would primarily cause slow changes in the fiber's linear birefingence, which would be masked by the other low frequency

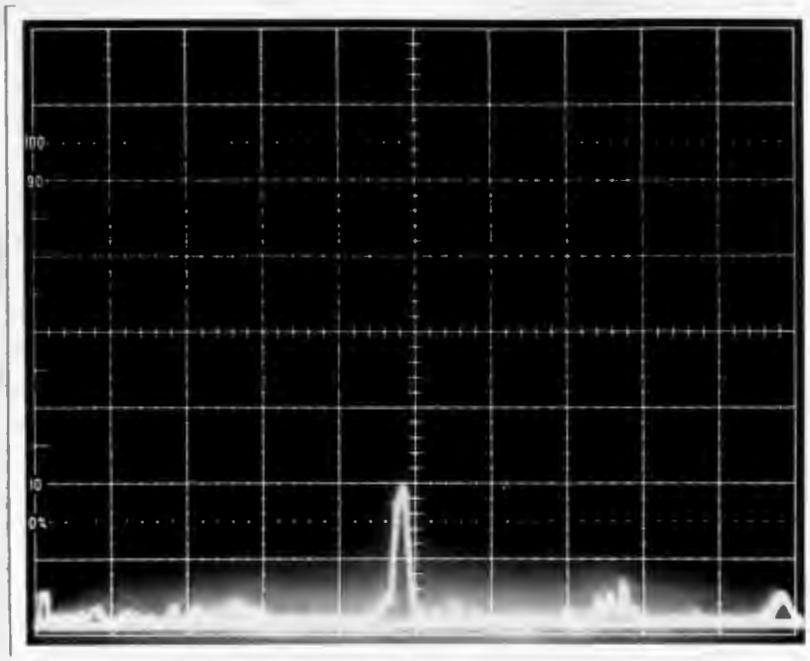

(a) With noise cancellation scheme ($\phi = 75°$)

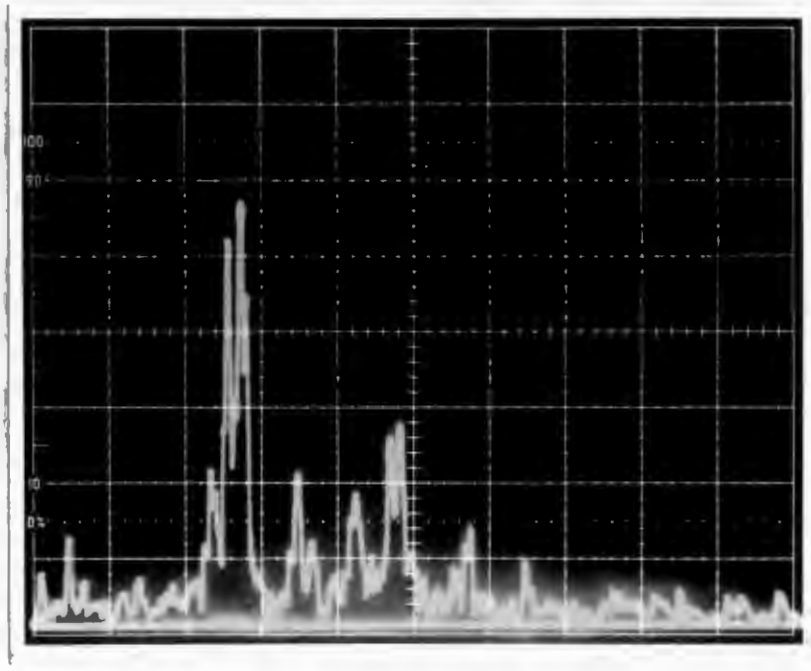

(b) Without noise cancellation scheme ($\phi = 0°$)

Fig. 6.2 Signal and noise spectrum of fiber-linked magnetic sensor; environmental conditions: air conditioner on. Spectrum analyzer settings: 1 mv/div, 20 Hz/div, 3 Hz resolution.

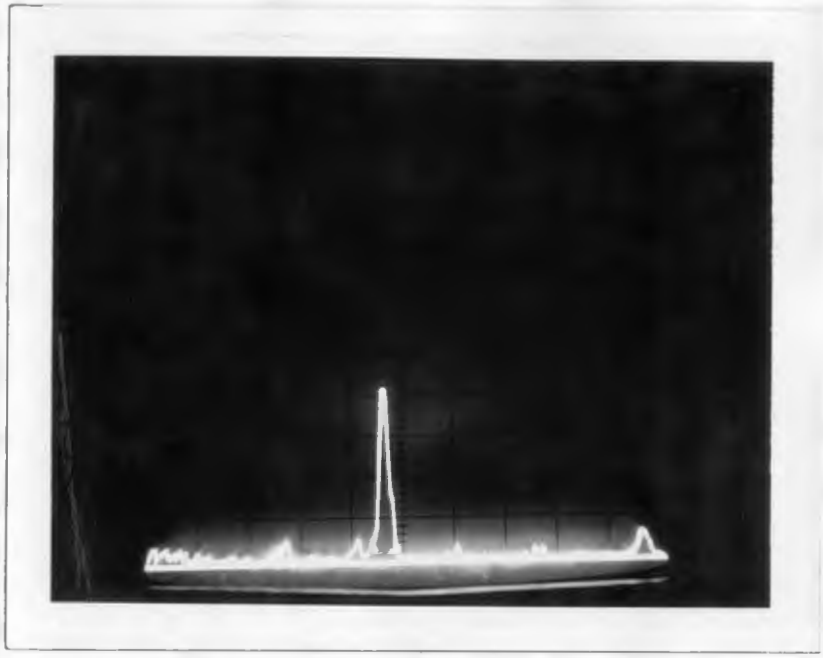

(a) With noise cancellation scheme ($\phi = 75°$)

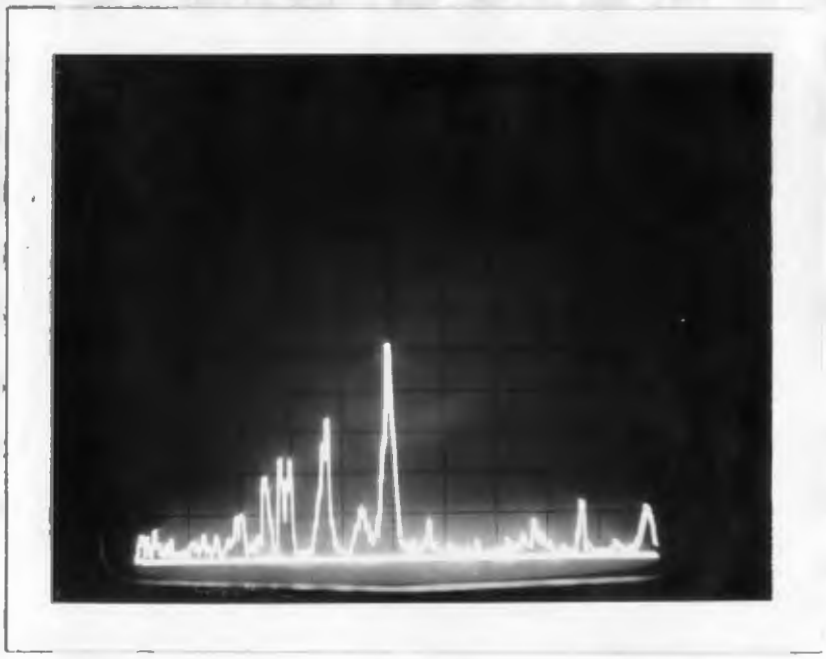

(b) Without noise cancellation scheme ($\phi = 0°$)

Fig. 6.3 Signal and noise spectrum of fiber-linked magnetic sensor; environmental conditions: air conditioner off, warm air from hair dryer. Spectrum analyzer settings: 2 mv/div, 20 Hz/div, 3 Hz resolution.

variations that occurred under ambient conditions.

In order to achieve 3 Hz resolution on the spectrum analyzer for these photos, a slow sweep speed was used, requiring roughly a minute to complete a trace. For this reason, we were especially still during the spectrum recordings to minimize any movement of the fiber by other than the air conditioner.

6.6 Experimental results versus theory

Before we can use equation (5.13) and (5.14) to arrive at theoretical plots to compare with experiment, a few experimental parameters need to be given. First, the light reflected back through the system and incident on the photodetector during the experiment (corresponding to Figure 6.2) was approximately 5 x 10^{-8} Watts, which represents $I_{in}\gamma^2$. The spectrum analyzer had an input impedance of R_L = 1 MΩ, and its effective bandwidth setting was 3.45 Hz. The QWP was measured to have a retardance of 75°, and the coil current was 92 mA. Finally, from the spectrum photos, we can estimate the signal-to-noise ratios and use these figures to find the cooresponding standard deviation of linear birefringence fluctuations which match theory to experiment.

Figures 6.4 and 6.5 are the theoretical plots of σ_x verses θ_{Fmin} using the aforementioned parameters for the cases where ϕ = 75° and ϕ = 0° (no QWP), respectively. Figure 6.4 covers signal-to-noise ratios from 1-10, and Figure 6.5 covers signal-to-noise ratios from 0.2-2. The magnetic field generated in these experiments at the point where the beam transversed the crystal was 182 Gauss. For the case where the crystal was not tilted (Figure 6.2), this gives a polarization rotation of

$$\theta_F = VBL = (0.15°cm^{-1}G^{-1})(182\ G)(0.13\ cm)(2) = 7.1°$$

The spectrum photo in Figure 6.2a shows a signal-to-noise ratio of about 10:1. On

the theoretical plot of Figure 6.4, a SNR of 10:1 and θF_{min} of 7.1° corresponds to a σ_x of about 0.12%(2π). For the case where the QWP was taken out of the system ($\phi = 0$), the spectrum photo shows a SNR that is a little over 0.4, which corresponds to $\sigma_x \simeq 0.1\%(2\pi)$ on Figure 6.5. The fact that σ_x is nearly the same for the case with and without the QWP is encouraging. Assuming $\sigma_x \simeq 0.12\%(2\pi)$, our theory seems to correctly estimate what the SNR should be for two values of retardance, $\phi = 0°$ and $\phi = 75°$.

Ideally of course, it would have been nice to have a continuous experimental plot to compare with the theoretical curves. For example, if we had used a variable retarder in our set-up in place of the QWP, we could have empirically plotted the retardance ϕ versus SNR over the entire range of $\phi = 0°$ to $\phi = 90°$, instead of just $\phi = 0°$ and $\phi = 75°$. This would have been a more rigorous test of theory. Unfortunately, a variable retarder was not available. For future experiments without a variable retarder, one might include the orientation of the QWP as a variable in the theoretical model and experimentally plot this orientation in degrees versus the SNR for a given Faraday rotation. One could then see if a consistant value of σ_x satifies this curve. Also, if our signal was stronger, we could have plotted θ_{Fmin} versus SNR.

The next question is whether or not the value of σ_x that matched theory to experiment is a reasonable one. From various papers dealing with linear birefringence fluctuations and polarization noise, the answer seems to be yes. In one paper, 48 meters of elliptical-type polarization preserving fiber was coiled and attached to a loadspeaker driven at 27 Hz in order to induce fluctuating propagation characteristics [45]. In this case, values of σ_x ($= \sigma_{\Delta\beta\ell}$) were found to be around 1.6%(2π). Considering that we were using only 10 meters of fiber with far less environmental stress, $\sigma_x \simeq 0.12\%(2\pi)$ seems quite plausible. Another paper

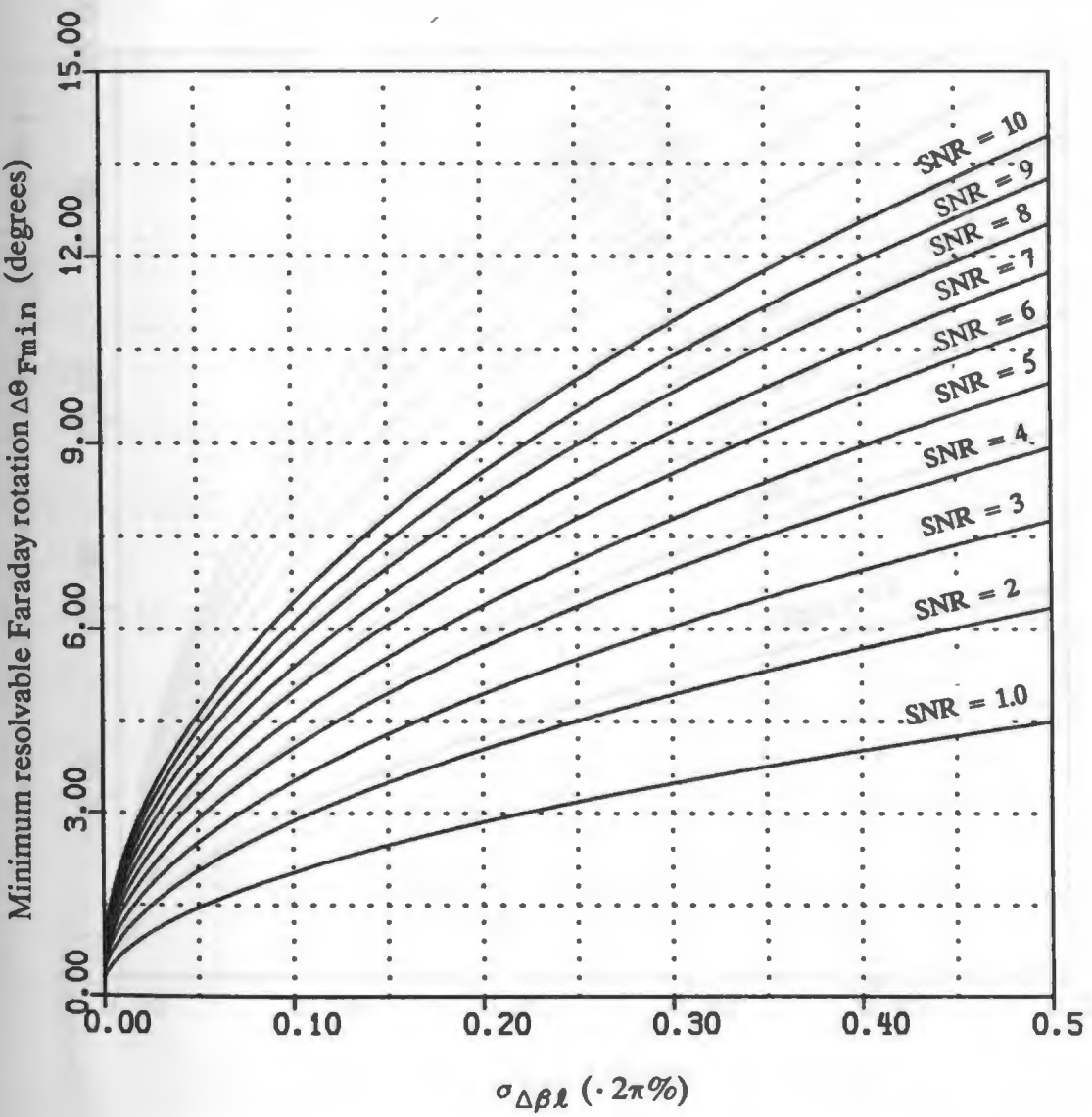

Fig. 6.4 Theoretical $\Delta\Theta_{min}$ vs. $\sigma_{\Delta\beta\ell}$ for experimental conditions corresponding to Fig. 6.2a ($\phi = 75°$).

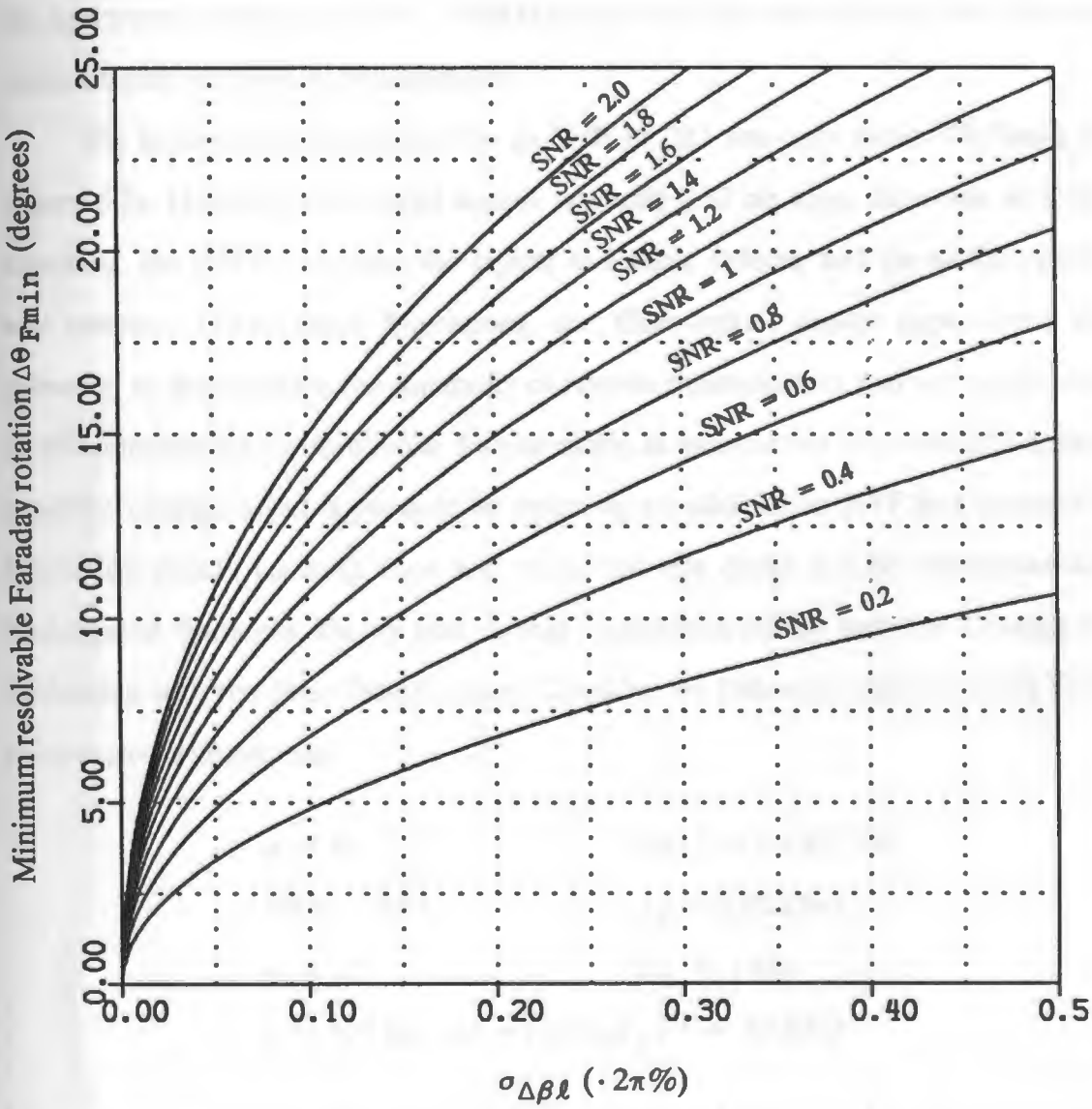

Fig. 6.5 Theoretical $\Delta\Theta_{min}$ vs. $\sigma_{\Delta\beta\ell}$ for experimental conditions corresponding to Fig. 6.2b ($\phi = 0°$).

examined the spectrum of the state of polarization fluctuations out of a single mode fiber by performing a Fourier transform of time domain samples of the polarization noise [49]. The fiber used in their experiment exhibited an exponential function of the kind $F(\nu) = ae^{-b\nu}$, where $b \simeq 0.6 \times 10^{-3}$ Hz^{-1}. From this we can show that half the spectrum's power was below ~600 Hz. From our spectrum photos, the noise was indeed higher at the lower frequencies.

The sensitivity of our set-up for an SNR of 10:1 was only about 180 Gauss for Figure 6.2a. However, our crystal sample was only 0.13 cm long, there was no index matching, the QWP was poor, the crystal had some defects, and the surface polish was uneven. Given these limitations, our fiber-linked sensor experiment was primarily to demonstrate the capability of remote measurement and the suppression of environmentally induced noise. Furthermore, as pointed out in section 5.5, a more sensitive configuration is possible by inserting an additional QWP just before the Wollaston prism. Lacking time and resources this could not be experimentally investigated. However, theory tells us that sensitivities on the order of 1 Gauss are achievable with the fiber-linked sensor. Consider the following example using fairly conservative parameters:

$\phi = 85°$	$I_{in\gamma}^2 = 5 \times 10^{-7}$ W
SNR = 10:1	$\sigma_x = 0.2\%(2\pi)$
$\eta = 0.5$	$R_L = 1\ M\Omega$
$\lambda = 633$ nm	$\Delta f = (2\pi C_d R_L)^{-1} = 32$ KHz

Using equation (5.19), $\theta_{Fmin} = 0.13°$. For a 0.5 cm long $Cd_{1-x}Mn_xTe$ crystal with $V = 0.15° \text{ cm}^{-1} \text{ G}^{-1}$, this corresponds to a sensitvity of about 0.9 Gauss. Futhermore, for measurements of high frequency fields, a transimpedance amplifier following the detector would likely be used to reduce the effective load capacitance so that a

higher load resistance could be tolerated [48]; the potential magnetic field sensitivity would thus be futher increased.

Summary

Despite a number of unforeseen obstacles--not the least of which was making a suitable crystal sample--the experiment successfully demonstrated a method of suppressing environmentally induced noise for a fiber-linked magneto-optical sensor. By treating the fiber's linear birefringence fluctuations as a stochastic process, we were able to obtain a theoretical model which concurred reasonably with experiment for an assumed variance of the birefringence fluctuations.

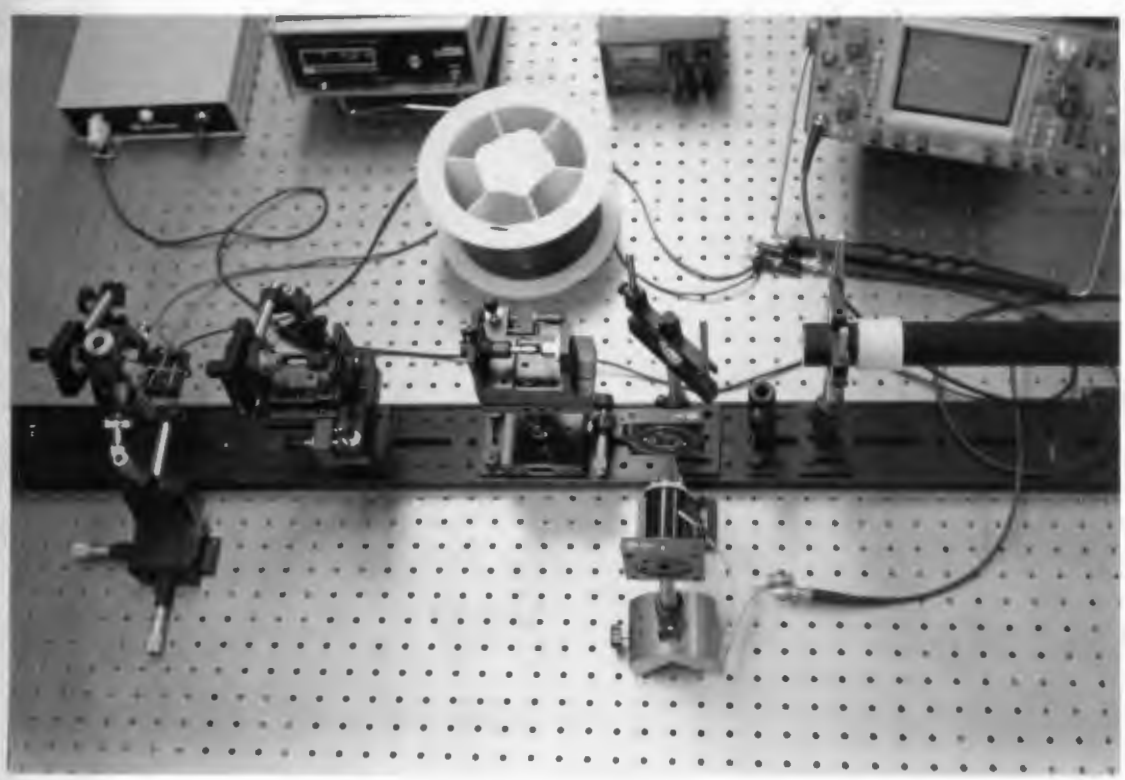

Fig. 6.6 Photograph of fiber-linked magnetic sensor experiment

CHAPTER 7 ◊ MAGNETO-OPTIC SENSORS--SUMMARY

7.1 Applications

Most of the papers dealing with magneto-optical sensing have focused on current measurement, particularly in the power industry. Though a small magnetic sensor, such as the one configured in this thesis, could be used to measure current in wires or "buses", the calibration would depend critically on sensor placement, since the magnetic field is inversely proportional to the radial distance **r** from the current carrying conductor. For this reason, optical fibers which enclose the conductor--thus eliminating the **r** dependence--are usually preferred (see equation (4.2)). However, using optical fibers is not the only way to enclose the current; authors at Maxwell Laboratories proposed an "absolute" current probe using sections of flint glass that would encircle a conductor. One advantage seen was the possibility of designing an absolute instrument because calibration will depend only on the Verdet constant of the rotative medium [40]. Such a configuration could also be used with $Cd_{1-x}Mn_xTe$. Using equation (2.2) with $V = 0.15° \, cm^{-1} G^{-1}$, and assuming a minimum resolvable $\Delta\theta$ of 0.01°, we can find the minimum resolvable current:

$$V\mu_o = (0.15° cm^{-1} G^{-1})(1cm/0.01m)(10^4 \text{ Gauss/Tesla})\mu_o$$

$$= 0.19° Amp^{-1} Turn^{-1}$$

For one turn (N = 1),

$$I_{min} = \theta_{Fmin}/(V\mu_o) = 0.01°/0.19° \, Amp^{-1} = 0.053 \text{ Amps.}$$

Futhermore, with a small sensor enclosure (e.g., $\lesssim$ 5 cm optical path length), the frequency response would be from DC to ~1 GHz, limited by optical transit time. Also, unlike conventional current probes, this one would produce no insertion impedance into the conductor under test, and would not readily saturate like typical ferrite cores used in conventional transformers. From discussions with engineers at the Boeing Development Center's Lightning Laboratory, their problems with conventional current probes for high pulsed currents are low risetime capability ($\lesssim$ 1 μs) and a limited Amp·second product (related to power handling capability and saturation effects) [50]. These limitations were also given by a scientist at Maxwell Labs [51]. Though $Cd_{1-x}Mn_xTe$ is far more sensitive than is necessary for measurements of thousands of amperes, some of the diamagnetic materials listed in Table 2.1 would be suitable. Finally, in the harsh electromagnetic environment of a Lightning Lab or similar facility, metallic links from instrumentation to current probe or magnetic sensor are subject to significant electromagnetic interference; optical systems, however, would be largely immune to EMI.

Additionally, note that for high frequency fields, even small loops of wire can pick-up significant voltages. Thus, even a conventional (non-optical) sensor that is linked to instrumentation using fiber optics is subject to errors caused by EMI. To illustrate, suppose we have a Hall device sensor that is coupled to an optical modulator and optically linked to instrumentation. If a mere 5 mm square "loop" of exiting Hall device wires is not adequately shielded, then a 10 MHz magnetic "noise" field of only 100 Gauss will produce an unwanted voltage of

$$V = \int \frac{\partial \mathbf{B}}{\partial t} \cdot d\mathbf{S} = 2\pi f(\text{Area})B \simeq 16 \text{ volts!}$$

Note that such a hypothetical sensor would be producing a Hall voltage that is much smaller than the above calculated value. The best Hall effect devices available usually do not exceed sensitivities of 100 μV mA^{-1} Gauss^{-1} [52]. For this sensitivity, a Hall bias current of 1 mA and an applied magnetic field of 100 Gauss would produce a Hall voltage of

$$V_{Hall} = (100\,\mu V\,mA^{-1}\,Gauss^{-1})(1\,mA)(100\,Gauss) = 0.01\,volts$$

The first proposed application for $Cd_{1-x}Mn_xTe$ was magnetic field measurement in particle accelerators at Sandia National Labs [29]. Another possible application is the measurement of RF fields around TV and FM antenna towers. From discussions with engineers at a consulting firm in Seattle, Washington [53], that makes these types of measurements, one problem they encounter is separating the effects of electric and magnetic fields when only one must be measured; a magnetometer may give false readings due to electric field coupling, for example. To get an idea of the magnitudes of the magnetic fields that must be measured, we consider the American National Standards Institute (ANSI) guidelines for the maximum recommended magnetic field exposure for very high frequency fields [54]. For 30 - 300 MHz, the magnetic field limit is $0.025(900/f^2)$ A^2/m^2 , where f is the frequency in MHz in this range. For 100 MHz in free space, this translates into a field of about 0.5 mGauss. Using equation (2.2), the corresponding amount of polarization rotation in a 4 cm length of Faraday material with V = 0.15° cm^{-1} G^{-1} is about 3 x 10^{-4}°. From discussions in chapter 4, this required sensitivity at such large bandwidths is probably not achievable--at least not without considerable sensor complexity. However, for other frequency ranges in the ANSI Radio Frequency Protection Guide, the field limitations are higher. For 0.3 - 3 MHz, the limit is 2.5 A^2/m^2, which translates into a free space magnetic field of 0.02 Gauss. Using the

previous example parameters, this corresponds to a Faraday rotation of 0.012°, which is detectable. Also, since $Cd_{1-x}Mn_xTe$ has an inherent frequency response into the GHz, it may find applications in measuring magnetic fields in microwave communications.

Finally, monitoring magnetic fields is not the only application for materials with large magneto-optic constants like $Cd_{1-x}Mn_xTe$. Optical isolators, bistable polarization devices [55], and magneto-optical modulators can also be built with many advantages using such materials.

7.2 Future research

Since a primary advantage of Faraday effect magneto-optic sensors such as the one proposed in this thesis is high frequency response, it would be instructive to test a sensitive Faraday material like $Cd_{1-x}Mn_xTe$ in a high frequency magnetic field; experimentally determined values of minimum measurable B-fields versus signal-to-noise ratios could then be compared directly with the theory in chapter 4 (e.g., equation 4.13).

In the fiber-linked magnetic sensor, it would be desirable to use a more reproducible method of inducing fiber birefringence fluctuations; a coiled fiber attached to a driven loadspeaker appears to be a good method [45].

Also, by using a number of different waveplates of various retardances in place of the quarter-wave plate in Figure 6.1, an experimental plot of the retardance ϕ versus the signal-to-noise ratio could be compared directly with the corresponding theoretical plot.

Finally, the experiment could be repeated using an extra quarter-wave plate at the output of the Wollaston prism to increase the sensing sensitivity, as described in section 5.4.

LIST OF REFERENCES

[1] T. G. Giallorenzi, J. A. Bucaro, A. Dandridge, G. H. Sigel, Jr., J. H. Cole, S. C. Rashleigh, and R. G. Priest, "Optical fiber sensor technology," J. Quantum Electron., vol. QE-18, pp. 626-661, April 1982.

[2] T. G. Giallorenzi, J. A. Bucaro, A. Dandridge, and J. H. Cole, "Optical-fiber sensors challenge the competition," IEEE Spectrum, vol. 23, pp. 44-49, Sept. 1986.

[3] R. S. Jamieson, R. P. Depaula, and E. L. Moore, "Overview of fiber-optical sensors," Jet Propulsion Lab. Report NPO-16817/6329, pp. 1-14, Aug. 1987.

[4] C. Ovrén, M. Adolfsson, B. Hök, and T. Brogårdh, "New oportunities with fibre-optic measurement," Sensor Review, pp. 199-205, Oct. 1985.

[5] S. McClelland, "Stimulating new developments into applications," Sensor Review, pp. 148-149, July 1986.

[6] J. H. Cole, T. G. Giallorenzi, and J. A. Bucaro, "Advances in optical fiber sensors," SPIE Integrated Optics, vol. 269, pp. 115-119, 1981.

[7] J. Fluitman and T. Popma, "Optical waveguide sensors," Sensors and Actuators, vol. 10, pp. 25-46, 1986.

[8] C. M. Davis, "Fiber optic sensors: an overview," SPIE Fiber Optic and Laser Sensors II, vol. 478, pp. 12-15, 1984.

[9] S. K. Krawczyk, "Senso-opto-micro-electronic (SOMET) devices," Sensors and Actuators, vol. 11, pp. 289-297, 1987.

[10] Marie-Helene du Chastel, "Fiberoptic sensors begin moving from laboratory to marketplace," Laser Focus, pp. 110-117, May 1987.

[11] J. Zilber, "Fiberoptic sensor market development," Kessler Marketing Intelligence, 1984.

[12] A. D. Kersey, D. A. Jackson, and M. Corke, "Single-mode fibre-optic magnetometer with dc bias field stabilization," J. Lightwave Tech., vol. LT-3, Aug. 1985.

[13] A. J. Rogers, "Optical measurements of power-system quantities," Electronics & Power, Feb. 1986.

[14] A. M. Smith, "Optical fibres for current measurements applications," Optics and Laser Tech., pp. 25-29, Feb. 1980.

[15] A. Papp and H. Harms, "Magnetooptical current transformer. 1: Principles," Appl. Optics, vol. 19, pp. 3729-3734, Nov. 1980.

[16] H. Aulich, W. Beck, N. Douklias, H. Harms, A. Papp, and H. Schneider, "Magnetooptical current transformer. 2: Components, Appl. Optics, vol. 19, pp. 3735-3740, Nov. 1980.

[17] H. Harms and A. Papp, "Magnetooptical current transformer. 3: Measurements," Appl. Optics, vol. 19, pp. 3741-3745, Nov. 1980.

[18] R. Malewski, "High-voltage current transformers with optical signal transmission," Optical Engineering, vol. 20, pp. 54-57, Jan.-Feb. 1981.

[19] K. Kyuma, S. Tai, M. Nunoshita, T. Takioka, and Y. Ida, "Fiber optic measuring system for electric current by using a magnetooptic sensor," Trans. Microwave Th. & Techniques, vol. MTT-30, pp. 1607-1611, Oct. 1982.

[20] B. D. Russell, "Switching transients in power substations present measurement challenges," EMC Tech., pp. 21-24, Jan.-Feb. 1986.

[21] J. Bronowski, *Science and Human Values*. New York: Harper & Row, 1965, p.13.

[22] Michael Faraday, "Experimental Researches in Electricity--Nineteenth Series," Philosophical Transactions, ed. B. Quaritch 1855, pp. 1-26, quoted in W. Swindell, ed., *Polarized Light*, Stroudsburg, Penn.: Halsted Press, 1975, pp. 104-105.

[23] D. Clarke and J. F. Grainger, *Polarized Light and Optical Measurement*, Braunschweig: Pergamon Press, 1971, ch. 2.

[24] E. Hecht and A. Zajac, *Optics*. Reading, Mass.: Addison-Wesley, 1979, ch. 8.

[25] K. Kyuma, S. Tai, M. Nunoshita, T. Takioka, and Y. Ida, "Fiber-optic current and voltage sensors using a $Bi_{12}GeO_{20}$ single crystal," J. Lightwave Tech., vol. LT-1, pp. 93-97, Mar. 1983.

[26] R. K. Willardson and A. C. Beer, eds., *Semiconductors and Semimetals*. New York: Academic Press, 1972, ch. 3.

[27] J. D. Krauss and K. R. Carver, *Electromagnetics*, 2d ed., New York: McGraw-Hill, 1973, ch. 15.

[28] S. Ramo, J. Whinnery, and T. Van Duzer, *Fields and Waves in Communication Electronics*, 2d ed., New York: John Wiley & Sons, 1984, ch. 13.

[29] M. A. Butler and S. J. Martin, "Optical fiber magnetic field sensor with nanosecond response time," IEEE doc. no. CH2127-9/85, pp. 316-319, 1985.

[30] A. E. Turner, R. L. Gunshor, and S. Datta, "New class of materials for optical isolators," Appl. Optics, vol. 22, pp. 3152-3154, 1983.

[31] S. J. Martin and M. A. Butler, "Wideband optical fiber magnetic field sensor," SPIE Fiber optic and Laser Sensors III, vol. 566, pp. 197-200, 1985.

[32] J. K. Furdyna, "Diluted magnetic semiconductors: An interface of semiconductor physics and magnetism," J. Appl. Phys., vol. 53, pp. 7637-7643, 1982.

[33] N. Kullensrff and B. Hök, "Temperature independent Faraday rotation near the band gap in $Cd_{1-x}Mn_xTe$," Appl. Phys. Lett., vol. 46, pp. 1016-1018, June 1985.

[34] B. Donovan and T. Medcalf, "The inclusion of multiple reflection in the theory of the Faraday effect in semiconductors," Brit. J. Appl. Phys., vol. 15, pp. 1139-1151, 1964.

[35] C. J. Gabriel and H. Pillar, "Determination of the optical Verdet coefficient in semiconductors and insulators," Appl. Optics, vol. 6, pp. 661-668, April 1967.

[36] E. D. Palik and J. R. Stevenson, "Multiple reflection effects in the Faraday rotation in thin-film semiconductors," J. Appl. Phys., vol. 37, pp. 1982-1988, April 1966

[37] H. Pillar, "Effect of internal reflection on optical Faraday rotation," J. Appl. Phys., vol. 37, pp. 763-767, Feb. 1966.

[38] M. Born and E. Wolf, *Principles of Optics.* London: Pergamon Press, 1959, ch. 1.

[39] J. C. Palais, *Fiber Optic Communications.* Englewood Cliffs, N.J.: Prentice-Hall, Inc., 1984, ch. 11.

[40] W. Canton and J. Katzenstein, "An absolute electric current probe based on the Faraday effect," J. of Research of the NBS, vol. 89, pp. 265-272, May-June 1984.

[41] L. Veeser, G. I. Chandler, and G. W. Day, "Fiber optic sensing of pulsed currents," Los Alamos National Lab report no. LA-UR-1212, April 1986.

[42] H. Sohlström, T. Brogårdh, and U. Holm, "Measurement system for magneto-optic sensor materials," J. Phys. E: Sci. Instrum., vol. 17, pp. 885-889, 1984.

[43] A. Enokihara, M. Izutsu, and T. Sueta, "Optical fiber sensors using the method of polarization-rotated reflection," J. Lightwave Tech., vol. LT-5, pp. 1584-1590, Nov. 1987.

[44] K. Goto, T. Sueta, and T. Makimoto, "Travelling-wave light-intensity modulators using the method of polarization-rotated reflection," J. Quantum Electron., vol. QE-8, pp.486-493, 1972.

[44] K. Goto, T. Sueta, and T. Makimoto, "Travelling-wave light-intensity modulators using the method of polarization-rotated reflection," J. Quantum Electron., vol. QE-8, pp.486-493, 1972.

[45] M. Imai, Y. Terasawa, and Y. Ohtsuka, "Polarization fluctuation characteristics of a highly birefringent fiber system under forced vibration," J. Lightwave Tech., vol. 6, pp. 720-727, May 1988.

[47] A. Papoulis, *Probability, Random Variables, and Stochastic Processes,* 2d ed., New York: McGraw-Hill, 1984, ch. 9.

[48] J. Gower, *Optical Communication Systems.* London: Prentice-Hall, 1984, ch. 14.

[49] B. Hillerich and E. Wiedel, "Polarization noise in single mode fibres and its reduction by depolarizers," Optical and Quantum Electron., vol. 15, pp. 281-287, 1982.

[50] Various discussions with engineers at Boeing Military Airplane Company's Lightning Lab in 1986.

[51] G. M. Wilkinson of Maxwell Labs. Private communication.

[52] J. Adams, "Hall noise in the 6302 current probe," Tektronix Inc., company report, Dec. 1984.

[53] Jim Hatfield of Hatfield and Dawson, Seattle. Private communication.

[54] "Question and answers about biological effects and potential hazards of radio frequency radiation," Office of Science and Technology bulletin no. 56, June 1983.

[55] H. Lee, "Optical polarization bistability using the Faraday effect," Appl. Optics, vol. 26, pp. 3486-3487, Sept. 1987.

[56] J. D. Krauss and K. R. Carver, *Electromagnetics*, 2d ed., New York: McGraw-Hill, 1973, p. 157.

[57] Kao-Feng Tsai, Master of Science Thesis, University of Rhode Island, Department of Electrical Engineering, 1988, p. 4.

[58] H. B. Dwight, *Tables of Integrals and other Mathematical Data,* 4th ed., New York: MacMillan Publishing Co., Inc., 1961, p. 236.

APPENDIX 1 ♦ HALL EFFECT MAGNETOMETER

Clearly, we needed a magnetic field sensor to use as a reference for our magneto-optic sensor. Since no such instrument was available, we made and calibrated a Hall effect magnetic sensor using a sample Hall effect sensor from Texas Instruments. The device was calibrated using a solenoid of known dimensions and turns which we borrowed from the Physics department stockroom.

The Hall sensor that we acquired is represented by the functional block diagram in Figure A1.1, which was gotten from the device's specification sheet. The Hall sensor was the transverse type, with a square area of about 0.16 cm^2.

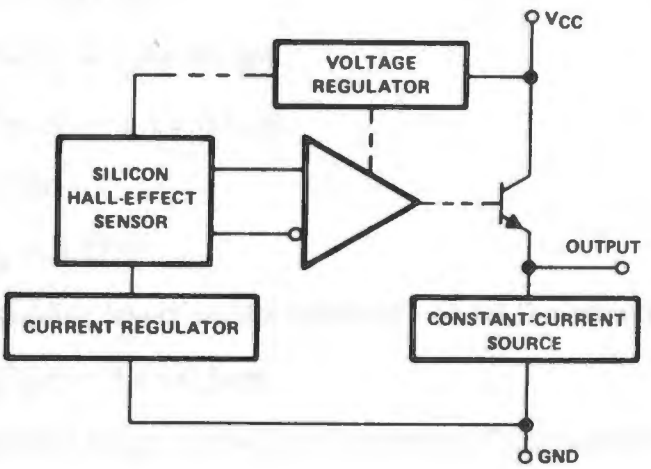

Fig. A1.1 Functional block diagram of Hall sensor

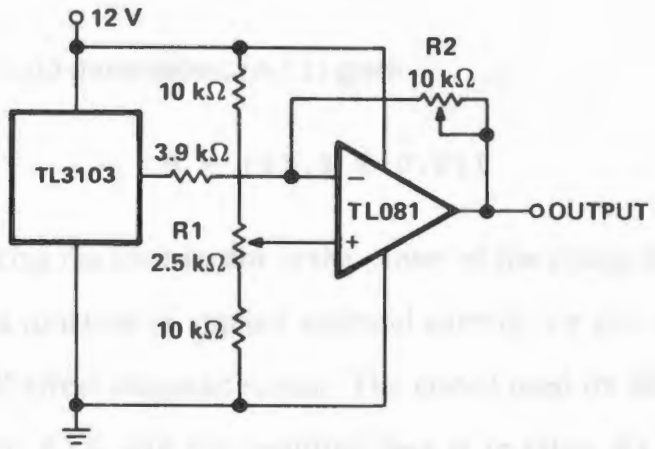

Fig. A1.2 Hall sensor compensation circuit

It is designed to give a linear output voltage proportional to the magnetic field. Using the recommended compensation circuit shown in Figure A1.2 on a breadboard, we attached stiff wire link to the Hall sensor for ease of use, and connected the ouput to a voltmeter.

The solenoid had the following specifications:

Length = L = 15 ± 0.1 cm

inner diameter = d_i = 4.3 ± 0.1 cm

outer diameter = d_o = 6.1 ± 0.1 cm

turns = N = 520

resistance = R_s = 1.27 Ω

There are 2-3 winding layers on the solenoid--we let the effective solenoid radius = r = $(d_i/2 + d_o/2)/2$ = 2.6 ± 0.2 cm.

The theoretical magnetic field at the center of a solenoid is [56]

$$B = \frac{\mu_o NI}{(4r^2 + L^2)^{\frac{1}{2}}} 10^4 \qquad \text{(A1.1)}$$

where I is the current in Amperes, r and L have units of meters, and B is in Gauss.

For the given solenoid dimensions, (A1.1) gives

$$B = (41.3 \pm 0.6)I \qquad (A1.2)$$

Now, by placing the Hall sensor in the center of the solenoid and measuring its ouput voltage as a function of applied solenoid current, we can obtain a sensitivity figure for our Hall effect magnetic sensor. The circuit used for these measurements is shown in Figure A1.4, and the resulting data is in table A1.1. Various power resistors were used to get the different currents. The sensor circuit was set to produce 6.00 volts when B = 0.

Table A1.1 Hall output voltage vs. magnetic field B

I (A)	V_o (V)	ΔV (V)	B (G)
.146	5.98	.02	6.02
.2	5.97	.03	8.25
.24	5.97	.03	9.9
.3	5.96	.04	12.38
.36	5.95	.05	14.86
.4	5.94	.06	16.51
.454	5.92	.08	18.74
.53	5.91	.09	21.87
.6	5.9	.1	24.76
.7	5.89	.11	28.89
.89	5.83	.17	41.27
1.29	5.78	.22	53.24
1.37	5.76	.24	56.54
1.45	5.74	.26	59.84
1.55	5.73	.27	63.97
1.61	5.72	.28	66.44
1.93	5.68	.32	79.65
2.04	5.64	.36	84.19
2.2	5.61	.39	90.79
2.42	5.56	.44	99.87
2.48	5.55	.45	102.35
2.56	5.55	.45	105.65
2.68	5.52	.48	110.6

The plot of this data is shown in Figure A1.3.

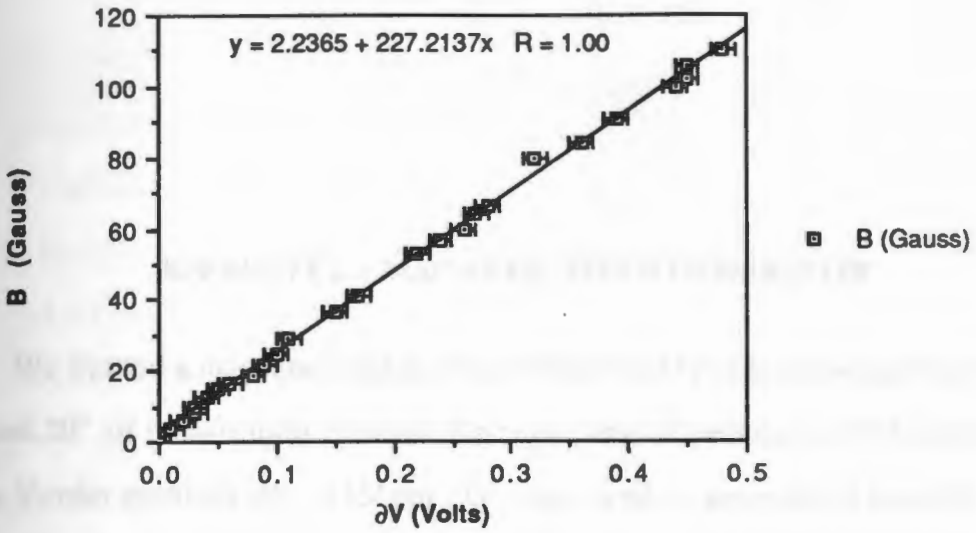

Fig. A1.3 Hall output voltage vs. solenoid B-field

The sensitivity of our device is thus

$$\frac{B}{\Delta V_o} = 227 \pm 3 \text{ Gauss/volt} \qquad \text{(A1.3)}$$

Therefore, every 0.01 volt change is equivalent to ~2.3 Gauss.

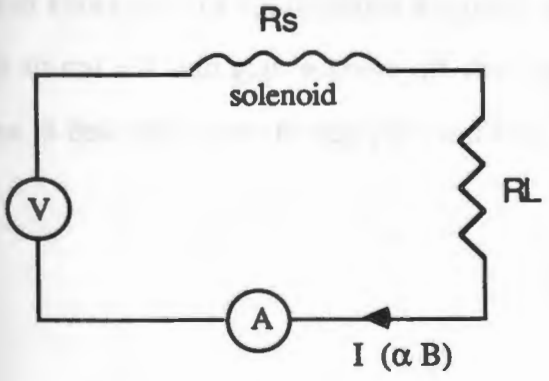

Note:
The Hall device is centered in the solenoid; its output is measured as a function of I.

Fig. A1.4 Set-up for Hall voltage vs. B-field measurement

APPENDIX 2 ◊ MAGNETIC FIELD GENERATOR

We wanted a magnetic field generator that would produce enough flux to cause at least 20° of polarization rotation. Since our crystal sample is 0.363 cm long, and has a Verdet constant of $\sim 0.15° \text{ cm}^{-1} \text{G}^{-1}$, we need to generate at least 350 Gauss. We initially tried making a solenoid utilizing equation (A1.1), but did not have a sufficient current supply in order to realize 350 Gauss (this solenoid had N = 500, L = 9.5 cm, and r = 1.55 cm, giving a theoretical field of B = 0.129NI Gauss). Also, more turns gave more coil resistance and lowered the acheivable current draw. Instead of designing and building a heavy duty current source, I chose to investigate the use of a high permeability toroidal coil with an air gap just large enough to accommodate the crystal. Since we need the B-field parallel to the light propagation direction, the usable flux in this configuration is actually the fringing flux above the gap.

Jim Florance, an applications engineer at Ceramic Magnetics, Inc., was kind enough to cut a 4 mm gap in some off-the-shelf high-μ_r toroids and send them as samples. A description of the sample used is as follows:

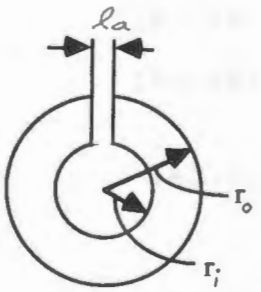

r_o = 1.825 cm
r_i = 1.15 cm
$r_{eff} = (r_o + r_i)/2$ = 1.487 cm
ℓ_a = length of air gap = 0.4 cm
ℓ_m = total mean magnetic path length of toroid = $2\pi r_{eff}$ = 9.346 cm

ℓ_c = effective core length = $\ell_m - \ell_a$
A_c = cross sectional area = a x b = 0.01 x 0.007 = 7×10^{-5} m^2
μ_r = relative permeability of material; *initial* μ_r = 6000.

We will get an estimate of the B-field just above the gap by first calculating the field in the gap for NI Amp-turns on the toroid core. Because the air gap is fairly large, the effective cross sectional area for the gap will be greater than A_c. For $\ell_a <$ b/10, we can approximate the effective cross sectional area of the air gap by $A_a = (a + \ell_a)(b + \ell_a)$, where a and b are the core cross section dimensions, and b < a. For this case, however, the approximation will be poor (since $\ell_a <$ b/10), and fringing will make the actual A_a larger than this approximation. Therefore, we introduce the "fudge factor" γ, and let use $A_a' = \gamma A_a$ for our subsequent calculations. We estimate that $\gamma = 2$ for these rough calculations.

Ojective: Find the flux Φ in the magnetic "circuit" for NI Amp-turns. The magnetic field in the air gap will then be $B_a = \Phi/A_a'$. Additional definitions are as follows:

Φ = magnetic flux (Webers)
H_c = field in air gap (Amps/m)
H_a = field in core (Amps/m)
B_a = field in air gap (Tesla)
$\ell_m = \ell_a + \ell_c$ (m)
N = number of coil turns on core
μ_o = vacuum permeability = 400π nH

$$NI = H_c\ell_c + H_a\ell_a \qquad \text{(A2.1)}$$

$$H_a\ell_a = \Phi\ell_a/(\mu_o A_a') \qquad \text{(A2.2a)}$$

$$H_c\ell_c = \Phi\ell_c/(\mu_o\mu_r A_c) \qquad \text{(A2.2b)}$$

$$\Phi = \frac{NI}{(\ell_c/\mu_o\mu_r A_c) + (\ell_a/\mu_o A_a')} \qquad \text{(A2.3)}$$

$$B_a = \Phi/A_a' = \frac{\mu_o NI}{(\ell_c A_a'/\mu_r A_c) + \ell_a} \qquad \text{(A2.4)}$$

In order to get a feel for how much of an increase in magnetic field this particular core will provide, we will now define an effective relative permeability, μ_{eff}, that applies to the entire core, air gap and all:

$$\mu_{eff} = \frac{\text{what } B_a \text{ would be with no magnetic core, (e.g. air)}}{\text{what } B_a \text{ is with the magnetic core (i.e. } \mu_r > 1)}$$

$$= \frac{B_a \text{ when } \mu_r = 1}{B_a \text{ when } \mu_r > 1}$$

$$= \frac{A_a' \ell_c + A_c \ell_a}{(\ell_c A_a'/\mu_r) + \ell_a A_c} \qquad \text{(A2.5)}$$

From our definition, $A_a' = \gamma A_a = 2(a + \ell_a)(b + \ell_a) = 3.1 \times 10^{-4}$ m^2. If we make the simplifying assumption that the specified initial permeability of the core is equal to μ_r (far from the saturation point, and at low frequencies, this is a pretty good assumption), then $\mu_r = 6000$. Using equation (A2.5) we get $\mu_{eff} \simeq 97$. Considering how large the air gap is, this is fairly good.

Now, using these same parameters in equation (A2.4) and converting to units of Gauss we get the magnetic field inside the air gap:

$$B_a = 3.12NI \text{ Gauss} \qquad \text{(A2.6)}$$

Thus, if our maximum coil current was 200 mA, we would need ~600 turns of wire to produce our desired 350 Gauss inside the gap. Since we will be depending on the fringing field outside the gap to produce Faraday rotation in our sample, we actually need more than 600 turns.

Considering the above calculations, we put approximately 1000 turns of #26 magnet wire on the core, and measured magnetic fields in and above the gap using

the circuit in Figure A2.1. Measurements were taken using the center of the Hall sensor as the reference for distance measurements along y, as shown in the Figure. This data is presented in Table A2.1 A plot of the coil current versus B in the gap's center in plotted in Figure A2.2. (Note that our theoretically approximated relationship in (A2.5/A2.6) happens to be quite close to experiment: for example, for N = 1000 and I = 100 mA, B_{theory} = 300 G and $B_{experiment}$ = 308 G for the gaps center.)

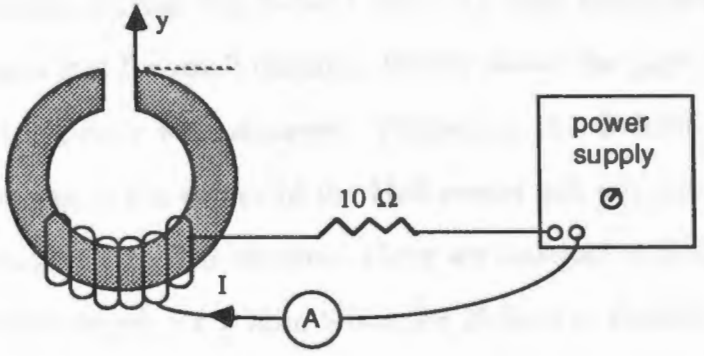

Fig. A2.1 Set-up for B-field measurement above toroid gap

Frequency Response of Toriodal Coil

Since the inductance was naturally quite large, the frequency response was unavoidably low. The configuration in Figure A2.3 was used to roughly measure the frequency response of the coil. Since the 3 dB down point is at f ≃ 60 Hz, the inductance is L ≃ R/2πf ≃ 24 mH.

Measurement of B at the location above the gap where the beam transversed the crystal

Immediately after measuring the coil current versus polarization rotation in the crystal, we measured the magnetic field using the Hall device at the same location where the light beam transversed the $Cd_{.5}Mn_{.5}Te$ sample. This measurement gives an empirical relationship between the coil current and the B-field which produced

the experimental Faraday rotation. Using this relationship, we will be able to plot the polarization rotation $\Delta\theta$ versus the magnetic field B.

The laser beam was 0.8 mm above the gap in our experiment, so it is here that we will measure the magnetic field using the Hall sensor. Though the integrated Hall sensor package has dimensions of .4 cm x .4 cm, the actual Hall device centered inside this is about half this size according to the manufacturer, so a centered Hall sensor will effectively average the B-field over $\sim$2 mm. Fortunately, the data in Table A2.1 indicates that for small distance directly above the gap's center (e.g. 1-2 mm), the B-field is linear with distance. Therefore, the B-field measured at a distance above the gap to the center of the Hall sensor will give an average B-field reading that corresponds to that distance. Here we estimate a physical placement error of the Hall sensor of $\sim\pm$.2 mm. Since the B-field is linearly related to the distance above the gap for small distances, a $\pm$ .2 mm uncertainty in distance corresponds to a $\pm$ 20% uncertainty in the B-field that we measure.

Centering the Hall sensor above the gap and securing it in place, we measured the coil current versus Hall output voltage, thus obtaining I versus B, as tabulated in Table A2.2. Figures A2.4 and A2.5 are plots of this data. From Figure A2.5, we now have a relationship between I and B:

$$B\ (\text{Gauss}) = 1.975I(\text{mA}) \qquad (A2.7)$$

This relation will allow us to calculate the Verdet constant from the measurements of chapter 3.

Table A2.1 Measured Magnetic Field above Air Gap vs. Coil Current

I (mA)	Gap Center			y = 1 mm			y = 2 mm		
	V_o (volts)	ΔV_o	B (G)	V_o (volts)	ΔV_o	B (G)	V_o (volts)	ΔV_o	B (G)
1.06	6.03	0.03	6.8	6.01	0.01	2.3	6.00	0.0	0.0
3.07	6.05	0.05	11.4	6.02	0.02	4.5	6.01	0.01	2.3
5.27	6.08	0.08	18.2	6.04	0.04	9.1	6.02	0.02	4.5
7.01	6.10	0.10	22.7	6.05	0.05	11.4	6.03	0.03	6.8
10.51	6.15	0.15	34.1	6.07	0.07	15.9	6.04	0.04	9.1
13.20	6.19	0.19	43.2	6.09	0.09	20.5	6.04	0.04	9.1
16.64	6.24	0.24	54.5	6.10	0.10	22.7	6.05	0.05	11.4
19.46	6.28	0.28	63.6	6.12	0.12	27.3	6.06	0.06	13.7
25.1	6.35	0.35	79.5	6.15	0.15	34.1	6.08	0.08	18.2
30.5	6.43	0.43	97.7	6.17	0.17	38.6	6.09	0.09	20.5
40.0	6.56	0.56	127.2	6.23	0.23	52.5	6.12	0.12	27.3
50.0	6.69	0.69	156.8	6.30	0.30	68.2	6.14	0.14	31.8
60.1	6.81	0.81	184.0	6.32	0.32	72.7	6.16	0.16	36.3
70.2	6.95	0.95	215.8	6.34	0.34	77.2	6.80	0.18	40.9
79.9	7.08	1.08	245.4	6.44	0.44	100.0	6.22	0.22	50.0
89.9	7.22	1.22	277.2	6.48	0.48	109.1	6.24	0.24	54.3
100.2	7.35	1.35	306.7	6.54	0.54	122.7	6.27	0.27	61.3
110.4	7.49	1.49	338.5	6.60	0.60	136.3	6.31	0.31	70.4
121.3	7.63	1.63	370.4	6.66	0.66	150.0	6.32	0.32	72.7
130.4	7.75	1.75	397.6	6.7	0.70	159.0	6.35	0.35	79.5
142.6	7.9	1.9	431.7	6.77	0.77	174.9	6.39	0.39	88.6
151.0	8.0	2.0	454.4	6.74	0.74	168.1	6.38	0.38	86.3
159.7	8.09	2.09	474.8	6.88	0.88	199.9	6.42	0.42	95.4
170.2	8.25	2.25	511.2	6.92	0.92	209.0	6.50	0.5	113.6
180.6	8.37	2.37	538.5	7.06	1.06	240.8	6.54	0.54	122.7
189.5	8.46	2.46	558.9	6.9	0.9	204.5	6.45	0.45	102.2
204.	8.58	2.58	586.2	6.94	0.94	213.6	6.52	0.52	118.1
214.	8.62	2.62	595.3	7.08	1.08	245.4	6.58	0.58	131.8
228.	8.69	2.69	611.2	7.14	1.14	259.0	6.62	0.62	140.9
237.	8.71	2.71	615.7	7.1	1.1	249.9	6.6	0.6	136.3
254.	8.75	2.75	624.8	7.14	1.14	259.0	6.6	0.6	136.3
268.	8.78	2.78	631.7	7.16	1.16	263.6	6.63	0.63	143.1
278.	8.8	2.8	636.2	7.17	1.17	265.8	6.63	0.63	143.1
288.	8.82	2.82	640.7	7.32	1.32	299.9	6.69	0.69	156.8
300.	8.85	2.85	647.6	7.4	1.4	318.1	6.73	0.73	165.9
310.	8.86	2.86	649.8	7.4	1.4	318.1	6.76	0.76	172.7
320.	8.85	2.85	647.6	7.36	1.36	309.0	6.7	0.7	159.1
330.	8.87	2.87	652.1	7.28	1.28	290.8	6.65	0.65	147.7
340.	8.88	2.88	654.4	7.26	1.26	286.3	6.64	0.64	145.4
350.	8.88	2.88	654.4	7.26	1.26	286.3	6.64	0.64	145.4
360.	8.83	2.83	643.0	7.22	1.22	277.2	6.56	0.56	127.2
370.	8.84	2.84	645.3	7.2	1.2	272.7	6.58	0.58	131.8
380.	8.83	2.82	643.0	7.2	1.2	272.7	6.64	0.64	145.4
390.	8.85	2.85	647.6	7.21	1.21	274.9	6.65	0.65	147.7

Table A2.1--cont. Measured Magnetic Field above Air Gap vs. Coil Current

I (mA)	Gap Center			y = 1 mm			y = 2 mm		
	V_o	ΔV_o	B	V_o	ΔV_o	B	V_o	ΔV_o	B
400.	8.87	2.87	652.1	7.24	1.24	281.7	6.67	0.67	152.2
410.	8.89	2.89	656.6	7.24	1.24	281.	6.67	0.67	152.2
420.	8.92	2.92	663.5	7.25	1.25	284.0	6.68	0.68	154.5
430.	8.93	2.93	665.7	7.3	1.3	295.4	6.7	0.7	159.0
440.	8.95	2.95	670.3	7.33	1.33	302.2	6.71	0.71	161.3
450.	8.88	2.88	654.4	7.24	1.24	281.7	6.67	0.67	152.2
460.	8.89	2.89	656.6	7.26	1.26	286.3	6.65	0.65	147.7
470.	8.95	2.95	670.3	7.28	1.28	290.8	6.68	0.68	154.5
476.	8.95	2.95	670.3	7.28	1.28	290.8	6.68	0.68	154.5

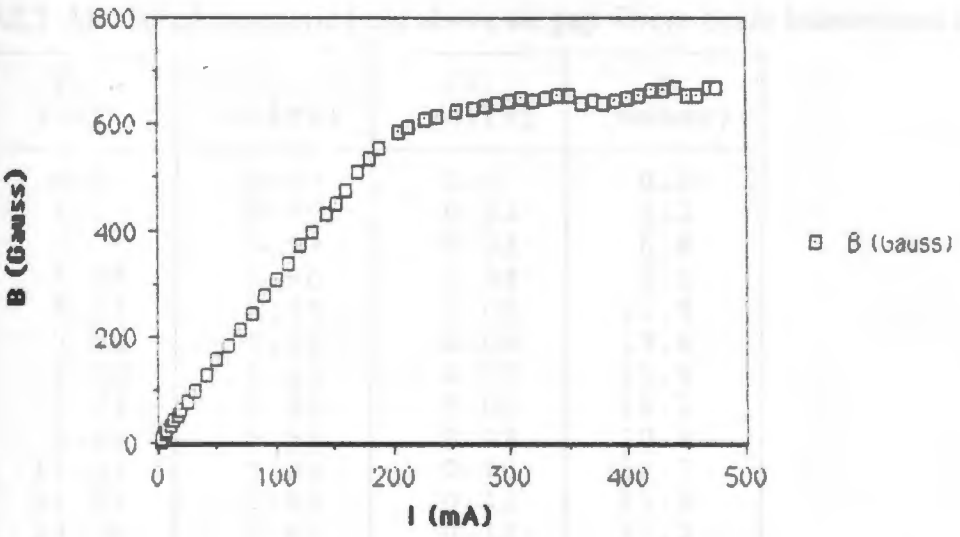

Fig. A2.2 Plot of measured B-field in air gap vs. coil current

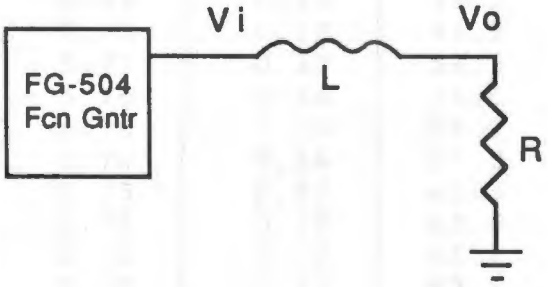

$$Vo/Vi = R/(j\omega L + R)$$

Fig. A2.3 Set-up for measuring frequency response of coil

Table A2.2 Measured magnetic field above air gap where beam transversed crystal

I (mA)	V_o (volts)	ΔV_o (volts)	B (Gauss)
0.0	6.00	0.0	0.0
1.	5.99	0.01	2.3
3.	5.97	0.03	6.8
4.18	5.96	0.04	9.1
5.69	5.95	0.05	11.3
7.08	5.94	0.06	13.6
8.30	5.93	0.07	15.9
9.04	5.92	0.08	18.2
9.85	5.91	0.09	20.4
11.57	5.90	0.10	22.7
12.47	5.89	0.11	25.0
13.38	5.88	0.12	27.2
14.7	5.87	0.13	29.5
16.18	5.86	0.14	31.8
16.90	5.85	0.15	34.0
17.93	5.84	0.16	36.3
19.4	5.83	0.17	38.6
20.5	5.82	0.18	40.9
21.7	5.81	0.19	43.1
22.4	5.80	0.20	45.4
23.9	5.79	0.21	47.7
25.2	5.78	0.22	49.9
26.1	5.77	0.23	52.2
26.6	5.76	0.24	54.5
28.0	5.75	0.25	56.7
29.3	5.74	0.26	59.0
31.1	5.73	0.27	61.3
32.4	5.72	0.28	63.6
33.3	5.71	0.29	65.8
34.3	5.70	0.30	68.1
36.8	5.68	0.32	72.6
38.5	5.66	0.34	77.2
41.0	5.64	0.36	81.7
43.1	5.62	0.38	86.3
45.5	5.60	0.40	90.8
47.7	5.58	0.42	95.3
52.4	5.54	0.46	104.4
56.2	5.50	0.50	113.5
61.7	5.46	0.54	122.6
66.3	5.42	0.58	131.7
70.2	5.38	0.62	140.7
75.2	5.34	0.66	149.8
79.6	5.30	0.70	158.9
83.6	5.26	0.74	168.0

Table A2.2--cont.

I (mA)	V_o (volts)	ΔV_o (volts)	B (Gauss)
88.8	5.22	0.78	177.1
93.0	5.18	0.82	186.1
97.8	5.14	0.86	195.2
102.5	5.10	0.90	204.3
107.2	5.06	0.94	213.4
111.8	5.02	0.98	222.5
116.3	4.98	1.02	231.5
121.1	4.94	1.06	240.6
125.0	4.90	1.10	249.7
130.2	4.86	1.14	258.8
135.2	4.82	1.20	272.4
138.7	4.78	1.24	281.5
146.4	4.72	1.28	290.6
150.7	4.68	1.32	299.6
156.2	4.64	1.36	308.7
160.4	4.60	1.40	317.8
164.5	4.56	1.44	326.9
170.3	4.52	1.48	336.0
174.4	4.48	1.52	345.0
179.0	4.44	1.56	345.0
184.4	4.40	1.60	363.2
189.2	4.36	1.64	372.3
193.6	4.32	1.68	381.4
199.4	4.28	1.72	390.4
204.	4.24	1.76	399.5
209.	4.20	1.80	408.6
214.	4.16	1.84	417.7
220.	4.12	1.88	426.8
226.	4.08	1.92	435.8
234.	4.04	1.96	444.9
242.	4.00	2.0	454.0
255.	3.96	2.04	463.1
271.	3.92	2.08	472.2
288.	3.88	2.12	481.2
310.	3.84	2.16	490.3
330.	3.80	2.20	499.4
349.	3.76	2.24	508.5
375.	3.72	2.28	517.6
399.	3.68	2.32	526.6
413.	3.68	2.32	526.6
428.	3.64	2.36	535.7
436.	3.65	2.35	533.4
447.	3.68	2.32	526.6

Table A2.2--cont.

I (mA)	V_o (volts)	ΔV_o (volts)	B (Gauss)
452.	3.63	2.37	538.
460.	3.60	2.40	544.8
501.	3.56	2.44	553.9

notes: V_o is the output from the Hall device. From calibration of the Hall sensor in appendix 1, $B = 227 \cdot \Delta V_o$.

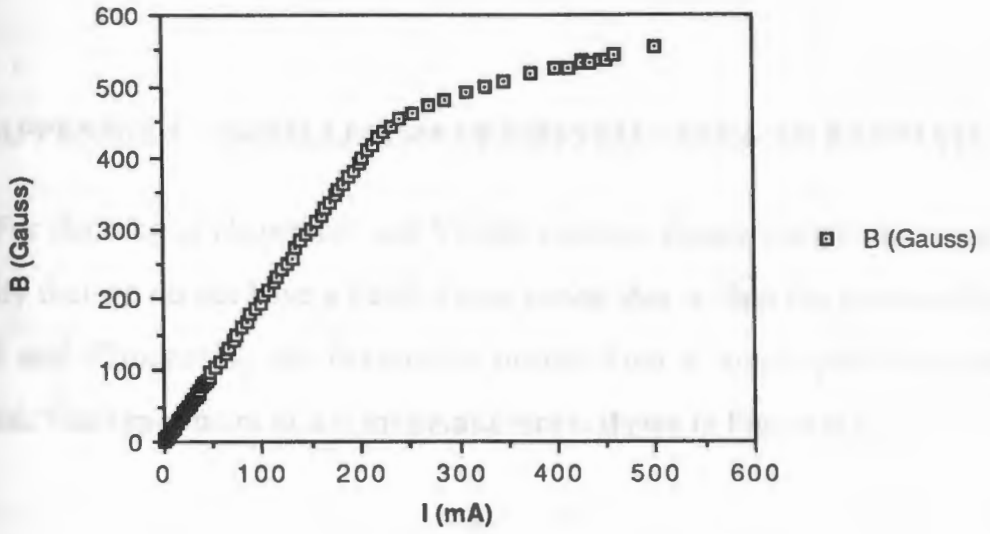

Fig. A2.4 Plot of I vs. B: 0-500 Gauss

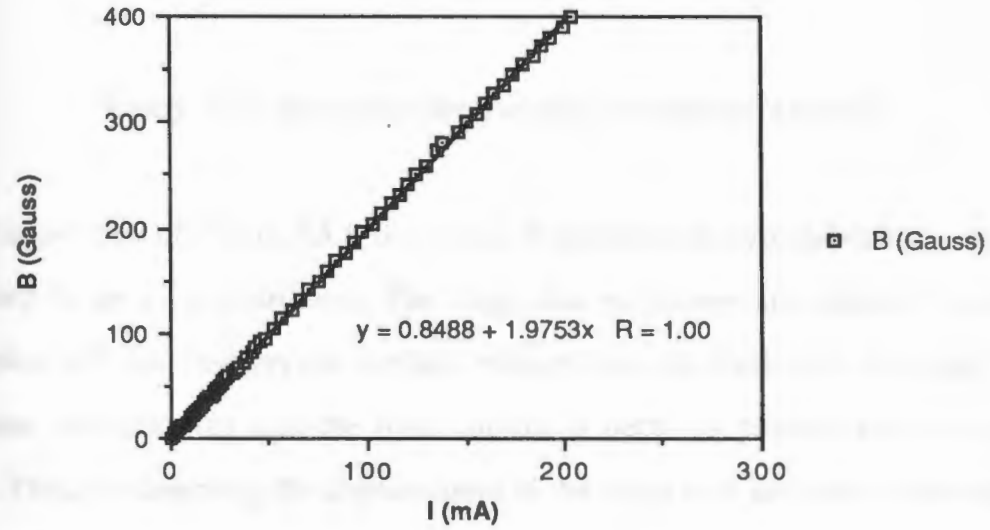

Fig. A2.5 Plot of I vs. B: 0-200 Gauss

APPENDIX 3 ◊ PARALLELISM OF CRYSTAL SIDES--AN ESTIMATE

For the sake of absorption and Verdet constant measurements, we would like to verify that we do not have a Fabry-Perot cavity, that is, that the beam exiting the crystal and illuminating the detector is purely from a "single-pass" through the material. The experiment to test for parallelism is shown in Figure A3.1.

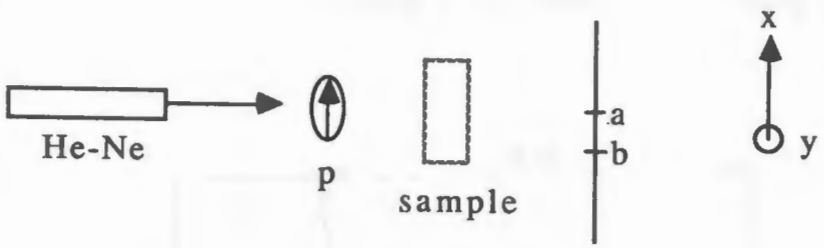

Figure A3.1 Set-up for determining parallelism of crystal

In the upper part of Figure A3.1, the crystal is mounted on a rotatable stage which is mounted to an x-y-z positioner. The stage and positioner are adjusted until the reflection off the first crystal surface reflects directly back into the laser light aperture, thus assuring that the front surface is perfectly parallel to the incident beam. Thus, by observing the displacement of the beam with and without the crystal, we can estimate the angle between the front and back crystal surface (see Figure A3.2). The beam location at points a (without the crystal) and b (with the crystal) were measured relative to each other for both x and y directions, using the

micro-positioner scales on the x-y-z positioner that held the photodetector. To locate position, the x-y-z positioner holding the detector was carefully adjusted for maximum intensity for each case.

Experimental results

Measurements were made twice and averaged. Δx and Δy are the measured displacements in the x and y directions.

Measurement 1:	$\Delta x = 1.67$ mm	$\Delta y = 5.28$ mm
Measurement 2:	$\Delta x = 1.71$ mm	$\Delta y = 5.25$ mm
	$\Delta x_{avg} = 1.69$ mm	$\Delta y_{avg} = 5.265$ mm

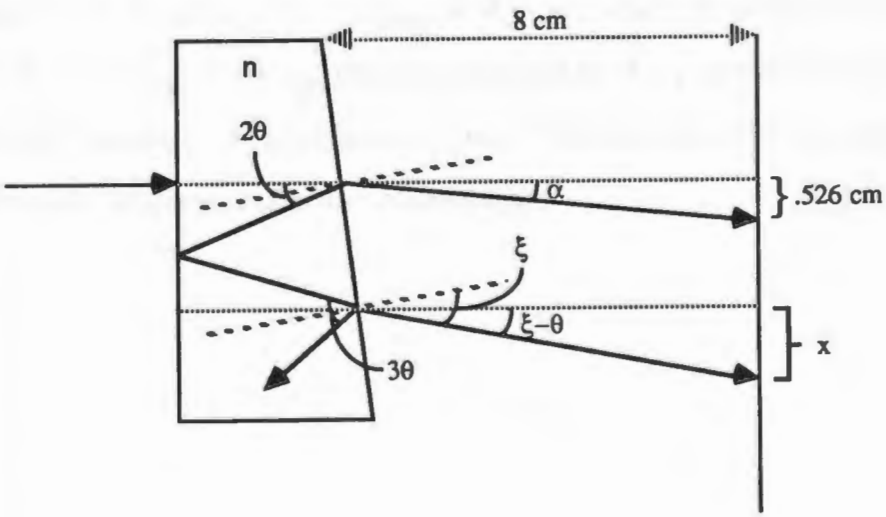

Fig. A3.2 Ray analysis of light in non-parallel crystal

From Figure A3.2, we have

$$\alpha \simeq \tan^{-1}(\Delta x_{avg}/80\text{mm}) = 1.21^{\circ}$$

From Snell's law we get

$$n\sin\theta = \sin(\theta + \alpha) \qquad \text{(A3.1)}$$

For $n \simeq 3$ and $\alpha = 1.21°$, (A3.1) is iteratively solved to give $\theta = 0.6°$.

In estimating the distance between the first and second beam at the plane in Figure A3.2, we will make the worse case assumption that "h" is negligibly small. Using Snell's law again we have

$$n\sin 3\theta = \sin\xi \qquad \text{(A3.2)}$$

For $n \simeq 3$ and $\theta = 0.6°$, (A3.2) gives $\xi = 5.41°$ and $\xi - \theta = 4.81°$. Now,

$$\tan(\xi - \theta) \simeq \ell/8\text{cm} \qquad \text{(A3.3)}$$

From (A3.3), $\ell = 0.67$ cm. Thus, the distance between the first and second beam at the plane of the detector is $\ell - \Delta x_{avg} = 0.5$ cm, which is outside the detector's aperture. Since $\Delta x_{avg} < \Delta y_{avg}$, the displacement in the y direction will be greater than 0.5 cm. Therefore, the detector only "sees" the single pass beam, and we do not need to consider multiple reflection phenomena.

APPENDIX 4 ◊ REFRACTIVE INDEX MEASUREMENT

We will make this measurement using two different methods: (1) measuring the refraction of the light beam, and (2) finding Brewsters angle.

Method 1

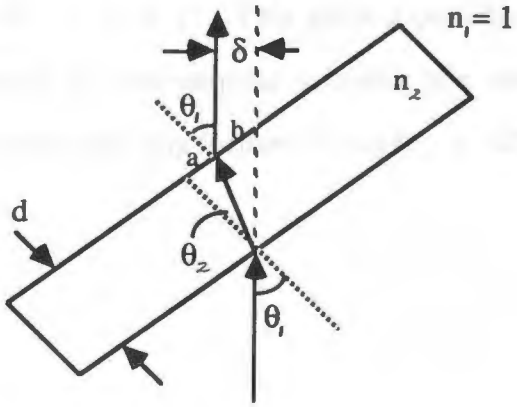

$$\tan\theta_1 = \frac{a + b}{d} \; ; \; \tan\theta_2 = a/d \; ; \; \cos\theta_1 = \delta/b \; ; \; b = \delta/\cos\theta_1$$

Making substitutions,

$$\tan\theta_2 = (d\tan\theta_1 - \delta/\cos\theta_1)/d$$

$$\theta_2 = \tan^{-1}\left[\frac{d\tan\theta_1 - \delta/\cos\theta_1}{d}\right] \qquad \text{(A4.1)}$$

$$n_2 = \sin\theta_1/\sin\theta_2 \qquad \text{(A4.2)}$$

From experiment, $\delta = 1.3 \pm 0.2$ mm, d = 3.63 ± 0.01 mm, and $\theta_1 = 31 \pm 1°$. From (A4.1), $\theta_2 = 10.37°$, which gives from (A4.2) $n_2 = 2.86$. The large tolerances on δ, however, yields a possible range for n_2 of 2.14 ($\delta = 1.1$ mm) to 4.37 ($\delta = 1.5$ mm).

Method 2

Using horizontally polarized laser light, the crystal is tilted until a minimum intensity is found from the reflected beam--this is Brewter's angle. Refering to Figure A4.1, $\tan\theta_1 = n_2$ at this angle. Experimentally, we find a minimum reflected intensity at $\theta_1 = 72 \pm 1°$. This gives a possible range for n_2 of 2.9 to 3.27. Since our research did not require knowing the refractive index with high accuracy, we did not pursue this any further. Using $\theta_2 = 72°$, we will let $n_2 = 3.08$.

APPENDIX 5 ◊ ABSORPTION MEASUREMENT

We measured the absorption immediately after measuring the Verdet constant, using the estimated value of refractive index (Appendix 4), and the fact that the crystal sides are non-parallel. The procedure simply uses the set-up of Figure A5.1, measuring the intensity with and without the crystal in the beam's path. The detector is mounted on an x-y-z positioner, and is adjusted for a maximum intensity reading for each case.

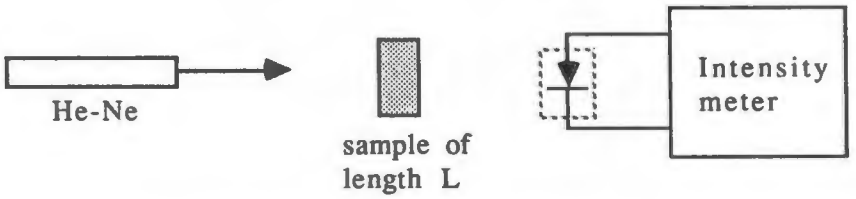

Fig. A5.1 Absorption measurement set-up

Intensity without crystal = I_{WO} = 14.85 x 10^{-4} Watts

Intensity with crystal = I_W = 3.88 x 10_{-4} Watts

Transmission = $T_m = I_W/I_{WO}$ = 26.13%

Since we know the refractive index of the crystal is approximately 3.1, we can estimate the material's intrinsic absorption α. Assuming two reflections off the crystal, one from the front surface and one from the back surface, the theoretical transmission due to reflection losses is [57]

$$T_r = \left[\frac{4n}{(n+1)^2}\right]^2 \qquad \text{(A5.1)}$$

For $n = 3.1$, $T_r = 0.554$. The difference between this and the measured transmission, T_m, is due to scattering and absorption. Neglecting the relatively small amount of scattering, the absorption can thus be found from

$$1 - (T_r - T_m) = e^{-\alpha L} \qquad \text{(A5.2)}$$

where L is the length of the material (cm) and α is the absorption coefficient (cm^{-1}). For $T_r = 0.544$ and $T_m = 0.26$, $\alpha = \underline{\underline{0.92\ cm^{-1}}}$.

This value compares well with previously published work. For $Cd_{.55}Mn_{.45}Te$ at λ = 621.6 nm, the calculated absorption from one paper was ~ 1.4 cm^{-1} [30].

APPENDIX 6 ◊ MEASUREMENT OF WAVE-PLATE RETARDANCE

The quarter wave-plate retardance was measured using the basic configuration of Figure A6.1. The retarder holder/positioner set-up the same way as in chapter 6. The quarter wave-plate (QWP) axes were set 45° to the linear input polarization, and the detector was mounted on an x-y-z positioner in order to adjust for maximum intensity readings.

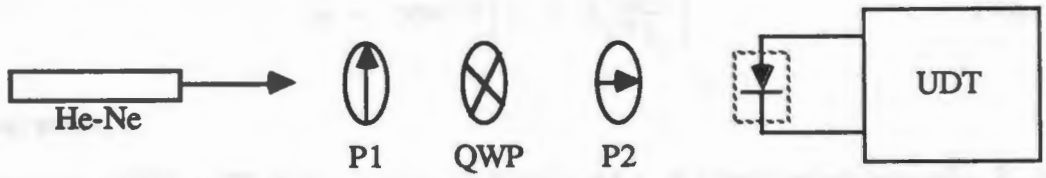

P1, P2: polarizers with transmission axes as shown
UDT: United detector Tech. intensity meter.
QWP: quarter wave plate

Fig. A6.1 Set-up for retardance measurement

The Jones Matrices for this system are

$$\begin{bmatrix} E_{xo} \\ E_{yo} \end{bmatrix} = \tfrac{1}{2}\gamma \underset{6}{\begin{bmatrix} 1 & 0 \\ 0 & 0 \end{bmatrix}} \underset{5}{\begin{bmatrix} 1 & -1 \\ 1 & 1 \end{bmatrix}} \underset{4}{\begin{bmatrix} 1 & 0 \\ 0 & e^{-j\phi} \end{bmatrix}} \underset{3}{\begin{bmatrix} 1 & 1 \\ -1 & 1 \end{bmatrix}} \underset{2}{\begin{bmatrix} 0 \\ E_y \end{bmatrix}} \underset{1}{}$$

Matrix descriptions:

(1) linear input light on y axis

(2) rotates input to coordinates of QWP (i.e. gives components on QWP)

(3) wave-plate with retardance ϕ

(4) rotates back to original coordinates

(5) polarizer P2

(6) resulting output E-field components (system attenuation = γ)

Multiplying the Jones Matrices together we get

$$E_{xo} = \tfrac{1}{2}\gamma E_y(1 - e^{-j\phi}) \qquad \text{(A6.1a)}$$

$$E_{yo} = \tfrac{1}{2}\gamma E_y(1 - e^{-j\phi}) \qquad \text{(A6.1b)}$$

$$I_{xo} = E_{xo} \cdot E_{xo}^{*} = \tfrac{1}{2}\gamma^2 I_y(1 - \cos\phi) \qquad \text{(A6.2)}$$

Solving for the retardance ϕ from (A6.2) we have

$$\phi = \cos^{-1}\left[1 - 2\frac{I_{xo}}{\gamma^2 I_y}\right] \qquad \text{(A6.3)}$$

Measurements

Without the QWP or P2 in the system of Figure A6.1, the total input intensity, I_y, out of P1 was 16.69×10^{-4} Watts. $I_{xo} = 2.35 \times 10^{-4}$ W. Rotating P2 90° from that shown in Figure A6.1 gives the intensity component I_{yo}--$I_{yo} = 4.00 \times 10^{-4}$ W. The attenuation due to the QWP and P2 is thus

$$\gamma^2 = (I_{xo} + I_{yo})/I_y \qquad \text{(A6.4)}$$
$$= 0.3805$$

From (A6.3), the retardance is calculated to be $\phi = 74.9°$.

APPENDIX 7 ◊ JONES MATRIX CALCULATIONS

Here we will evaluate the matrix "chain" of Figure 5.3 in order to find the intensity relation for an output beam of the Wollaston prism in Figure 5.2. The subscript numbers that we use correspond to the matrix numbers in Figure 5.3.

$$\begin{bmatrix} E_{x1} \\ E_{y1} \end{bmatrix} = \begin{matrix} E_x e^{-(\alpha_x + j\beta_x)\ell} \\ E_y e^{-(\alpha_y + j\beta_y)\ell} \end{matrix}$$

For $\theta_r = 45°$ we have:

$$\begin{bmatrix} E_{x2} \\ E_{y2} \end{bmatrix} = \begin{matrix} \sqrt{2}/2\,(E_x e^{-(\alpha_x + j\beta_x)\ell} + E_y e^{-(\alpha_y + j\beta_y)\ell}) \\ \sqrt{2}/2\,(-E_x e^{-(\alpha_x + j\beta_x)\ell} + E_y e^{-(\alpha_y + j\beta_y)\ell}) \end{matrix}$$

$$\begin{bmatrix} E_{x3} \\ E_{y3} \end{bmatrix} = \begin{matrix} E_{x2} \\ E_{y2} e^{-j\phi} \end{matrix}$$

$$\begin{bmatrix} E_{x4} \\ E_{y4} \end{bmatrix} = \begin{matrix} E_{x2}\cos\theta_F + E_{y2}\sin\theta_F e^{-j\phi} \\ -E_{x2}\sin\theta_F + E_{y2}\cos\theta_F e^{-j\phi} \end{matrix}$$

Since it is intensity we are ultimately after, we will not consider the sign change at the mirror (matrix 5 in Fig. 5.2). Continuing with the output from matrix 6 we have

$$\begin{bmatrix} E_{x6} \\ E_{y6} \end{bmatrix} = \begin{matrix} E_{x4} \\ E_{y4} e^{-j\phi} \end{matrix}$$

$$\begin{bmatrix} E_{x7} \\ E_{y7} \end{bmatrix} = \begin{matrix} E_{x4}\cos\theta_r - E_{y4} e^{-j\phi}\sin\theta_r \\ E_{x4}\sin\theta_r + E_{y4} e^{-j\phi}\cos\theta_r \end{matrix}$$

For $\theta_r = 45°$:

$$\begin{bmatrix} E_{x8} \\ E_{y8} \end{bmatrix} = \begin{matrix} \sqrt{2}/2\,(E_{x4} - E_{y4} e^{-j\phi}) e^{-(\alpha_x + j\beta_x)\ell} \\ \sqrt{2}/2\,(E_{x4} + E_{y4} e^{-j\phi}) e^{-(\alpha_y + j\beta_y)\ell} \end{matrix}$$

For $\theta_w = 45°$, one Wollaston output beam is

$$0.5(E_{x8} + E_{y8}) = \sqrt{2}/2\left[(E_{x4}(e^{-(\alpha_x + j\beta_x)\ell} + e^{-(\alpha_y + j\beta_y)\ell}) + E_{y4}(e^{-(\alpha_y + j\beta_y)\ell} - e^{-(\alpha_x + j\beta_x)\ell})e^{-j\phi}\right]$$

For the case where the fiber eigenaxes are equally excited at the input (i.e., $E_x = E_y$), E_{x4} and E_{y4} are put in terms of E_{in}, and the system loss factor γ is included, we have

$$\begin{aligned}
&0.5(E_{x8} + E_{y8})/(\gamma 2E_{in}) = \\
&(e^{-(\alpha_x + j\beta_x)\ell} + e^{-(\alpha_y + j\beta_y)\ell})^2\cos\theta_F \\
&+ (e^{-(\alpha_x + j\beta_x)\ell} + e^{-(\alpha_y + j\beta_y)\ell}) \cdot \\
&(-e^{-(\alpha_x + j\beta_x)\ell} + e^{-(\alpha_y + j\beta_y)\ell})\sin\theta_F e^{-j\phi} \\
&- (e^{-(\alpha_y + j\beta_y)\ell} - e^{-(\alpha_x + j\beta_x)\ell})e^{-j\phi}\sin\theta_F \cdot \\
&(e^{-(\alpha_y + j\beta_y)\ell} + e^{-(\alpha_x + j\beta_x)\ell}) \\
&+ (e^{-(\alpha_y + j\beta_y)\ell} + e^{-(\alpha_x + j\beta_x)\ell})^2\cos\theta_F e^{-2j\phi} \cdot \\
&= (e^{-(\alpha_x + j\beta_x)\ell} + e^{-(\alpha_y + j\beta_y)\ell})^2\cos\theta_F \\
&+ (e^{-(\alpha_y + j\beta_y)\ell} - e^{-(\alpha_x + j\beta_x)\ell})^2\cos\theta_F e^{-2j\phi} \\
&= (e^{-2(\alpha_x + j\beta_x)\ell} + e^{-2(\alpha_y + j\beta_y)\ell} \\
&+ 2e^{-(\alpha_x + \alpha_y)\ell}e^{-j(\beta_x + \beta_y)\ell})\cos\theta_F \\
&+ (e^{-(\alpha_y + j\beta_y)\ell} + e^{-(\alpha_x + j\beta_x)\ell} \\
&- 2e^{-(\alpha_x + \alpha_y)\ell}e^{-j(\beta_x + \beta_y)\ell})\cos\theta_F e^{-j2\phi} \\
&= (e^{-2(\alpha_x + j\beta_x)\ell} + e^{-2(\alpha_y + j\beta_y)\ell})(1 + e^{-j2\phi})\cos\theta_F \\
&+ (2e^{-(\alpha_x + \alpha_y)\ell}e^{-j(\beta_x + \beta_y)\ell})(1 - e^{-j2\phi})\cos\theta_F \\
&= \cos\theta_F\left[(1 + e^{-j2\phi})(e^{-2(\alpha_x + j\beta_x)\ell} + e^{-2(\alpha_y + j\beta_y)\ell})\right. \\
&\left.+ (1 - e^{-j2\phi})(2e^{-(\alpha_x + \alpha_y)\ell}e^{-j(\beta_x + \beta_y)\ell})\right]
\end{aligned}$$

= E-field of one Wollaston prism output beam = E_O.

The output intensity of this beam is

$$I_O = E_O \cdot E_O^* = \cos^2\theta_F\left[(CD + EF) \cdot (C^*D^* + E^*F^*)\right]$$

where

$$C = 1 + e^{-j2\phi}$$
$$D = e^{-2(\alpha_x + j\beta_x)\ell} + e^{-2(\alpha_y + j\beta_y)\ell}$$
$$E = 1 - e^{-j2\phi}$$
$$F = 2e^{-(\alpha_x + \alpha_y)\ell} e^{-j(\beta_x + \beta_y)\ell}$$

$$I_o = \cos^2\theta_F (CC^*DD^* + EE^*FF^* + CDE^*F^* + EFC^*D^*)$$

$$CC^* = 4\cos^2\phi$$
$$EE^* = 4\sin^2\phi$$
$$DD^* = e^{-4\alpha_x\ell} + e^{-4\alpha_y\ell} + 2e^{-2(\alpha_x + \alpha_y)\ell}\cos 2(\beta_x - \beta_y)\ell$$
$$FF^* = 4e^{-2(\alpha_x + \alpha_y)\ell}$$

Combining terms we have

$$I_o = 4\cos^2\phi\cos^2\theta_F \left[e^{-4\alpha_x\ell} + e^{-4\alpha_y\ell}\right.$$
$$\left. + 2e^{-2(\alpha_x + \alpha_y)\ell}\cos 2(\beta_x - \beta_y)\ell\right]$$
$$+ 16\sin^2\phi e^{-2(\alpha_x + \alpha_y)\ell}\cos^2\theta_F$$
$$- 4j\sin 2\phi e^{-(\alpha_x + \alpha_y)\ell} e^{-j(\beta_x + \beta_y)\ell}\left[e^{-2(\alpha_x + j\beta_x)\ell}\right.$$
$$\left. + e^{-2(\alpha_y + j\beta_y)\ell}\right]$$
$$+ 4j\sin 2\phi e^{-(\alpha_x + \alpha_y)\ell} e^{-j(\beta_x + \beta_y)\ell}\left[e^{-2(\alpha_x + j\beta_x)\ell}\right.$$
$$\left. + e^{-2(\alpha_x + j\beta_x)\ell}\right].$$

Letting $\alpha_x = \alpha_y = \alpha$ and reducing the above expression we get

$$I_o = \gamma^2 I_{in} e^{-4\alpha\ell}\left[\cos^2\phi\cos^2(\beta_x - \beta_y)\ell + \sin^2\phi\right],$$

which is equation (5.5).

For the case where the fiber input eigenmodes are not equally excited, (i.e., $E_x \neq E_y$ and thus $\theta_{in} \neq 45°$), we have the following:

$$E_o = 2(E_y - E_y) e^{-j\phi} e^{-(\alpha_x + \alpha_y)\ell} e^{-j(\beta_x + \beta_y)\ell} e^{-j(\beta_x + \beta_y)\ell}$$
$$\cdot \sin\theta_F + \left[(E_x + E_y)(1 - e^{-j2\phi}) e^{-(\alpha_x + \alpha_y)\ell} e^{-j(\beta_x + \beta_y)\ell}\right.$$
$$\left. + (1 + e^{-j2\phi})(E_x e^{-2(\alpha_x + j\beta_x)\ell} + E_y e^{-2(\alpha_x + j\beta_x)\ell})\right].$$

The output intensity is

$$I_o = E_o \cdot E_o^*$$

$$= 4(E_y - E_x)^2 e^{-2(\alpha_x + \alpha_y)\ell} \sin^2\theta_F + 4(E_y - E_x) \cdot \cos\phi \sin 2\theta_F e^{-(\alpha_x + \alpha_y)\ell} \cos(\beta_x - \beta_y)\ell (E_x e^{-2\alpha_x \ell} + E_y e^{-2\alpha_y \ell})$$

$$+ \cos^2\theta_F \Big\{ 4\sin^2\phi (E_x + E_y)^2 e^{-2(\alpha_x + \alpha_y)\ell} - 4(E_x - E_y) \cdot \sin 2\phi e^{-(\alpha_x + \alpha_y)\ell} (E_x e^{-2\alpha_x \ell} - E_y e^{-2\alpha_y \ell}) \sin(\beta_x - \beta_y)\ell$$

$$+ 4\cos^2\phi \Big[E_x^2 e^{-4\alpha_x \ell} + E_y^2 e^{-4\alpha_y \ell} + 2E_x E_y e^{-2(\alpha_x + \alpha_y)\ell} \cdot \cos 2(\beta_x - \beta_y)\ell \Big] \Big\} .$$

Letting $E_x = E_{in}\cos\theta_{in}$, $E_y = E_{in}\sin\theta_{in}$ and rearranging, we get equation (5.4).

The output intensity is

$$I_o = E_o \cdot E_o^*$$

$$= 4(E_y - E_x)^2 e^{-2(\alpha_x + \alpha_y)\ell} \sin^2\theta_F + 4(E_y - E_x) \cdot \cos\phi \sin 2\theta_F e^{-(\alpha_x + \alpha_y)\ell} \cos(\beta_x - \beta_y)\ell (E_x e^{-2\alpha_x \ell} + E_y e^{-2\alpha_y \ell})$$

$$+ \cos^2\theta_F \Big\{ 4\sin^2\phi (E_x + E_y)^2 e^{-2(\alpha_x + \alpha_y)\ell} - 4(E_x - E_y) \cdot \sin 2\phi e^{-(\alpha_x + \alpha_y)\ell} (E_x e^{-2\alpha_x \ell} - E_y e^{-2\alpha_y \ell}) \sin(\beta_x - \beta_y)\ell$$

$$+ 4\cos^2\phi \Big[E_x^2 e^{-4\alpha_x \ell} + E_y^2 e^{-4\alpha_y \ell} + 2E_x E_y e^{-2(\alpha_x + \alpha_y)\ell} \cdot \cos 2(\beta_x - \beta_y)\ell \Big] \Big\} .$$

Letting $E_x = E_{in}\cos\theta_{in}$, $E_y = E_{in}\sin\theta_{in}$ and rearranging, we get equation (5.4).

APPENDIX 8 ◊ EVALUATION OF $\sigma_{\Delta\beta\ell}$

The expected value of y^2, $E\{y^2\}$, is evaluated from chapter 5, page 48. This evaluation will lead to the standard deviation of the linear birefringence fluctuations, $\sigma_{\Delta\beta\ell}$ $(= \sigma_x)$, which will then determine the standard deviation of the resulting intensity fluctuations or "noise," σ_y.

$$E\{y^2\} = \frac{1}{\sigma_x(2\pi)^{\frac{1}{2}}} \int_{-\infty}^{\infty} (0.5A\cos 2x + C)^2 e^{-\frac{(x-\eta_x)^2}{(2\sigma_x^2)}}\, dx$$

$$= \frac{1}{\sigma_x(2\pi)^{\frac{1}{2}}} \int_{-\infty}^{\infty} \underset{\uparrow 1}{\left[\tfrac{1}{2}A^2\cos^2 2x\right]} + \underset{\uparrow 2}{AC\cos 2x} + \underset{\uparrow 3}{C^2} e^{-\frac{(x-\eta_x)^2}{(2\sigma_x^2)}}\, dx$$

Terms 1, 2, and 3 will be evaluated individually, then summed to give $E\{y^2\}$.

$$\text{Term 1} = \frac{A^2}{8\sigma_x(2\pi)^{\frac{1}{2}}} \int_{-\infty}^{\infty} (1 + \cos 4x) e^{-\frac{(x-\eta_x)^2}{(2\sigma_x^2)}}\, dx$$

$$= \frac{A^2}{8} + \frac{A^2}{8\sigma_x(2\pi)^{\frac{1}{2}}} \int_{-\infty}^{\infty} \cos 4x \cdot e^{-\frac{(x-\eta_x)^2}{(2\sigma_x^2)}}\, dx$$

Letting $x - \eta_x = \xi$ we have

$$\text{Term 1} = \frac{A^2}{8} + \frac{A^2}{8\sigma_x(2\pi)^{\frac{1}{2}}} \int_{-\infty}^{\infty} \cos 4(\xi + \eta_x) e^{-(\xi^2/2\sigma_x^2)}\, d\xi$$

Using the identity $\cos 4(\xi + \eta_x) = \cos 4\xi \cos 4\eta_x - \sin 4\xi \sin 4\eta_x$, and referring to relations in a math handbook [58], we have

$$\text{Term 1} = \underline{\underline{\frac{A^2}{8} + \frac{A^2}{8}\cos 4\eta_x e^{-8\sigma_x^2}}}\ .$$

$$\text{Term 2} = \frac{AC}{\sigma_x(2\pi)^{\frac{1}{2}}} \int_{-\infty}^{\infty} \cos 2x \cdot e^{-\frac{(x-\eta_x)^2}{(2\sigma_x^2)}} dx$$

Letting $x - \eta_x = \xi$ and using a trigonometric identity we get

$$\text{Term 2} = \frac{AC}{\sigma_x(2\pi)^{\frac{1}{2}}} \int_{-\infty}^{\infty} (\cos 2\xi \cos 2\eta_x - \sin 2\xi \sin 2\eta_x) e^{-\xi^2/2\sigma_x^2} d\xi$$

From relations in a math handbook [57], the even argument gives

$$\text{Term 2} = \underline{\underline{0.5AC\cos 2\eta_x \cdot e^{-2\sigma_x^2}}}.$$

$$\text{Term 3} = \frac{C^2}{\sigma_x(2\pi)} \int_{-\infty}^{\infty} e^{-\frac{(x-\eta_x)^2}{(2\sigma_x^2)}} dx = \underline{\underline{C^2}}.$$

$$E\{y^2\} = \text{term 1} + \text{term 2} + \text{term 3}$$

$$= A^2/8(1 + \cos 4\eta_x e^{-8\sigma_x^2}) + 0.5ACe^{-2\sigma_x^2} + C^2$$

The variance of the output intensity fluctuation is

$$\sigma_y^2 = E\{y^2\} - \eta_y^2$$

$$= A^2/8[1 + \cos 4\eta_x e^{-8\sigma_x^2}] + 0.5AC\cos 2\eta_x e^{-2\sigma_x^2}$$

From chapter 5, page 47,

$$A = I_{in}\gamma^2 e^{-4\alpha\ell}\cos^2\theta_F\cos^2\phi$$
$$B = I_{in}\gamma^2 e^{-4\alpha\ell}\cos^2\theta_F\sin^2\phi$$
$$C = \eta_y = A/2 + B$$

Thus,

$$\sigma_y^2 = (I_{in}\cos^2\theta_F e^{-4\alpha\ell})^2(1 + \cos 4\eta_x e^{-8\sigma_x^2})(\cos^4\phi/8) +$$

$$0.5(I_{in}\cos^2\theta_F e^{-4\alpha\ell})^2(0.5\cos^4\phi + \cos^2\phi\sin^2\phi)\cos -2\eta_x e^{-2\sigma_x^2}.$$

Rearranging the above and taking the square root yields σ_y, which is given by equation (5.10) on page 48.

APPENDIX 9 ◊ EXPERIMENTAL DATA: $\Delta\theta$ vs. B

Data is presented for the measurement results of chapter 3. Variable relations and definitions are given on page 22. The relation between the magnetic field **B** and the coil current I_{coil} was determined in appendix 2, and is given by (A2.7).

Table A9.1 Faraday rotation $\Delta\theta$ vs. magnetic field

I_{coil} (mA)	I_D' (10^{-5}W)	I_D (10^{-5}W)	$\Delta\theta$ (deg.)	B (Gauss)
0.0	9.25	9.25	0.0	0.0
0.592	9.2	9.23	0.093	1.2
1.80	9.01	9.09	0.252	3.6
2.24	8.99	9.06	0.221	4.4
2.43	9.02	9.10	0.252	4.8
3.4	8.98	9.10	0.661	6.7
4.24	9.0	9.13	0.408	8.4
4.31	8.92	9.06	0.443	8.5
5.51	8.87	9.06	0.601	10.9
5.60	8.88	9.08	0.631	11.1
5.77	8.91	9.12	0.66	11.4
7.13	8.82	9.05	0.728	14.0
7.96	8.76	9.04	0.887	15.7
8.84	8.73	9.03	0.952	17.5
9.54	8.70	9.03	1.015	18.8
9.97	8.69	9.02	1.048	19.7
11.04	8.63	9.02	1.24	21.8
13.6	8.56	9.01	1.43	26.9
14.34	8.52	9.01	1.56	28.3
15.74	8.48	9.02	1.72	31.1
17.08	8.42	9.00	1.847	33.7
18.81	8.38	9.00	1.975	37.2
19.54	8.33	8.98	2.075	36.8
22.2	8.24	8.98	2.36	43.8
27.5	8.07	9.00	2.966	54.3
30.5	7.97	8.99	3.257	60.2
34.1	7.84	8.99	3.67	67.4
36.2	7.77	8.99	3.9	71.5

Table A9.1--cont.

I_{coil} (mA)	I_D' (10^{-5}W)	I_{D_5} (10^{-5}W)	$\Delta\theta$ (deg.)	B (Gauss)
38.7	7.68	8.98	4.16	76.4
41.6	7.6	8.99	4.45	82.2
43.6	7.52	8.98	4.68	86.1
45.0	7.49	9.00	4.83	88.9
47.6	7.40	8.99	5.09	94.0
48.8	7.35	8.98	5.23	96.4
50.8	7.29	8.99	5.45	100.3
51.6	7.27	8.99	5.45	100.3
53.4	7.21	8.99	5.515	101.9
56.1	7.12	8.99	6.00	110.8
58.8	7.03	8.99	6.3	116.1
61.7	6.93	8.99	6.62	121.9
63.5	6.87	8.99	6.82	125.4
66.1	6.8	8.99	7.05	130.6
69.9	6.68	9.00	7.47	138.1
73.3	6.57	9.00	7.83	144.8
74.8	6.51	8.99	8.01	147.8
77.1	6.44	8.99	8.34	152.3
78.9	6.39	9.00	8.43	155.9
79.2	6.38	9.00	8.46	156.4
81.9	6.30	9.00	8.73	161.8
84.6	6.20	9.00	9.06	167.1
86.7	6.14	9.00	9.26	171.3
88.4	6.09	9.01	9.46	174.6
91.8	5.99	9.02	9.81	181.3
93.1	5.95	9.01	9.93	183.9
94.0	5.93	9.02	10.02	185.7
95.2	5.88	9.01	10.16	188.0
96.5	5.85	9.02	10.29	190.6
97.2	5.83	9.02	10.36	192.0
98.4	5.79	9.02	10.49	194.4
100.9	5.71	9.02	10.78	199.3
101.4	5.7	9.02	10.80	200.3
102.9	5.65	9.02	10.97	203.3
103.3	5.64	9.01	10.98	204.0
105.7	5.56	9.01	11.26	208.8
107.2	5.52	9.01	11.31	211.8
109.1	5.46	9.01	11.60	215.5
111.8	5.38	9.04	11.94	220.8
113.1	5.34	9.04	12.08	223.4

Table A9.1--cont.

I_{coil} (mA)	I_{D}' (10^{-5}W)	I_{D_5} (10^{-5}W)	$\Delta\theta$ (deg.)	B (Gauss)
115.5	5.28	9.04	12.29	228.1
116.6	5.24	9.03	12.41	230.3
117.6	5.22	9.04	12.50	232.3
119.1	5.17	9.04	12.67	235.3
121.4	5.10	9.04	12.67	235.3
122.9	5.06	9.04	13.13	243.5
125.1	4.99	9.04	13.31	247.1
128.6	4.89	9.04	13.70	254.0
130.1	4.84	9.04	13.84	257.0
133.4	4.75	9.04	14.16	263.5
137.6	4.63	9.04	14.60	271.8
139.5	4.58	9.05	14.80	275.6
140.0	4.56	9.05	14.87	276.5
142.5	4.49	9.05	15.13	281.5
146.0	4.40	9.05	15.46	288.4
147.9	4.34	9.05	15.68	292.1
150.6	4.26	9.05	15.98	297.5
152.5	4.21	9.05	16.17	301.2
155.3	4.13	9.05	16.42	306.8
157.1	4.09	9.05	16.62	310.3
159.5	4.02	9.03	16.85	315.0
161.8	3.95	9.04	17.13	319.6
164.5	3.88	9.04	17.40	324.9
165.5	3.86	9.04	17.48	326.9
167.4	3.80	9.03	17.70	330.7
169.6	3.75	9.04	17.91	335.0
171.0	3.71	9.04	18.06	337.8
174.3	3.62	9.03	18.40	344.3
176.2	3.57	9.03	18.60	348.0
178.9	3.51	9.04	18.86	353.4
180.9	3.46	9.04	19.06	357.3
182.9	3.41	9.03	19.24	361.3
184.8	3.35	9.03	19.49	365.0
187.1	3.30	9.02	19.68	369.6
190.8	3.21	9.02	20.05	376.9
192.5	3.17	9.03	20.23	380.2
194.2	3.13	9.02	20.38	383.6
195.5	3.09	9.02	20.55	386.2
196.0	3.09	9.02	20.55	386.2
199.6	3.00	9.02	20.93	394.3
201.	2.90	9.02	21.36	397.0

Table A9.1--cont.

I_{coil} (mA)	I_D' (10^{-5}W)	I_D (10^{-5}W)	$\Delta\theta$ (deg.)	B (Gauss)
204.	2.85	9.01	21.57	403.0
206.	2.80	9.02	21.80	406.8
208.	2.75	9.02	22.02	410.8
210.	2.72	9.01	22.14	414.8
212.	2.67	9.01	22.36	418.7
214.	2.62	9.01	22.59	422.7
216.	2.58	9.01	22.77	426.6
218.	2.54	9.01	22.95	430.6
220.	2.50	9.00	23.12	434.5
222.	2.46	9.00	23.3	438.5
224.	2.44	9.00	23.4	442.4
226.	2.39	9.00	23.63	446.4
228.	2.36	8.99	23.76	450.3
230.	2.33	8.99	23.90	454.3
232.	2.29	8.99	24.09	458.2
234.	2.27	8.99	24.19	462.2
236.	2.25	8.99	24.28	466.1
238.	2.22	8.98	24.31	470.1
240.	2.20	8.98	24.41	474.0
242.	2.18	8.98	24.50	478.0
244.	2.16	8.98	24.60	481.9
246.	2.15	8.98	24.65	485.9
248.	2.13	8.97	24.84	489.8
250.	2.11	8.97	24.94	493.8
252.	2.10	8.97	24.99	497.7
254.	2.08	8.96	25.08	501.7
256.	2.07	8.95	25.12	505.6
258.	2.05	8.95	25.22	509.6
260.	2.04	8.94	25.26	513.5
264.	2.01	8.94	25.41	521.4
268.	1.99	8.94	25.51	529.3
272.	1.96	8.94	25.67	537.2
276.	1.94	8.94	25.77	545.1
280.	1.92	8.94	25.87	553.0
284.	1.89	8.94	26.03	560.9
288.	1.88	8.94	26.08	568.8
292.	1.85	8.93	26.23	576.7
296.	1.83	8.93	26.33	584.6
300.	1.82	8.92	26.38	592.5
304.	1.80	8.93	26.49	600.4
308.	1.78	8.92	26.59	608.3
312.	1.76	8.92	26.69	616.2

Table A9.1--cont.

I_{coil} (mA)	I_{D}' (10^{-5}W)	I_{D} (10^{-5}W)	$\Delta\theta$ (deg.)	B (Gauss)
316.	1.74	8.92	26.80	624.1
320.	1.72	8.91	26.93	632.0
324.	1.70	8.91	27.01	639.9
328.	1.69	8.90	27.05	647.8
332.	1.67	8.9	27.16	655.7
336.	1.66	8.90	27.22	663.6
340.	1.64	8.89	27.32	671.5
344.	1.63	8.89	27.38	679.4
348.	1.61	8.88	27.48	687.3
352.	1.60	8.88	27.53	695.2
356.	1.58	8.87	27.64	703.1
360.	1.57	8.87	27.64	711.0
366.	1.55	8.89	27.03	722.9
370.	1.54	8.88	27.87	730.8
375.	1.52	8.87	27.98	740.6
380.	1.51	8.87	27.98	740.6
387.	1.49	8.86	28.14	764.3
390.	1.48	8.86	28.14	764.3
395.	1.46	8.85	28.31	780.1
400.	1.45	8.85	28.37	790.0
405.	1.44	8.85	28.43	799.9
410.	1.42	8.84	28.54	809.8
415.	1.41	8.82	28.58	819.6
420.	1.40	8.82	28.64	829.5
425.	1.39	8.82	28.70	839.4
430.	1.37	8.80	28.8	849.3
435.	1.36	8.80	28.86	859.1
440.	1.35	8.79	28.91	869.0
445.	1.32	8.77	29.03	898.6
460.	1.30	8.74	29.17	908.5

BIBLIOGRAPHY

Adams, J. *Hall noise in the 6302 current probe.* Tektronix Inc., company report, December, 1984.

Aulich, H., W. Beck, N. Douklias, H. Harms, A. Papp, and H. Schneider. *Magnetooptical current transformer 2: Components.* Appl. Optics 19 (Nov. 1980): 3735-3740.

Born, M. *Principles of Optics.* London: Pergamon Press, 1959, Chapter 1.

Bronowski, J. *Science and Human Values.* New York: Harper & Row, 1965, 13.

Butler, M.A., and S.J. Martin. *Optical fiber magnetic field sensor with nanosecond response time.* IEEE document no. CH2127 (Sept. 1985): 316-319.

Canton, W., and J. Katzenstein. *An absolute electric current probe based on the Faraday effect.* Journal of Research of the NBS 89 (May-June 1984): 265-272.

Clarke, D., and J.F. Grainger. *Polarized Light and Optical Measurement.* Braunschweig: Pergamon Press, 1971.

Cole, J.H., T.G. Giallorenzi, and J.A. Bucaro. *Advances in optical fiber sensors.* SPIE Integrated Optics 269 (1981): 115-119.

Davis, C.M. *Fiber optic sensors: an overview.* SPIE Fiber Optic and Laser Sensors II 478 (1984): 12-15.

Donavan, B., and T. Medcalf. *The inclusion of multiple reflection in the theory of the Faraday effect in semiconductors.* British Journal of Appl. Physics 15 (1964): 1129-1151.

du Chastel, Marie-Helene. *Fiberoptic sensors begin moving from laboratory to marketplace.* Laser Focus (May 1987): 110-117.

Dwight, H. B. *Tables of Integrals and other Mathematical Data.* 4th ed. New York: MacMillan Publishing Co., Inc.

Enokihara, A., M. Izutsu, and T. Sueta. *Optical fiber sensors using the method of polarization-rotated reflection.* Journal of Lightwave Tech. LT5 (Nov. 1987): 1584-1590.

Faraday, Michael. *Experimental Researches in Electricity--Nineteenth Series. Philosophical Transactions,* ed. B. Quartich, 1855. Quoted in W. Swindell, ed. *Polarized Light.* Stroudsburg, Pennsylvania: Halsted Press, 1975.

Fluitman, J., and T. Popma. *Optical waveguide sensors.* Sensors and Actuators 10 (1986): 25-46.

Furdyna, J.K. *Diluted magnetic semiconductiors: an interface of semiconductior physics and magnetism.* Journal of Appl. Physics 53 (1982): 7637-7643.

Gabriel, C.J., and H. Pillar. *Determination of the optical Verdet coefficient in semiconductors and insulators.* Applied Optics 6 (April 1967): 661-668.

Giallorenzi, T.J., J.A. Bucaro, A. Dandridge, G.H. Sigel, Jr., J.H. Cole, S.C. Rashleigh, and R.J. Priest. *Optical fiber sensor technology.* Journal of Quantum Electronics QE-18 (April 1982): 626-661.

Giallorenzi, T.G., J.A. Bucaro, A. Dandridge, and J.H. Cole. *Optical-fiber sensors challenge the competition.* IEEE Spectrum 23 (Sept 1986): 44-49.

Goto, K., T. Sueta, and T. Makimoto. *Travelling-wave light-intensity modulators using the method of polarization-rotated reflection.* Journal of Quantum Electron QE-8 (1972): 486-493.

Gower, J. *Optical Communication Systems.* London: Prentice-Hall, 1984, Chapter 11.

Harms, H., and A. Papp. *Magnetooptical current transformer 3: Measurements.* Applied Optics 19 (Nov. 1980): 3741-3745.

Hecht, E., and A. Zajac. *Optics.* Reading, Mass.: Addison-Wesley, 1979, Chapter 8.

Hillerich, B., and E. Weidel. *Polarization noise in single mode fibers and its reduction by depolarizers.* Optical and Quantum Electron 15 (1982): 281-287.

Imai, M., Y. Terasawa, and Y. Ohtsuka. *Polarization fluctuation characteristics of a highly birefringent fiber system under forced vibration.* Journal of Lightwave Tech. 6 (May 1988): 720-727.

Lee, H. *Optical polarization bistability using the Faraday effect.* Applied Optics 26 (Sept. 1987): 3486-3487.

Jamieson, R.S., R.P. Depaula, and E.L. Moore. *Overview of fiber-optical sensors.* Jet Propulsion Lab Report no. NPO-16817/6329, August 1987, 1-14.

Kersey, A.D., D.A. Jackson, and M. Corke. *Single mode fibre-optic magnetometer with dc bias field stabilization.* Journal of Lightwave Technology LT-3, Aug. 1985.

Krauss, J.D., and K.R. Carver. *Electromagnetics*, 2nd ed. New York: McGraw-Hill, 1973, Chapter 13.

Krawczyk, S.K. *Senso-opto-micro-electronic (SOMET) devices.* Sensors and Actuators 11 (1987): 289-297.

Kullensrff, N., and B. Hök. *Temperature independent Faraday rotation near the band gap in $Cd_{1-x}Mn_xTe$.* Appl. Physics Letter 46 (June 1985):1016-1018.

Kyuma, K., S. Tai, M. Nunoshita, T. Takioka, and Y. Ida. *Fiber optic measuring system for electric current by using a magnetooptic sensor.* Trans. Microwave Th. & Techniques MTT-30, October 1982, 1607-1611.

_____. *Fiberoptic current and voltage sensors using a $Bi_{12}GeO_{20}$ single crystal.* Journal of Lightwave Tech. LT-1 (Mar. 1983): 93-97.

Malewski, R. *High Voltage current transformers with optical signal transmission.* Optical Engineering 20 (Jan.-Feb. 1981): 54-57.

Martin, S.J., and M.A. Butler. *Wideband optical fiber magnetic field sensor.* SPIE Fiber optic and Laser Sensors III 566 (1985): 197-200.

McClelland, S. *Stimulating new developments into applications.* Sensor Review (July 1986): 148-149.

Ovrén, C., M. Adolfsson, B. Hök, and T. Brogårdh. *New Opportunities with fibre-optic measurement.* Sensor Review (Oct. 1985): 199-205.

Palais, J.C. *Fiber Optic Communications.* Englewood Cliffs, N.J.: Prentice-Hall, Inc. 1984, Chapter 11.

Palik, E.D., and J.R. Stevenson. *Multiple reflection effects in the Faraday rotation in thin-film semiconductors.* Journal of Appl. Physics 37 (April 1966): 1982-1988.

Papoulis, A. *Probability, Random Variables, and Stochastic Processes,* 2nd ed. New York: McGraw-Hill, 1984, Chapter 9.

Papp, A., and H. Harms. *Magnetooptical current transformer 1: Principles.* Applied Optics 19 (Nov. 1980): 3729-3734.

Pillar, H. *Effect of internal reflection on optical Faraday rotation.* Journal of Appl. Physics 37 (Feb. 1966): 763-767.

Ramo, S., J. Whinnery, and T. Van Duzer. *Fields and Waves in Communication Electronics,* 2nd ed., New York: John Wiley & Sons, 1984, Chapter 13.

Rogers, A.J. *Optical measurements of power system quantities.* Electronics & Power (Feb. 1986).

Russell, B.D. *Switching transients in power substations present measurement challenges.* EMC Tech. (Jan.-Feb. 1986): 21-24.

Smith, A.M. *Optical fibres for current measurement applications.* Optics and Laser Tech. (Feb. 1980): 25-29.

Sohlström, H., T. Brogårdh, and U. Holm. *Measurement system for magnetooptic sensor materials.* Journal Physics E: Sci. Imstrum. 17 (1984): 885-889.

Turner, A.E., R.L. Gunshor, and S. Datta. *New class of materials for optical isolators.* Appl. Optics 22 (1983): 3152-3154.

Tsai, K. Masters thesis, University of Rhode Island, Department of Electrical Engineering, 1988.

Veeser, L., G.I. Chandler, and G.W. Day. *Fiber optic sensing of pulsed currents.* Los Alamos National Lab. Report no. LA-UR-1212, April 1986.

Willardson, R.K., and A.C. Beer, eds. *Semiconductors and Semimetals.* New York: Academic Press, 1972, Chapter 3.

Zilber, J. *Fiberoptic sensor market development.* Kessler Marketing Intelligence, 1984.